At the Interface of Simulation and Experiment in Composite Cathodes for All-Solid-State Batteries

Dem Fachbereich Biologie und Chemie
der Justus-Liebig-Universität Gießen
vorgelegte Dissertation zur Erlangung
des akademischen Grades
Doktor der Naturwissenschaften
- Dr. rer. nat. -

Anja Bielefeld

Februar 2022

Dekan / Dean	Prof. Dr. Thomas Wilke
1. Gutachter / 1st Reviewer	Prof. Dr. Jürgen Janek (Justus-Liebig University Gießen)
2. Gutachter / 2nd Reviewer	Prof. Dr. Doreen Mollenhauer (Justus-Liebig University Gießen)
Eingereicht / submitted	03.02.2022
Disputation / disputation	04.04.2022

Eidesstattliche Erklärung

Die vorliegende Arbeit wurde im Zeitraum vom 01.07.2017 bis 03.02.2022 am Physikalisch-Chemischen Institut der Justus-Liebig-Universität Gießen in Kooperation mit der Volkswagen AG unter Betreuung von Prof. Dr. Jürgen Janek angefertigt.

Ich erkläre: Ich habe die vorgelegte Dissertation selbstständig und ohne unerlaubte fremde Hilfe und nur mit den Hilfen angefertigt, die ich in der Dissertation angegeben habe. Alle Textstellen, die wörtlich oder sinngemäß aus veröffentlichten Schriften entnommen sind, und alle Angaben, die auf mündlichen Auskünften beruhen, sind als solche kenntlich gemacht. Ich stimme einer evtl. Überprüfung meiner Dissertation durch eine Antiplagiat-Software zu. Bei den von mir durchgeführten und in der Dissertation erwähnten Untersuchungen habe ich die Grundsätze guter wissenschaftlicher Praxis, wie sie in der "Satzung der Justus-Liebig-Universität Gießen zur Sicherung guter wissenschaftlicher Praxis" niedergelegt sind, eingehalten.

Gießen, 03.02.2022

_____

Anja Bielefeld

Disclaimer

Ergebnisse, Meinungen und Schlüsse dieser Publikation sind nicht notwendigerweise die der Volkswagen Aktiengesellschaft.

The results, opinions and conclusions expressed in this publication are not necessarily those of Volkswagen Aktiengesellschaft.

Zusammenfassung

Im Zuge der Energiewende und der Transformation des Mobilitätssektors gewinnen Batterien in vielerlei Hinsicht an Bedeutung. Feststoffbatterien sind, aufgrund ihres Potentials zu hohen Energiedichten, und damit hohen Reichweiten für batteriebetriebene Fahrzeuge, eine mögliche Alternative zu konventionellen Lihtium-Ionen-Batterien. Diese enthalten flüssige, leicht entflammbare Elektrolyte und Lösungsmittel, die in Feststoffbatterien durch einen festen Ionenleiter ersetzt werden und entsprechend auch sicherheitsrelevante Vorteile im Fahrzeug bieten können. Allerdings sind Feststoffbatterien bisher nicht in Massenproduktion verfügbar und weisen teils weitreichende Kapazitäts- und Leistungsunterschiede im Vergleich zu konventionellen Zellen auf. Ein grundlegender Unterschied zwischen den Zellkonzepten ist die Partikelmorphologie der Festelektrolyte: Hochleitfähige Materialien, wie Lithium-Argyrodite (z.B. Li_6PS_5Cl) zählen zu den Glaskeramiken und besitzen damit eine spezielle Mikrostruktur. So entfällt die Möglichkeit, poröse Elektrodenstrukturen aus ionenspeicherndem Material (Aktivmaterial) mit flüssigem Elektrolyten zu infiltrieren. Vielmehr muss der feste Elektrolyt bereits bei der Elektrodenherstellung berücksichtigt werden. Darüber hinaus weisen auch Komposite mit vergleichsweise weichem Festelektrolyt eine Restporosität auf, und die Rolle dieser Porosität und der Mikrostruktur in Elektroden für Feststoffbatterien sind bisher kaum untersucht und verstanden.
Tatsächlich gibt es einige Fragen zur Mikrostruktur, die nur schwerlich mit experimentellen Arbeiten beantwortet werden können. Daher widmet diese Dissertation sich der Elektrodenmikrostruktur aus der Modell- und Simulationsperspektive und untersucht mit verschiedenen Modellansätzen die Leitungsnetzwerke durch die Elektrode, deren Effektivität und das Ladeverhalten mit synthetisch generierten, realistischen Mikrostrukturen.
Die Elektrodenmodelle bestehen aus Kathodenaktivmaterial, Festelektrolyt und Restporosität, die mit ihren charakteristischen Partikelgrößen und -formen, basierend auf Rasterelektronenmikroskopaufnahmen, rekonstruiert werden. Die Modellkomplexität nimmt im Laufe der Dissertation zu, beginnend mit einer Analyse der Perkolation (Durchdringung) von Lithium-Ionen und Elektronen durch die Kathode, die unter anderem aufzeigt, dass kleinpartikuläres Kathodenaktivmaterial mit seiner hohen Oberfläche eine besonders hohe Fähigkeit zur Ausbildung eines perkolierenden Elektronennetzwerkes hat. Die Arbeit mündet in der Simulation der elektrochemischen Prozesse in der Kathode, beleuchtet darin insbesondere das Zusammenwirken von Experimenten und Simulationen und fokussiert die Grenzfläche von Aktivmaterial und Poren. Auch Aspekte der Massenproduktion, wie die Auswirkungen von Bindern, die für Rolle-zu-Rolle-Prozesse benötigt werden, und die (Laser-)Strukturierung von Elektroden werden in der Dissertation behandelt. Die Ergebnisse der Simulationen identifizieren Zielkonflikte im Elektrodendesign und werden für entsprechende Leitlinien herangezogen.

Abstract

In the course of the exit from nuclear and fossil-fuel energy and the transformation of the mobility sector, batteries gain in importance. With their potentially high energy density, and high range for battery electric vehicles, accordingly, (all-)solid-state batteries are a possible alternative to conventional lithium ion batteries. These contain liquid, flammable electrolytes and solvents that are, in solid-state batteries, substituted by a solid ion conductor whose lower flammability could also offer safety relevant advantages.

To date, solid-state batteries are not available in mass production and exhibit partly extensive differences in capacity and performance compared to conventional cells. A fundamental difference in the cell concept is the particle morphology of the solid electrolytes: Highly conductive materials, such as lithium argyrodites (e.g. Li_6PS_5Cl) are counted among the glass-ceramics and possess a specific microstructure. Therefore, it is not possible to infiltrate porous electrode structures that contain the ion storage material (active material), with the electrolyte. Instead, the solid electrolyte has to be considered already upon electrode manufacturing. Moreover, also composites that feature a comparably ductile solid electrolyte have residual void space and the role of these voids and the electrode microstructure in solid-state batteries is barely understood and studied.

Indeed, several questions that concern the microstructure are difficult to address in experimental work. Hence, this dissertation regards the electrode microstructure from the perspective of modeling and simulation and studies the conduction networks through the electrode, their effectivity and the charge behavior of synthetically generated realistic microstructures in different model approaches.

The electrode models consist of cathode active material, solid electrolyte and void space which are reconstructed with their characteristic shapes and sizes based on scanning electron microscope images. The model complexity increases in the course of the thesis, beginning with an analysis of the lithium ion and electron percolation through the electrode which depicts that small cathode active material particles are favorable in forming percolating electron networks due to their high surface area. The work leads to the simulation of the electrochemical processes in the cathode, therein portraying the coaction of experiments and simulations and zooms in on the interface of the active material and the voids. Further, aspects of mass production, such as the effects of binders that are required for roll-to-roll processing and the (laser-)structuring of electrodes, are discussed in the thesis. The simulation outcomes identify trade-offs in the electrode design and are used to develop guidelines, consequently.

Contents

List of Abbreviations and Symbols

General

ASSB	all-solid-state battery
SSB	solid-state battery
LIB	lithium ion battery
AM	active material
CAM	cathode active material
SE	solid electrolyte
SOC	state-of-charge
3D	3-dimensional
P2D	pseudo-2-dimensional

Methods

FEM	finite element method
FVM	finite volume method
DEM	discrete element method
DFT	density functional theory
EIS	electrochemical impedance spectroscopy
SEM	scanning electron microscopy
FIB	focused ion beam
μ-CT	x-ray microtomography

Chemicals

NCM	lithium nickel manganese cobalt oxide, $LiNi_xCo_yMn_{1-x-y}O_2$
LFP	lithium iron phosphate, $LiFePO_4$
β-LPS	lithium phosphorus sulfide, β-Li_3PS_4
LPSCl	lithium phosphorus sulfur chloride, Li_6PS_5Cl
LiTFSI	lithium bis(trifluoromethanesulfonyl)imide, $LiC_2NO_4F_6S_2$
VGCF	vapor grown carbon fiber
PVDF	polyvinylidene fluoride
NBR	nitrile butadiene rubber
PTFE	polytetrafluoroethylene
PPC	polypropylene carbonate
PEO	polyethylene oxide

Symbols

ϵ	porosity
τ	tortuosity factor
l	direct path length
l_{eff}	effective path length
$D_{\text{eff}}^{\text{ion}}$	effective ion diffusion coefficient
$D_{\text{bulk}}^{\text{ion}}$	ion diffusion coefficient in the bulk material
A_s	active surface area
r_p	radius of the active material particles
c_{Li}	lithium concentration in the active material
$\tilde{D}_{\text{Li}}$	chemical lithium diffusion coefficient in the active material
j_n	current density normal to the surface
ρ_ν	density of the material ν
j_0	exchange current density at the interface

1. Introduction

The human-made climate change is undoubtedly a major challenge of our times. The Intergovernmental Panel on Climate Change (IPCC) states in its sixth assessment report:[1]

> *Global surface temperature will continue to increase until at least the mid-century under all emissions scenarios considered. Global warming of 1.5°C and 2°C will be exceeded during the 21st century unless deep reductions in CO_2 and other greenhouse gas emissions occur in the coming decades.*

These deep reductions will and must have an effect on the energy sector and the mobility. In a life cycle analysis Bieker [2] points out that it is impossible to achieve the goals set by the Paris Climate Agreement[3] with combustion engine vehicles and that a transformation to battery electric vehicles and hydrogen fuel cell vehicles is necessary.

One promising candidate or even the jack-of-all-trades for chemical energy storage in mobile applications is often considered the solid-state battery (SSB). However, there is no such thing as *the* SSB and SSBs should rather be regarded as a family with various cell types, layouts, degrees of solidification and materials. They range from semi-solid or hybrid battery concepts[4,5] to all-solid-state batteries (ASSBs) as well as from polymer to ceramic and glassy solid electrolytes (SEs) (with ion conductivities up to 12 $mScm^{-1}$ in $Li_{5.5}PS_{4.5}Cl_{1.5}$ on sintering[6] and 25 $mScm^{-1}$ in $Li_{9.54}Si_{1.74}P_{1.44}S_{11.7}Cl_{0.3}$[7]) and from lithium ion batteries (LIBs) to magnesium ion batteries, to name a few concepts.[4] Consequently, each family member entails diverging advantages and challenges and may be beneficial for a particular application.
To date, conventional LIB technology is well-established and its performance is still being enhanced by newly developed electrode materials and concepts (e. g. the introduction of silicon for higher energy densities[8]), so one may very reasonably ask: Why go solid?
Besides the idea to improve the cell safety by replacing the organic, flammable liquid electrolyte by a solid ion conductor, a major motivation for (A)SSBs is to increase the energy density, and therefore the driving range: One way to achieve this is the utilization of a lithium metal anode which may increase the volumetric energy density by 70 % and the gravimetric energy density by 40 % on the cell level compared to conventional LIBs.[9] In an optimized cell design the anode would then be absent in the discharged state. When charging, lithium ions are extracted from the cathode host material, conducted through the SE and plated at the anodic current collector, *in situ* building the anode layer, which is the best-case scenario for a high energy density. A major issue of lithium metal anodes is the control of homogeneous plating and the volume changes

that go along with it.[10–12] The formation of lithium dendrites that grow through the cell and lead to a short circuit has to be inhibited. Apart from non-uniform plating, the stripping of lithium ions is an issue as well, because the generation of voids has to be prevented.[10] The morphological, thermodynamic and kinetic requirements for a favorable lithium metal/SE interface are brought together by Krauskopf et al. [12].

Besides lithium metal anodes, a high active material loading in the cathode is another way to elevate the energy density, e.g. by using thick electrodes as demonstrated by Kato et al. [13]. The cathode active material (CAM) is typically an intercalation material, such as lithium nickel manganese cobalt oxide, $LiNi_xCo_yMn_{1-x-y}O_2$ (NCM), that provides a layered oxide host structure from which lithium ions can deintercalate upon cell charge. Though, for a pure and dense CAM layer, its ionic conductivity is not sufficient and a lithium ion conductor is required in the electrode. So upon manufacturing a conventional cathode, around 30 vol% of the electrode are pores,[14] provisioned to be filled with liquid electrolyte that establishes the interfacial contact and transports lithium ions to the CAM.
However, the performance of the liquid electrolyte is limited and inhibits thick electrodes: Common liquid electrolytes feature an ionic conductivity of 5-10 mS cm^{-1} at room temperature, depending on the salt concentration and electrolyte system.[15] What should be kept in mind is that the ion conduction is not exclusive for lithium ions, because the anions (e.g. PF_6^-) are mobile as well. The lithium ion current fraction in these electrolyte systems is described by the cationic transference number, with typical values around 0.27 for $LiPF_6$ at 20 °C[15] and the partial lithium ion conductivity is 2.7 mS cm^{-1}, accordingly. In thick electrodes, this is not sufficient and a lithium ion concentration gradient builds up over the electrode thickness.[16]
In contrast, SEs are considered single ion conductors and feature a cationic transference number around unity, except for polymer-based SEs wherein lithium salts are added for conduction and the same issue as in conventional cells arises. Yet, the SE in the cathode poses challenges as well, from degradation[17,18] via (chemo-)mechanics[19] to percolation issues.[20,21] Other than the liquid electrolyte, the SE (except for polymer-based SEs) does not infiltrate (micro-)porosities and possesses a specific morphology. This results in around 15% residual void space[20,22,23] and a significant role of the microstructure for the cell performance:[20,21,24,25] Upon manufacturing, one has to ensure sufficient ionic and electronic percolation. Both, lithium ions and electrons are required for intercalation and must therefore be able to penetrate the electrode in its entire thickness. While the SE allows for fast ion transport, most CAMs provide electron pathways and, depending on the layout, carbon additives, such as carbon black or vapor grown carbon fibers (VGCFs) strengthen the electron transport.[26]

The prerequisites for ionic and electronic percolation and the resulting trade-off between energy and power density are studied in the first publication, (section 3.1) entitled *"Microstructural Modeling of Composite Cathodes for All-Solid-State Batteries"*[21] by geometrical modeling

of conduction clusters for a wide variety of electrode layouts. The work combines percolation theory with 3-dimensional (3D) microstructure models to construct realistic ASSB cathodes and analyzes the utilization levels of CAM and SE and the resulting active surface area. By studying the impact of the void space, the CAM particle size, the composition and the electrode thickness, the work takes the first step to an elaborate electrode design and provides explanations for the limited performance of ASSB cells in various studies. In particular, the study highlights the crucial effects that the void space has on conduction clusters and strongly proposes future experimental studies to measure or calculate the void space for the sake of comparability.

However, a percolating electrode is not a well-performing electrode right away. Once percolating conduction networks are established, these have to be efficient as well. I like to picture the electrode as a maze for charge carriers - for ions and electrons that both have the task to travel through the maze in an effort-saving way. Therefore, tortuous and isolated ion paths should be avoided; they lower the effective ionic conductivity. In a stationary, flux-based simulation, the second publication (section 3.2), entitled *"Modeling Effective Ionic Conductivity and Binder Influence in Composite Cathodes for All-Solid-State Batteries"*,[24] analyzes the links between the effective ionic conductivity and the electrode design. It further proceeds towards industrialization and upscaling by introducing binders into the microstructure. An estimation of the applicable current densities through the composite assesses the impact that the electrode microstructure, the SE bulk conductivity and the electrode thickness have on the cell performance. The study proposes to target an ionic conductivity of 10 mS cm^{-1} to be on a par with conventional cells and illustrates that due to the proper morphology of the SE and the existence of voids in the ASSB composite, SEs are not necessarily enablers for thick high-energy cathodes and require comparably higher conductivities than liquid electrolytes, despite their high transference number.

Finally, the third publication (section 3.3) *"Influence of Lithium Ion Kinetics, Particle Morphology and Voids on the Electrochemical Performance of Composite Cathodes for All-Solid-State Batteries"*[27] deals with microstructural influences on different scales in ASSB cathodes. The electrochemical charge simulations are based on the finite element method (FEM) and in contrast to the first two publications, this work also incorporates the lithium diffusion inside the CAM particles and the charge transfer reactions at the interfaces. The work is closely linked to experiments that provide the input parameters[23,28,29] and the validation data.[23] The closer look at the chemical lithium diffusion coefficient $\tilde{D}_{\mathrm{Li}}$ in NCM811 reveals the intimate relationship that simulations and experiments have: Reliable data on the coefficient are difficult to obtain; $\tilde{D}_{\mathrm{Li}}$ depends on the lithiation degree and the reliability of the data is affected by the lithiation homogeneity of the composite, the miscibility gap and the superposition of anode and cathode signals in the electrochemical impedance spectroscopy (EIS). In the meantime, the charge simulation is heavily affected by $\tilde{D}_{\mathrm{Li}}$. Apart from the interaction of experiments and simulation,

the study zooms in on the CAM/SE-interface with the presence of voids, discusses their size, distribution and surface coverage effects, and models a laser-patterned structured cathode as an outlook toward electrode optimization.

Overall, the models evolve from a simple conduction network analysis to an electrochemical cell charge simulation, progressively. The first publication is based on few, general assumptions and provides rather broad guidelines and the third publication is quite specific and strongly dependent on its experimental input. Still, all publications are interactive with experiments, either by addressing questions that result from experiments, by basing assumptions of experimental findings, by providing guidelines for experimental work or by relying on experimental input. Chapter 2 puts these interactions into the greater context, including the epistemology of scientific models, simulations and experiments.
Inspired by Berro [30], I develop an agenda on how to build useful models (section 2.1.1), analyze the interactions of simulations and experiments (section 2.1.2) and briefly introduce the crux of the Newman Model as the state-of-the art model for conventional LIBs (section 2.2.1). Finally, the existing ASSB simulations, including the publications of this work, are arranged in a simulation landscape from general, broadly applicable models to specific, highly complex models (section 2.2.2).

2. Fundamentals

For (A)SSBs, many issues remain unsolved and many research questions are to be answered: From materials design to manufacturing and from "What conditions [...] modify lithium plating and stripping behavior?" to "How should composites be designed to maintain their structure and internal connectivity during cycling?".[31] Not all of these questions are (easily) accessible by experiments and models and/or simulations may offer a different perspective.
Admittedly, introducing models and/or simulations to these problems, a whole bunch of new questions arises:

- (How) Are these research questions accessible by models and simulations?
- Which requirements should these models fulfill? How detailed do they have to be?
- What interfaces with experiments are there?
- How to assure reliability and computational feasibility?

In the following chapter, I target to give answers to these questions in regard to the ASSB research and to assess the publication landscape in this context.

2.1. Models, Simulations and Experiments

> *All models are wrong, but some are useful.*[32]

To understand the interaction of experiments and simulations, we dive into the epistemological understanding of simulations, their role in knowledge gain.

But first: What are simulations? And how are they distinct from models?

Models are mathematical constructs accompanied by verbal interpretations, that are created to describe phenomena.[33] When these phenomena get too complex to be modeled and solved analytically there are two ways of investigating the phenomenon anyway: simplification or computer simulation.[34] In the computer simulation, e.g. the FEM, complex systems of equations are approximated by numerical methods. In the FEM, also the model geometry is discretized into small elements by the construction of a mesh.[35] Without going too much into detail, computer simulations are approximations of mathematical models, implemented in a software. Or in other words, the ingredients for models are established theory, physical insight and mathematical tricks

and by translating these in a computer algorithm, one can simulate the target system behavior.[36] But, as Box[32] puts it, also models, and that includes theories and scientific laws, are approximations of reality. They cannot tell us the whole truth. They might tell us the truth about parts of reality, but one should always bear in mind the underlying assumptions and variables chosen for the model and the limitations that go along with it.[32]
So, what applies for models also holds for computer simulations: To "All models are wrong, but some are useful.",[32] I'd like to add: "All simulations are wrong, but some are useful."
It is essential to understand the underlying assumptions, the use cases and, correspondingly, the limits of validity. In the case of FEM simulations, this means being aware of the limitations of the underlying mathematical model, the geometry model as well as the simulation implementation. At which point does the approach become invalid and what results from it? Because of these inherent similarities for simulations and models, I will not treat simulations separately, but assume, they fall into the parent category of models in general.

If only some models are useful, what makes a model useful?

As Truran[34] describes, the verification, testing and real world application is, what builds confidence and trust into a model.
The verification assures that the model is internally consistent, from the suitability of the assumptions to the correct implementation of the mathematical equations into program code.
The validation then checks whether the model is capable of providing the information it is intended for. Does it fulfill its purpose and answer the underlying research questions? Is it able to reproduce experimentally measured data under similar model conditions? Or as M. Brenner is cited: "If a model does not tell you something new, it needs to go."[37]

2.1.1. How does one assure to build a model that is indeed useful?

In the context of electrochemical energy storage devices combinations of experiments and simulations or modeling are quite common,[22,25,26,38] however reflecting upon the techniques, their interplay and the (communication) gap that is to be bridged has not been done, yet. Of course, simulation just for the sake of simulating is absurd and potentially futile.
In cell biology and biophysics, the research community is one step ahead: When the number of publications that include simulation increased by the mid 2010s, Berro[30] and Möbius and Laan[37] scrutinized when, how and and to which extent, simulations can and should be used, with the goal to provide guidelines for researchers from all involved disciplines and to facilitate communication and co-working.
Berro[30] even presents a tentative agenda containing nine points on how to develop useful models. A slightly modified version of this agenda is visualized in figure 2.1. To exemplify what the agenda implies, each step is put in context with this thesis' first publication that is intended to (among others) answer whether conductive carbon, such as Super C65, is required in ASSB

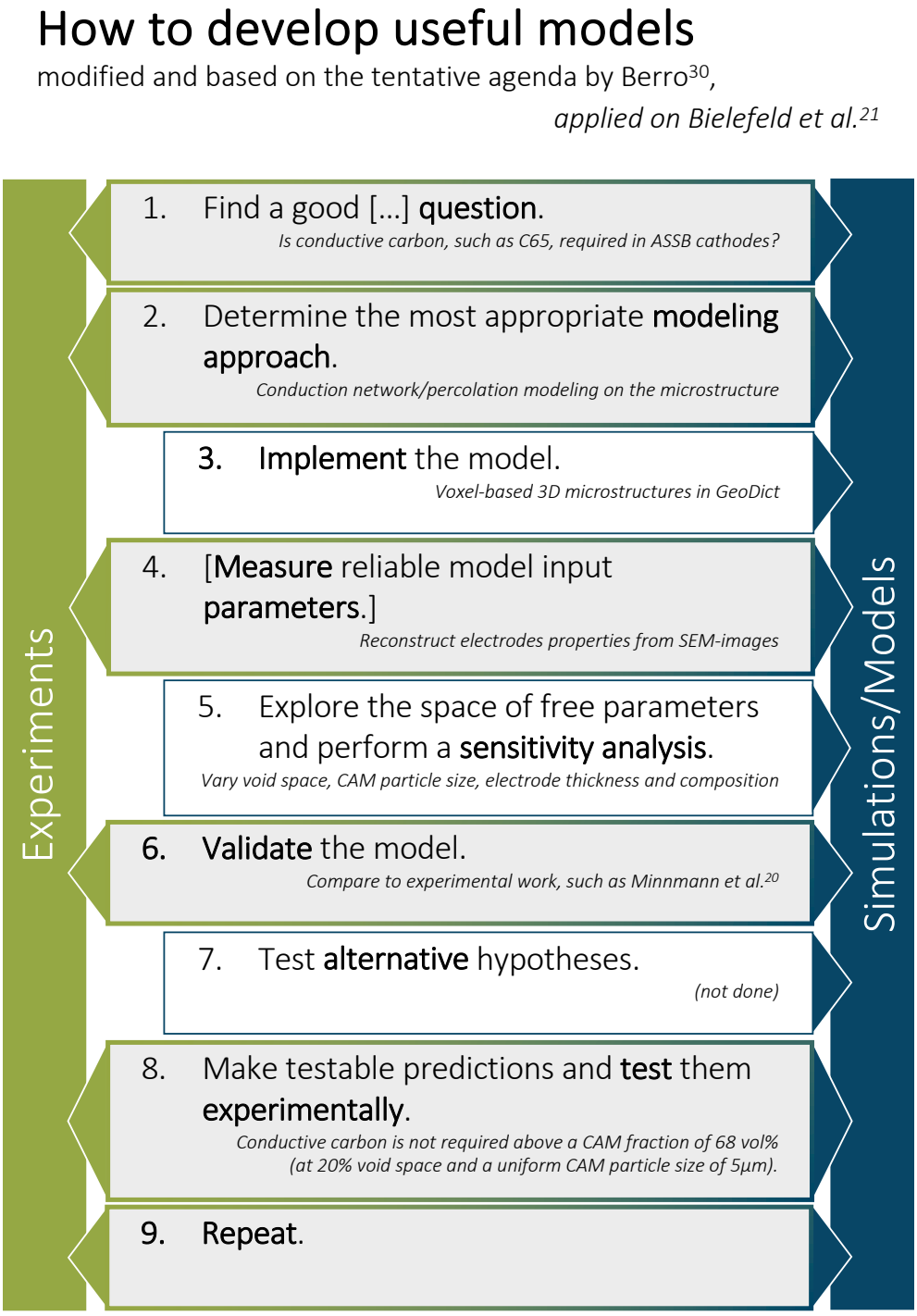

Figure 2.1.: Agenda on how to develop useful models, originally proposed by Berro [30]; here step 1. is generalized and step 4. is modified. The agenda is applied on the question whether conductive carbon is required in ASSBs with the simulation in publication 1[21](section 3.1) in italic. The arrows sketch the interaction of experiments and simulations.

cathodes. From an experimental point of view, it would be favorable to build electrodes that do not contain conductive carbons, because these are known to degrade thiophosphates, such as $Li_{10}GeP_2S_{12}$[39] or β-Li_3PS_4,[18,26] and to lower the cell performance. Furthermore, in figure 2.1 the linkage of the model with experiments is visualized by arrows.

Let us take a closer look at the tentative agenda:

1. **Find a good [...] question.**
   Preliminary to building a model, it is essential to identify a research question of interest. One, that is non-trivial, has not been answered in multiple studies previously and that can be addressed by a model. If the question can better be answered by an experiment, there is no need for a model.[30] But if there is a chance for a model to become an shortcut for the experiments, it can still be a useful tool.
   The "conductive carbon"-question provides a good example: The question can generally be answered by a well-chosen experiment that tests different electrode compositions for their electronic (and ionic) conductivity, such as the one performed by Minnmann et al. [20]. However, a wide screening of a variety of electrode design parameters would require a lot of time and effort and a model that provides guidelines on where to focus the experimental work can be a shortcut.

2. **Determine the most useful model approach.**
   A key to identify the most useful model approach is parsimony, or as Box [32] puts it: "simplicity illuminates, and complication obscures". The law of parsimony is also referred to as Occam's razor which implies that when confronted with two models, describing the phenomenon equally well, one should keep the simpler one.[34,40] This is not always straightforward, because simplicity is not well-defined and has to be put into context. If we want to quantify simplicity by the degrees of freedom, for example, a line might seem more simple to describe than a circle in a Cartesian system, because it requires only two points that mark the ends. But when transferring to polar coordinates, circles are just as easy to describe by a radius and a center.[40] Apart from the vague definition of simplicity, Occam's razor is regarded quite critically among scientists. The qualitative study of Riesch [40] indicates that while many scientists find simplicity useful and some believe that simplicity in theories actually mirrors the simplicity in nature, Occam's razor is not uncommon to be outright rejected.
   Despite skepticism of Occam's razor, parsimony does not only make the modelers life easier, but also avoids overfitting. Or as John von Neumann is cited: "With four parameters I can fit an elephant, and with five I can make him wiggle his trunk.".[41]
   So, when setting up a model, it is recommended to either use a universal approach, because of its broad applicability and lower computation cost[37] or to focus on a specific phenomenon and stick with manageable degrees of freedom.
   In the case of the "conductive carbon"-question, one could have simulated an entire ASSB

cell including degradation phenomena, mechanics, temperature influences, etc. – The road of complexity is endless. However, with a rather simple approach of a network analysis in microstructure particle arrangements the research question was accessible at low computational cost and with few input parameters.
The modeling assumptions often originate from experiments, e.g. the negligible electronic conductivity in the SE and the ionic conductivity in the CAM had previously been shown in experiments.[42]

3. **Implement the model.**
When implementing the model, one has to check in which environment the model will be represented and implemented best? Depending on the research question, the mathematical model and the available resources, the software choice may range from self implemented C++- code to the use of predefined interfaces in a commercial software.
For the "conductive carbon"-question, I started implementing my own microstructure generation code and a version of the Hoshen-Kopelman algorithm[43] in Matlab,[44] until I realized the existence of a ready-to-use software available in my vicinity that did the job with less bugs and helped me to focus and concentrate on other steps in modeling.
When modeling microstructures, one should also keep in mind that the FEM and finite volume method (FVM) might not be equally suited for the task.[45]

4. **Measure reliable model input parameters.** This is, where I propose a different focus than Berro[30], who suggested to "Identify model parameters that fit the data." and that screening parameters until the model output fits the experimental data is the general practice. He warns that a parameter set which produces a good fit is not necessarily the only parameter set that does.
And while this procedure might be fine in other fields, there have been different studies on the parametrization of electrochemical models for conventional LIBs; all conclude that a reliable simulation result can only be obtained when the input parameters are reliable,[46–48] which is quite intuitive, just like the adage: Garbage in, garbage out.
Therefore, my suggestion for the fourth step is to measure reliable model input parameters on the materials (and material combinations) that are to be simulated. Adopting previously measured data sets to the own simulation should be done with caution and only if the materials are the same. Ecker et al.[48] points out, that the lithium diffusion coefficient in the active material is a critical parameter in particular, as the values reported in the literature vary widely and the coefficient has to be implemented including its dependence on the lithiation degree of the active material. An experience that I share from the third publication.[27]
When the model parameter set is not complete and experimental measurements are not possible, I suggest to either simplify the model, e.g. instead of simulating a full electrochemical cell, relying on a flux-based simulation of the effective conductivity, or to factor

out the specific parameter by making a sophisticated guess that assures this parameter will not affect the simulation result. Of course, such a step must be explained in detail and discussed.

5. **Explore the space of free parameters and perform a sensitivity analysis.**
   Even with a reliable input parameter set, one has to be aware that all input data are limited by their accuracy and precision. To get an impression how robust the simulation is with respect to the input parameters, a sensitivity analysis is appropriate. If small changes in a parameter result in large deviations in the results, the particular parameter should be elaborated on.
   In the electrode microstructure model of the first publication[21] this meant, screening the electrode design parameters: void space, CAM particle size, electrode thickness and composition.

6. **Validate the model.**
   Once the model is all set up, it is important to check whether it actually describes the processes in the target system, usually by comparing the simulation results to experimental data that is measured under controlled and comparable conditions.
   In pseudo-2-dimensional (P2D) Newman-type electrochemical battery models, new model implementations[49] are also validated numerically by comparison with an existing well-established implementation of the P2D model, such as COMSOL[50] or DUALFOIL.[51]
   In simulations that rely on complex geometries, such as electrode microstructures, one has to make sure that the chosen mesh (for FEM-based simulations), voxel size, etc. is adequately representing the structure. This means testing different discretizations and mesh refinements. In the FEM, the h-method describes the refinement of linear or parabolic mesh elements and apart from that one should also consider to use the p-method that relies on elements with a variable polynomial order.[52]
   For the work on conductive carbon in ASSB cathodes, the main validation was later done by Minnmann et al.[20]. However, the effect of the CAM particle size on the electronic conduction network and its utilization degree had already been shown experimentally by Strauss et al.[53], previously and helped to assure the model suits the intended purpose. Still, technically, this is rather a qualitative agreement than a full validation.

7. **Test alternative hypotheses.**
   If a phenomenon can be explained by different mechanisms, one should test the alternative as well to distinguish which hypothesis is most likely to be true. This may require the design of adequate experiments that discard one of the possibilities.

8. **Make testable predictions and test them experimentally.**
   Apart from the direct validation and the test of alternative hypotheses, simulations can advance to experimentally unexplored regions and predict the systems behavior. However,

the best prediction is useless, if it is not experimentally verifiable. – Another argument to keep it simple. – If the model becomes excessively complex, its predictions are unlikely to be concrete, distinguishable and verifiable.
For the question of conductive carbons in ASSB cathodes, the work predicts: "Conductive carbon is not required above a CAM fraction of 68 vol%".[21] A statement that was later supported by Minnmann et al.[20] who tested cathode compositions between 25 to 61 vol% NCM622 and observed that the electronic tortuosity factor goes down to 4.3 for the highest NCM fraction, compared to 120 at 25 vol% NCM622. They conclude that high CAM fractions could enable sufficient electron percolation and supersede carbon additives. This is not the exact same conclusion, but considerably close.

9. **Repeat.**
Scientific questions reproduce. Answering one, usually evokes several new questions.
Therefore, refining the model, revisiting its assumptions and implementation and expanding its scope can be useful to touch upon newly arising questions.

2.1.2. Interactions of Simulations and Experiments

We have scratched the interaction of experiments and simulations already in the previous section. With 3., 5. and 7. there are only a few steps in the modeling agenda that do not involve experiments. From the obvious aspects that simulations have to be validated with experimental data to the experimentally obtained insight that is the basis for fundamental model assumptions or the availability of reliable input parameters for the simulation. Experiments are an integral part of simulations providing the motivation for simulations as well as the foundation and the credibility.
But despite all similarities and common goals, simulations and experiments involve different viewpoints on problems and may also lead to diverging perceptions, definitions and/or use of language. A situation that is natural to arise in interdisciplinary environments. For example in biophysics, where Bentovim et al.[54] depict the different understanding of the term 'precision' among biologists and physicists and attempt to dissolve it. Due to the complexity of all the disciplines involved, complete all-round-knowledge is impossible to obtain. This leaves a gap which becomes all the worse, when the interaction of simulations and experiments is impeded by deficient communication or ignorance of the simulation/experiment counterpart.
Möbius and Laan[37] suggest to bridge the inter-disciplinary gap by adapting the explanation degree and language use to the audience. Berro[30] depicts that the simplistic assumptions used by mathematicians and physicists in modeling biological processes are occasionally not sufficiently explained. He encourages to switch the perspective by role reversal, arguing that switching the perspective does not only widen the horizon, but also helps understanding the methods, assessing the data accuracy and proposing expedient experiments. Modelers in the lab building battery cells and measuring cycle data and experimenters who test different time discretizations,... – Not

the worst vision, is it?
I agree that communication is the key. Only well-explained models are graspable for other scientists and when they understand the model, they can think it through, question it and, eventually, gain trust in the model and its predictions. Once this trust is established, experimenters will be more likely to draw conclusions for their own work, to eventually test the simulations predictions in practice or to develop suggestions for further model sophistication.
Notwithstanding all gaps between specialists, epistemologically, simulations can be regarded as a particular kind of experiment, also called *in-silico* experiments.[36,55] For Frigg and Reiss [56] simulations create parallel worlds that represent the target system, but this does not distinguish them from experiments or models of all kinds. They further highlight the capability of simulations to mediate between theories and experiments and Morgan [57] pictures models as "artificial worlds built to represent the real world" and experiments as "versions of the real world captured within an artificial laboratory experiment". For me, simulations could join this perception as "versions or approximations of an artificial world built to represent the real world".
And because this is quite abstract and not straightforward to grasp, communication is essential for inter-disciplinary work.

2.2. Battery Models

From the methodological background and the epistemological understanding of models and simulations in general, let us proceed to their application in battery research and particularly in ASSB cathodes.

2.2.1. The Newman Model

The state-of-the-art model to describe the electrochemical processes in a battery with liquid electrolyte is based on the early works by the group of John Newman.[58,59] It is widely known as the Newman model or the P2D-model and has been simplified, as well as extended in various directions over the years from single-particle models to multi-scale models including aging and/or mechanical effects (for a detailed overview, see Falconi [47], chapter 1.4 or Ramadesigan et al. [60]). Generally, to model a battery cell, one has to account for the charge transport, namely diffusion and migration, in the relevant materials and reactions at the interfaces, e.g. the intercalation of lithium ions into the graphite host structure at the anode. From the original works of Doyle [58] and Fuller et al. [59] to more recent publications,[47,49,61] the P2D-model has been explained at length and I will refrain from doing so again and limit this section to the main line of thoughts. The crux of the P2D-model is to break the complex 3D microstructure down to a computationally convenient 2-dimensional system in two steps:

Effective microstructure parameters Newman and co-workers developed the idea of describing

the complex electrode microstructure by three characteristics: porosity, tortuosity and active surface area. The underlying assumption is that the electrode microstructures are sufficiently homogeneous for this purpose.

- The porosity ϵ represents the electrode composition, particularly the volume fraction that is available for the liquid electrolyte. In conventional LIBs the porosity is usually around 30 %.[14]
- The tortuosity factor τ describes how intertwined a path is, as illustrated in figure 2.2. So when the charge carriers travel through the electrode, the idea is to account for the microstructural influences by a factor that elongates the way they have to travel.

$$\tau = \frac{l_{\text{eff}}}{l}, \tag{2.1}$$

with the direct path length l and the effective path length l_{eff}. The effective ion diffusion coefficient $D_{\text{eff}}^{\text{ion}}$ is then described by

$$D_{\text{eff}}^{\text{ion}} = \frac{\epsilon}{\tau^2} D_{\text{bulk}}^{\text{ion}}, \tag{2.2}$$

where the diffusion coefficient in the pure liquid electrolyte is denoted as $D_{\text{bulk}}^{\text{ion}}$. Today, τ and a common assessment of it by the Bruggeman relation(s)[62] are controversially discussed.[63–66] Commercial LIB cathodes possess tortuosity factors around 4.[67]

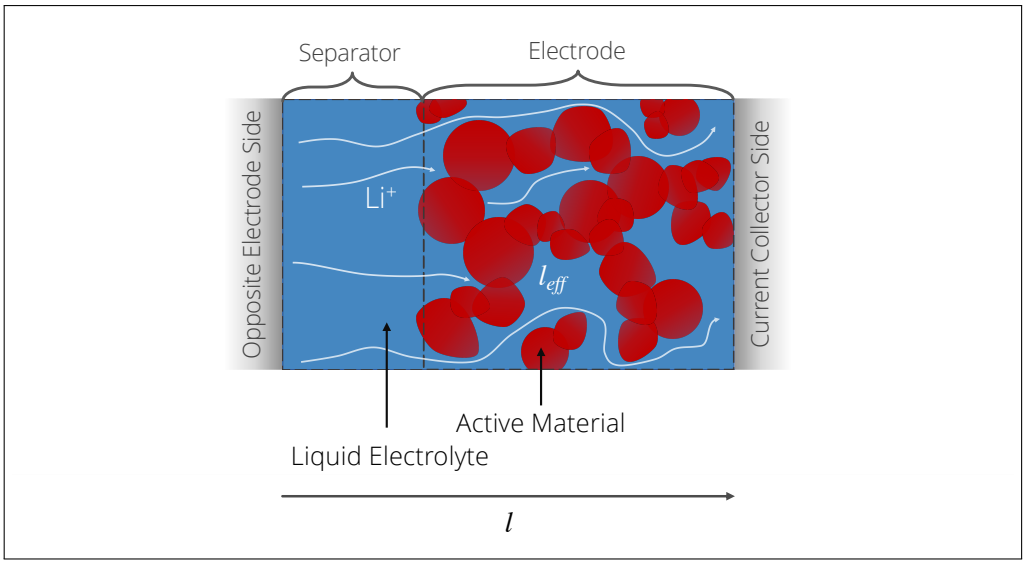

Figure 2.2.: Schematic representation of ion pathways in a liquid electrolyte cell.

- The active surface area A_s is the surface area that is available for insertion and

extraction of lithium ions to/from the active material (AM).

The introduction of these parameters allows to describe the battery cell, the charge transport in the liquid electrolyte and the (de-)intercalation of lithium into/from the AM in just one dimension, x that runs from the anode current collector through the electrodes and separator to the cathode current collector. However, this dimension is not well-suited to describe the diffusion of lithium inside the AM particles. Therefore, Newman and co-workers extended the model with a second dimension.

Spherical coordinates in the active material Once lithium ions have reached the interface of the liquid electrolyte and the AM they will intercalate into the latter (if the local electric field is sufficiently large). So inside the AM particle, a lithium concentration gradient forms and the ions diffuse into the particle center according to Fick's law. In the P2D-model, one chooses the radius of the AM particles r_p to be the second dimension in the model. Assuming spherical AM particles, the ion mass balance can be described by

$$\frac{\partial c_{\mathrm{Li}}}{\partial t} = D_s \left(\frac{\partial^2 c_{\mathrm{Li}}}{\partial r^2} + \frac{2}{r} \frac{\partial c_{\mathrm{Li}}}{\partial r} \right), \tag{2.3}$$

with the local lithium concentration c_{Li}, the lithium diffusion coefficient in the AM $\tilde{D}_{\mathrm{Li}}$ and the spherical coordinate, the radius r. In the particle center, there is no flux

$$- \tilde{D}_{\mathrm{Li}} \left. \frac{\partial c_{\mathrm{Li}}}{\partial r} \right|_{r=0} = 0 \tag{2.4}$$

and at the outer AM particle boundary the current density j_n is given by the reaction at the interface

$$- \tilde{D}_{\mathrm{Li}} \left. \frac{\partial c_{\mathrm{Li}}}{\partial r} \right|_{r=r_p} = j_n. \tag{2.5}$$

These two assumptions facilitate the modelers life and enable fast simulations.
Naturally, the assumptions narrow the applicability of the model, e.g. not all AMs are spherical particles. The particle shape of natural graphite, for example, is flake-like, while synthetic graphite features a random particle shape.[8] NCM single-crystals are also shaped rather octahedral or tetradecahedral,[68,69] but secondary NCM particles possess a spherical form.[70]
The homogenization assumption that supports the use of effective parameters is also limited in its applicability. Real electrodes in conventional lithium ion cells are more complicated than homogeneously distributed AM and the remaining space (the porosity) filled with liquid electrolyte. (as sketched in figure 2.2. Mass-produced anodes and cathodes feature polymeric binders, such as polyvinylidene fluoride (PVDF) or nitrile butadiene rubber (NBR) that provide mechanical support for the porous AM structure. In cathodes, carbon additives, namely Ketjenblack, Super C65,

VGCFs or others, ensure sufficient electronic conduction. Both components make only a small weight fraction, but, depending on the density ($\rho_{\mathrm{PVDF}} = 1.78$ g cm^{-3},[71] $\rho_{\mathrm{NBR}} = 1$ g cm^{-3}[72] and $\rho_{\mathrm{VGCF}} = 1.8$ g cm^{-3}[73] compared to $\rho_{\mathrm{NCM}} = 4.76$ g cm^{-3}), the volume they take may not be negligible.
Further, scanning electron microscopy (SEM) images show that the production process influences the distribution of binders and the agglomeration of carbons.[74–76] Apart, it is unknown to which extent binders and carbons are nanoporous and may be penetrated by the liquid electrolyte.[77,78] This is where the P2D-model reaches its limits and FEM- or FVM-based simulations investigate the effect of binders and carbons.[45]

2.2.2. All-Solid-State Battery Models

In ASSBs the above mentioned issues are supplemented by another component in the electrodes: Voids.
Other than in conventional cells, the electrolyte cannot wet and penetrate the pores. In ASSBs that feature ceramic or glassy electrolytes, the SE has a particle morphology, even if it is a rather soft material, like the thiophosphate SEs.[79,80] The assumption that all non-CAM-volume is filled with electrolyte no longer applies. This is shown schematically in figure 2.3. The volume taken up by voids is around 15 %[20,22,23] in pressed cells with thiophosphate SEs. This fraction can be reduced to 6-8% by sophisticated manufacturing techniques,[81] but an entire elimination is

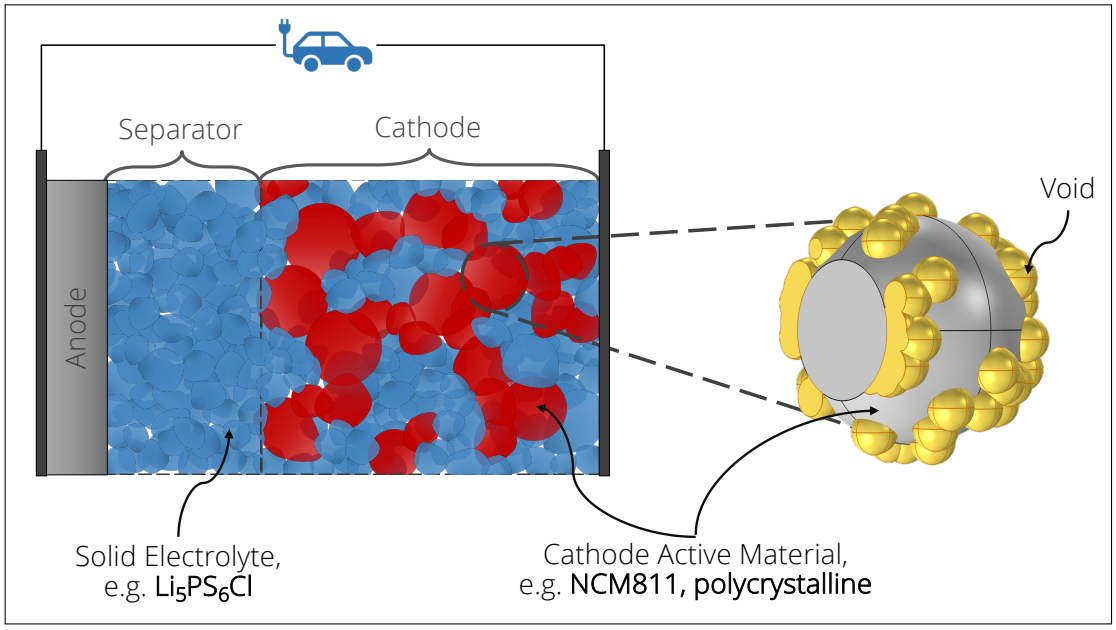

Figure 2.3.: Schematic representation of an ASSB with a zoom on the voids at the CAM/SE-interface. In reality, the voids rather possess a random shape and their size, spatial distribution and evolution upon cycling is mostly unknown.

unlikely. Therefore, the microstructure is suspected to play a decisive role in the performance of ASSBs.
A typical research question in the context of batteries is:

- Which component is rate limiting?

Once the critical component is identified, further questions are to be answered:

- Is the critical parameter a material property that must be tackled by material optimization (e.g. substitution or doping in CAMs or SEs)?
- Does the limitation originate from the electrode layout and the composition, particle distribution or particle size should be adjusted?
- Or is the tuning of the cycling conditions required and the limits can be pushed by high-temperature cycling or applying pressure to the cell?

Figure 2.4 shows the recent ASSB simulation landscape with a focus on composite cathodes and their microstructure. There are issues and open questions at the anode side, likewise and some anode issues might counteract with cathode issues, but to date, the simulation strategy is rather to separate issues and keep it as simple as possible, just like step 2 in the modeling agenda suggests. The x-axis of figure 2.4 is inspired by the model classification of Möbius and Laan [37] who distinguish between universal models that feature general principles and are broadly applicable and highly complex, specific models that are theoretically more sophisticated, but usually act as a spotlight on a very specific topic rather than illuminating the overall picture. This is not supposed to be a grading as in good/bad, but shows the various model approaches for ASSB simulations and the clusters that form.

On the universal end ... Braun et al. [82] assess the general design of ASSBs in a 1-dimensional homogenized transmission line impedance model that simulates discharge curves for various separator thicknesses and temperatures. The electrode microstructure is represented by the effective parameters, porosity and tortuosity, that were introduced in the Newman Model (section 2.2.1) and the SE does not posses a specific morphology. The model exhibits flaws at elevated C-rates, because it simulates the cell behavior in equilibrium state and parameters, like the specific charge-transfer resistance at the interfaces are rough estimates. Yet, its Ragone diagrams sketch the overall development for ASSB design.

Conduction network models do not simulate discharge curves or model the chemical processes, but focus on the electronic and/or ionic conduction clusters. The implementation of the cathode microstructures is either based on voxel particle arrangements (FVM)[21,83] or discrete element method (DEM) with spherical particles.[25,84] Laue et al. [83] and Sangrós Giménez et al. [84] both investigate lithium iron phosphate, $LiFePO_4$ (LFP)/polymer-SE (e.g. polyethylene oxide (PEO):lithium bis(trifluoromethanesulfonyl)imide, $LiC_2NO_4F_6S_2$

(LiTFSI))/carbon black composites and are particularly interested in a homogeneous distribution of the carbon black to ensure sufficient electron conduction. While LFP-containing composites require carbon additives to compensate the low electronic conductivity, this question is open for debate in NCM-containing ASSB cathodes and part of my first publication.[21] The conduction network models do not require a plurality of input parameters and rely solely on the particle sizes, distributions and shapes (only for voxel-based representations, as the DEM to limited to spherical particles) and despite their low level of complexity, they turn out useful for general issues.

Flux-based simulations are a stationary approach to approximate effective conductivities[24,85] that we got to know as an auxiliary property from the microstructure homogenization approach in the Newman Model (section 2.2.1). Although the porosity and the tortuosity are not able to fully describe the microstructure of ASSB electrodes, they are still noteworthy characteristics to study the effect of different electrode design parameters. Park et al. [85] and my second publication[24] both study the influence of binders in a flux-based simulation. Still not reflecting other processes than the transport of charge carriers in an electric field, these models require the bulk conductivites as additional input compared to the pure network models. The bulk conductivities are commonly measured to characterize materials and are, consequently, straightforward to obtain for modelers.
The analysis of Park et al. [85] also simulates discharge curves, which leads us over the the largest cluster:

Electrochemical cell simulations The general idea is not far off the Newman model with a mathematical description of lithium diffusion inside the AM particle, ion transfer at the AM/SE-interfaces denoted by the Butler-Volmer equation and charge and energy conservation. What is different in ASSBs is that single ion conductors can be modeled as (ionic) Ohmic conductors (for a detailed explanation, see section 3.3, "mathematical model"[27]) and that the homogenization approach is not applicable. Instead, FEM[27] or voxel-based methods[26,38,86,87] are used to approximate the system of partial differential equations on the particle microstructure. The cell simulations provide charge or discharge voltage curves and information about the lithium distribution and the current density in every discretized geometry part. These simulations are closer to actual cell cycling than the approaches to the left in figure 2.4, but that inherits challenges: Besides the higher model complexity and the resulting computational cost, the input parameters needed for this kind of simulation are various and not straightforward to obtain. As described in section 2.1.1 the reliability of the input strongly affects the reliability of the output.
Finally, this model type is quite specific compared to the conduction network models, where the outcome was broadly applicable. In the context of electrode cell charge or discharge simulations the conditions are tightly defined. In predicting anything from these models, one has to reflect upon the underlying assumptions and always remember the validity

limits.

... further down the road of specific models is the space charge layer simulation of Becker-Steinberger et al. [88] who focus on the SE and its interfaces with the anode and the cathode. The controversy about the significance of the build-up of lithium depleted layers that result in a space charge is still ongoing for SEs and the models have the potential to provide insight that is hardly ever extracted experimentally.
Of course, this is not the actual end of the road and the model landscape in figure 2.4 is not the full picture, but rather a cutout. Also, the work of Becker-Steinberger et al. [88] should be regarded as a representative for models with an elevated complexity. There are other approaches, such as the density functional theory (DFT)-based simulations by Swift et al. [89].

To date, generally, the landscape of simulation studies for ASSBs is quite barren. There are comparably few simulation studies overall and especially the field of mechanical modeling is in the fledgling stages.[90] Meanwhile, there are many (chemo-)mechanical issues to be addressed and coupled electrochemical-mechanical models are a prospect to point out where the comfort zone for the cell, in terms of external pressure and cycling conditions, is. This is especially important, when proceeding towards practical application in electric vehicles with the integration of the cells into the battery pack and the design of the battery module that comprises cell stacks.
So, has the SSB-research passed the simple conduction network and flux-based models? Will the models get more and more complicated from now on with multiple coupled effects and scales?
Not necessarily. Instead, the strategy should be to build models according to the agenda suggested previously (section 2.1.1) and not to forget about step 2: "Determine the most useful model approach." Be parsimonious with the model complexity and if needed, focus on a specific effect rather than building the all-in-one model suitable for every purpose that is difficult to implement, to understand, to interpret and to explain.

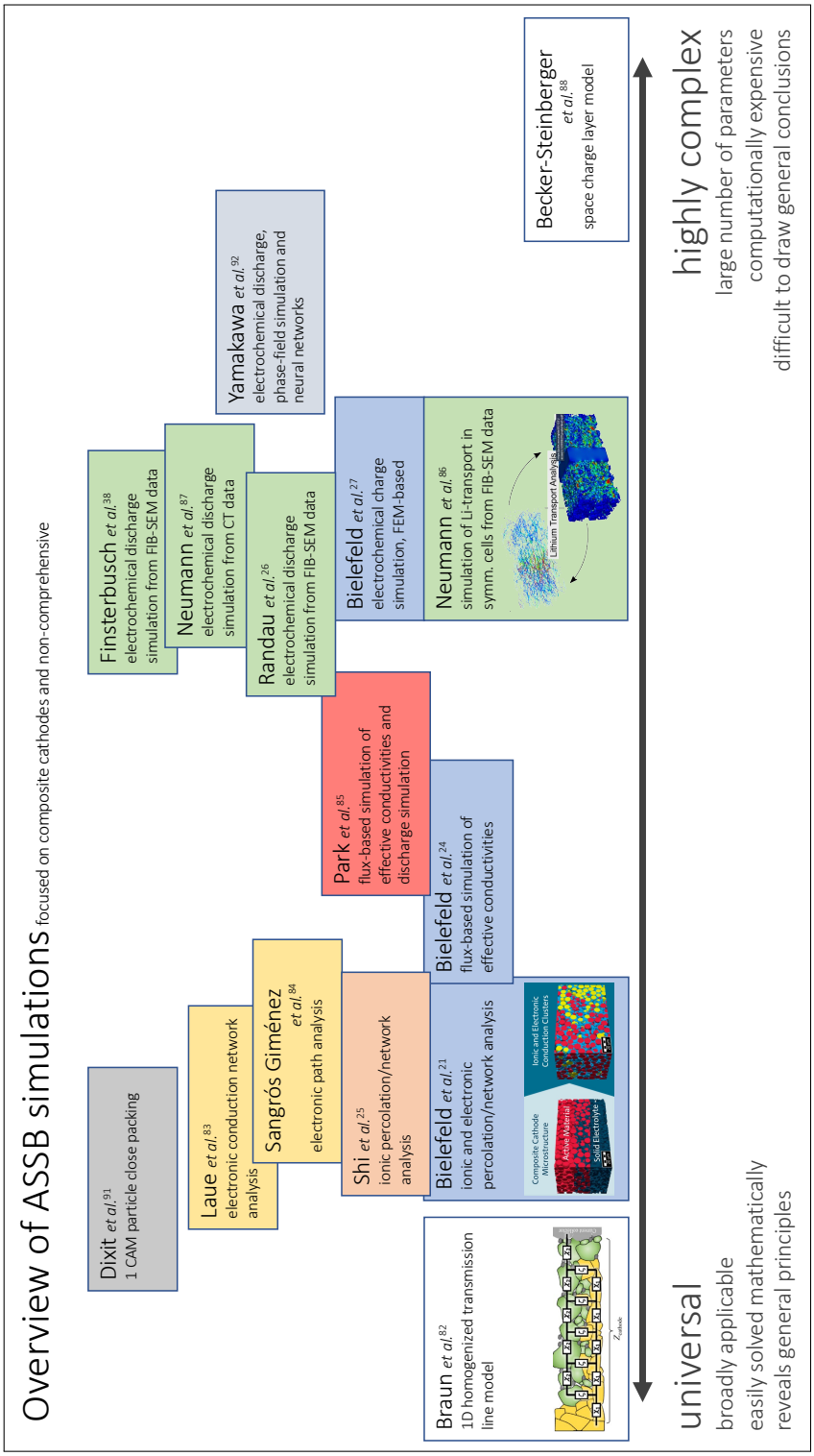

Figure 2.4.: Cutout of the ASSB simulation landscape (caption is continued on next page)

Figure 2.4.: (Continued caption) focusing on composite cathodes with schematic representations of selected models. The schematics are, from left to right, reprinted with permission from Braun et al. [82] Copyright 2018 Elsevier, adapted with permission from Bielefeld et al. [21] Copyright 2019 American Chemical Society, adapted with permission from Neumann et al. [86] Copyright 2021 American Chemical Society.

3. Results and Discussion

Not all peculiarities of ASSBs, compared to LIBs, are easily accessible in experiments, so the goal of this work is to offer explanations to observed limitations and issues from the perspective of models and simulations. Due to the morphology of oxide and thiophosphate solid electrolytes, the cathode microstructure is a key for the cell performance, but it is not straightforward to analyze by experiments. The reconstruction of cathode microstructures based on x-ray microtomography (μ-CT) or focused ion beam (FIB)-SEM is one of the few ways to analyze the microstructure in depth, but it is time-consuming and and cannot be done for numerous electrodes.
Therefore, the identification of bottlenecks can be quite challenging and the generation of synthetic microstructures or particle arrangements is a way to handle this issue. Scanning through a wide variety of electrode layouts and compositions can lead to optimizing its design.

This chapter features three publications on composite cathodes for ASSBs that approach observed limitations and issues from the modeling perspective. The articles focus on high energy NCM CAMs and thiophosphate/sulfide solid electrolytes due to their high ionic conductivity and lower Young's modulus[79,80] which is favorable to compensate volume changes that occur during (de-)lithiation of the CAM.[93]
While all publications deal with the layout of composite cathodes, the first two focus on ionic and electronic percolation and conduction, modeled in 3D voxel-based particle arrangements. The third publication models the actual electrochemistry of the cell using the FEM to approximate a set of partial differential equations that describe charge transport, (de-)intercalation and ensure charge and mass continuity. From the first to the third study, the electrode behavior is represented more detailed, culminating in a study of a sole CAM particle with voids on the surface. Naturally, the in-depth analysis is more accurate, but also computationally demanding, which makes it more difficult to get a wide overview of various electrode set-ups. Furthermore, the detailed study in the third publication relies heavily on the experimental input, whereas the percolation study of the first publication is widely independent from measured input, such as diffusion coefficients or exchange current densities.

3.1. Percolation of Ionic and Electronic Conduction Clusters (Publication 1)

The origin of the first publication lies in the limited performance that was observed in ASSBs beforehand[53,94–97] and provides the first step to an elaborate electrode layout by combining percolation theory with microstructural geometrical modeling.
The model consists of spherical secondary CAM particles that represent NCM622, polyhedral solid electrolyte particles that represent lithium phosphorus sulfide, β-Li_3PS_4 (β-LPS) and void space. Percolation theory is generally used in statistics to describe phase transitions and critical phenomena; in the case of composite electrodes, the charge carriers (lithium ions and electrons) either penetrate the electrode in its entire thickness, which is the percolating phase or reach dead ends before, which is equivalent to the non-percolating phase that entails a low usable electrode capacity. The identification of ion and electron conduction networks through the electrode allows to quantify the fraction of CAM that can be addressed upon cycling and the active interface area between NCM and β-LPS that is available for (de-)intercalation. Studying the impact of the composition, the void space, the CAM particle size and the electrode thickness, the work provides a broad overview that clarifies the conditions required for sufficient percolation.
The observation that small CAM particles are favorable for electronic percolation[53] is confirmed by the model and explained with the high surface area of the smaller particles that offers more possibilities for cluster-building. Carbon additives that are commonly used in conventional cathodes to ensure electronic percolation, have shown to degrade thiophosphate solid electrolytes and reduce the cell performance.[18,26,39] The percolation study shows that these additives are not required, if a sufficient electronic percolation is provided by a high fraction of CAM in the composite and/or small CAM particles. This finding was later experimentally verified by Minnmann et al.[20]. At the time, the void space in ASSBs was widely not considered, but was brought to the fore by this study, because its effect on the conduction clusters can be crucial. Not knowing the fraction of void space inhibits the comparison of experimental studies.
The method is also capable to identify and optimal cathode composition for a given void space fraction and particle size (distribution) which can be quite helpful, when exploring electrode layouts beyond the commonly known.

The idea was developed by D. Weber and me and the study concept was created by all authors. The modeling and the simulation setup was done by me using GeoDict 2018[98] (Version 2018, Service Pack 5) and Matlab[44] for batch processing. The manuscript was written by me and edited by all authors.
Reprinted with permission from Bielefeld, A.; Weber, D. A.; Janek, J. Microstructural Modeling of Composite Cathodes for All-Solid-State Batteries. *J. Phys. Chem. C* **2019**, *123*, 1626–1634, DOI: 10.1021/acs.jpcc.8b11043
Copyright © 2019 American Chemical Society

THE JOURNAL OF PHYSICAL CHEMISTRY C

Article

Cite This: J. Phys. Chem. C 2019, 123, 1626−1634

pubs.acs.org/JPCC

Microstructural Modeling of Composite Cathodes for All-Solid-State Batteries

Anja Bielefeld,*[,†,‡] Dominik A. Weber,[‡] and Jürgen Janek*[,†,§]

[†]Physikalisch-Chemisches Institut and [§]Center of Materials Research (LaMa), Justus-Liebig-Universität, 35392 Giessen, Germany

[‡]Volkswagen AG, Group Research, 38436 Wolfsburg, Germany

ABSTRACT: When it comes to energy density, all-solid-state batteries are seen as a promising technology for next-generation electrochemical storage devices. Nevertheless, the performance of all-solid-state cells is still very limited. The reasons are manifold, with insufficient ionic and electronic percolation within the composite cathode being a crucial one. In this work, we investigate percolation characteristics by three-dimensional microstructural modeling with the aim to define and understand boundary conditions for well-percolating networks. Utilizing spherical active material particles together with convex polyhedra as the solid electrolyte, ionic and electronic conduction clusters are determined and analyzed by means of percolation theory for varying macroscopic parameters, such as composition, porosity, particle size, and electrode thickness. Small active material particles turn out to enhance the effective electronic conductivity, offering high surface areas and thus more possibilities to connect particles, while porosity crucially affects ionic and electronic conduction capabilities. An impact of electrode thickness on the effective electronic conductivity is observed exclusively in thin electrodes, where percolation effects are suppressed implying favorable electrode properties. From microstructural modeling, ideal compositions are derived and guidelines for electrode design are developed at a given porosity and particle size of active material and solid electrolyte.

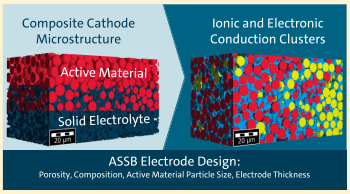

INTRODUCTION

Conventional lithium-ion batteries are expected to approach their physical limits in energy density and fast charging anytime soon,[1,2] leaving all-solid-state batteries (ASSBs) as promising candidates to promote battery technology even further: the advancement of higher energy and power densities is driven by the idea to enable lithium-metal anodes using a dense and thin but dendrite-safe, solid electrolyte (SE) separator.[3] As bulk polarization inside such a SE can practically be excluded because of sole conduction of lithium ions (single ion conductors; transference number very close to one), ASSBs may also pave the way toward higher current densities and fast charging,[4] which is an important feature for future mobility concepts.

Despite promising sulfide-based high power cells demonstrating stable cycling at a rate of 18 C at 100 °C,[5] up to date, the performance of ASSBs has been very limited in most studies.[6] The reasons are miscellaneous, and different mutually nonexclusive explanations can be drawn. The performance strongly depends on material properties (elastic, (electro-) chemical, and morphological), the compatibility of the cell components, and the cell design. For once, contact loss throughout the composite cathode occurs because of volume change of the active material (AM) during cycling, as was exemplarily shown for nickel-rich $LiNi_{0.8}Co_{0.1}Mn_{0.1}O_2$ (NCM-811) and the sulfide-based SE β-Li_3PS_4 (LPS).[7] Moreover, the formation of a space charge layer at the interface between SE and cathode,[8] dendrite formation[9] (or interfacial defect propagation along Griffith flaws[10]) and limitations in ionic and/or electronic conduction within the cathode[11,12] are reported.

In conventional liquid electrolyte systems as well as in ASSBs, electrodes have to be designed with regard to performance featuring high capacity, power, and cycling stability. These goals are achieved by providing (fast) ionic and electronic conduction pathways for charge transport, high active interface areas between electrolyte and AM for the intercalation to occur and sufficient utilization of AM. Contrary to conventional battery cells, the rigid SE does not necessarily adhere well to the surface of the AM. This has to be taken into consideration already in the process of cathode manufacturing. The impact of electrode design on the performance of ASSBs comprising shape and size (distribution) of AM and SE, porosity, and composition as well as electrode thickness is an important aspect yet to be investigated in depth for ASSBs.

To date, studies on the role of composition and particle size have been conducted and limitations for ionic as well as for electronic transport have been reported: on the one hand, a severe drop of electronic conductivity has been observed upon the increase of AM particle size (up to 20 μm), using carbon-free electrodes that consist of nickel-rich NCM-622 and the thiophosphate electrolyte LPS, indicating that small AM particles enhance cell performance.[13] Similarly, the effective

Received: November 14, 2018
Revised: December 25, 2018
Published: December 31, 2018

ACS Publications © 2018 American Chemical Society

DOI: 10.1021/acs.jpcc.8b11043
J. Phys. Chem. C 2019, 123, 1626−1634

Downloaded via VOLKSWAGEN AG on January 28, 2019 at 09:40:29 (UTC).
See https://pubs.acs.org/sharingguidelines for options on how to legitimately share published articles.

electronic conductivity in NCM-523 and $Li_2S-P_2S_5$ composites happens to be affected by the composition, indicating that a high AM/SE volume ratio enhances effective electronic conductivity, while it goes along with a decrease in effective ionic conductivity throughout the composite.[14] On the other hand, studies on the effect of electrode composition show that high mass loading of up to 85 wt% AM leads to lower capacity and weak rate capability in NCM-622/argyrodite/Super C65/nitrile butadiene rubber composite cathodes. The polymer binder and the small fraction of SE are considered as key reasons for the poor effective ionic conductivity.[11] More evidence for limitation in the ionic conduction at high mass loading of AM is provided by cycling and rate tests of electrodes, consisting of $LiCoO_2$ (LCO) and $Li_{10}GeP_2S_{12}$ (LGPS) at varying fractions,[12] as well as for composites of $Li_{3x}La_{2/3-x}TiO_3$-coated LCO and glass-ceramic LPS with Super P carbon.[15] Similarly, the porosity has been evidenced to have a significant impact on the effective ionic conductivity and therefore on tortuosity in LCO and $Li_2S-P_2S_5-LiI$ composite electrodes, analyzed by electrochemical impedance spectroscopy and focused ion beam-scanning electron microscopy reconstruction coupled with numerical simulations.[16] Moreover, thick composite cathodes of up to 600 μm have successfully been prepared and operated at room temperature using LPS and LGPS with LCO AM,[17] indicating that SEs with a transference number close to unity may enable the usage of thick high energy cathodes, while conventional liquid electrolytes tend to build up concentration gradients of the conducting salt, limiting ionic transport at high C rates.[1,18]

Even though the above-mentioned studies give indications upon composite electrode design, a holistic approach considering porosity, AM particle size, and size distribution, as well as composition and electrode thickness as parameters of interest, has not been reported, both experimentally as well as theoretically or from a modeling perspective. In this work, we analyze ionic and electronic percolation, the utilization of AM, and the resulting active interface area in an expedient number of predefined composite cathodes by microstructural modeling.

We give a short introduction on percolation theory and explain its application to microstructural modeling of composite electrodes, as well as the layout and construction of the microstructure itself. The study on the influence of AM particle size, composition, porosity, and electrode thickness allows us to predict and specify optimal conditions for high-performance composite electrodes and to understand the influence of design parameters to provide useful guidelines for electrode composition.

METHODS

In their study on microstructural connectivity, Lagadec et al.[19] conclude that all electrochemical systems can be seen as interwoven electronic and ionic networks, which have to be balanced at all length scales, providing pathways for charge transport. Accordingly, the idea of our work is to use percolation theory to model the network of ionic and electronic conduction throughout the composite cathode of ASSBs.

Percolation Theory. Percolation theory is used for the description of critical phenomena and phase transition modeling in probability theory and originates from the analysis of percolation of fluids through a (random) porous structure.[20,21]

A simulation network with occupied or unoccupied sites is created and their connectivity is examined. Identification of connected clusters is carried out starting at one chosen boundary, checking whether neighboring sites of occupied sites are occupied, as well. If so, these sites are added to the cluster. This routine continues through the whole structure, using the Hoshen–Kopelman algorithm.[22] Clusters that reach throughout the whole structure and connect both boundaries are called percolating clusters. As a result, occupied/unoccupied sites and, if present, occupied sites that belong to the percolating cluster can be discerned. Apart from the existence of percolation itself, the connectivity of the percolation cluster is an interesting characteristic.

To investigate percolation phase changes, order parameters are analyzed. These parameters are also known from theory of phase transformations and exhibit sudden value changes at the percolation threshold p_c, which is defined as the critical occupation probability at which percolation is first observed and the phase transition (non-percolating to percolating) occurs. The regions below and above the critical probability are referred to as the subcritical phase ($p < p_c$) and the supercritical phase ($p > p_c$), respectively.[21] Just above the percolation threshold, percolation law predicts the order parameter to obey a power law

$$\Theta \propto (p - p_c)^{\beta} \tag{1}$$

where Θ is the order parameter, β is the critical exponent as introduced by Grimmett[21] and p refers to the occupation probability in the critical region above and close to the threshold. In finite systems, the phase transition observed by the order parameter is expected to be smeared over an interval because of statistical variation. Only infinite systems incorporate a well-defined and discrete percolation threshold.

In ASSB electrodes, the application of percolation theory and the identification of conduction clusters may allow estimating the effective ionic and electronic conductivity close to the percolation threshold for similar microstructures. Apart from the percolation law, the threshold itself is of interest because the achievement of high performance in ASSB cells requires both ionic and electronic conduction throughout the cathode (and anode) and during the whole cell lifetime.[11]

Microstructural Modeling. Targeting a significant study design, the aim is to generate microstructures that are as simple as possible, while being representative for realistic composite cathodes at the same time. In general, composite cathodes for ASSBs consist of five components: AM, SE, conductive agent, binder, and pore volume (e.g., Nam et al.[11]). For the current microstructural percolation study, the influence of binder and conductive agent are left aside, similar to the experimental analysis performed by Strauss et al.,[13] but could in principle be added to such a microstructure model. A practical reason to consider renunciation of carbon black is that carbon additives have shown degradation reactions in contact with thiophosphate electrolytes during cycling.[7,23,24] Apart, cathode AM coatings play an important role for thiophosphate SEs, preventing electrochemical reactions of AM and SE, as well as suppressing highly resistive lithium-ion-deficient layers at the interface.[25] Different coatings on cathode AM, such as partially crystallized $Li_{56}Nb_{22}Ta_{22}$-oxide,[26] $Li_4Ti_5O_{12}$,[25] $LiNbO_3$,[27,28] and Li_2O-ZrO_2[29] have shown to improve cell performance. Concerning the percolation study, AM coatings are considered to have negligible impact on percolation

DOI: 10.1021/acs.jpcc.8b11043
J. Phys. Chem. C 2019, 123, 1626–1634

networks and therefore on effective conductivities because of their nanoscale thickness and sufficient charge transport properties.[26]

On this basis, the electronic conduction through the cathode is exclusively provided by connected AM particles, because the SE is a single ion conductor with negligible electronic conductivity. With the percolation study carried out on a three-dimensional microstructure, the outer boundary conditions for sufficiently well-connected particles are to be found.

The microstructural modeling approach in GeoDict[30] is schematically shown in Figure 1, assuming a two-component

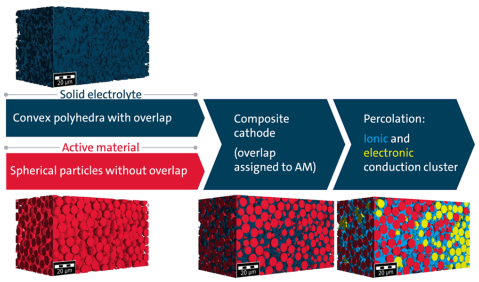

Figure 1. Microstructural modeling of composite cathodes in GeoDict,[30] featuring spherical AM particles (red), convex polyhedra as SE (dark blue) and ionic (light blue) as well as electronic (yellow) conduction clusters.

cathode consisting of two submodels, one for the SE (e.g., lithium thiophosphate electrolyte, LPS) and one for the AM particles (e.g., NCM-811). Both substructures are generated separately and merged afterwards. The AM is modeled by spherical particles with a uniform particle size distribution and no overlap. Even though leading to oversimplification, a uniform particle size is chosen in this work to isolate the influence of particle size itself from possibly biasing distribution settings. As an example, a Gaussian distribution with a given width and bi- or tri-modal distributions introduce more input parameters whose influence on percolation is to be analyzed in future studies. In sub-model-creation, the AM particles are distributed randomly throughout the microstructure, so that none of the modeled microstructures looks like the other. After creation of all particles up to a given solid volume fraction, the overlap is removed by allowing overlapping particles (one by one) to shift within a given distance. If this process does not eliminate the overlap, it is repeated 10 times for the particle. Doing so, the overlap could be minimized to around 10^{-5} vol% in most cases. The overlap removal gets difficult at elevated solid volume fractions because the particles are densely packed. In case of the highest AM volume fractions (around 65 vol%), the overlap reaches values of up to 1%, which is explicable by the proximity to the geometrical limit for dense packing of equally sized spheres at 74%.[31] Introduction of nonuniform particle distributions would shift this limits toward higher packing densities.

The SE is incorporated as convex polyhedra with overlap, which is a reasonable assumption for thiophosphate electrolytes because of their relatively low Young's modulus of ~25 GPa[32−34] and good ductility. The SE particle size corresponds to the enclosing sphere diameter. The marriage of the AM and electrolyte substructures is carried out by assigning the overlap to the AM particles for them to remain spherical. This results in a loss of SE within the composite, which has to be compensated a priori by generating a denser electrolyte substructure.

The volume which is neither filled with AM nor with SE is the pore volume V_{pore}. The fraction of pores, with respect to the microstructure volume V_{total}, is referred to as the porosity

$$\phi = \frac{V_{pore}}{V_{total}} \tag{2}$$

or, expressed in terms of volume filled by AM V_{AM} and SE V_{SE}

$$\phi = 1 - \frac{V_{AM} + V_{SE}}{V_{total}} \tag{3}$$

Calculating the volume fractions of AM and SE for microstructure construction, one has to distinguish volume fractions with respect to the total structure volume with superscript V, taking porous volume into account, from volume fractions with respect to the solid phase only. These are referred to by superscript S and can directly be found in the composition indication. At given composition and porosity, the fraction of AM in the whole volume g^{V}_{AM}, including porosity, can then be calculated as

$$g^{V}_{AM} = (1 - g^{S}_{SE})(1 - \phi) \tag{4}$$

while the electrolyte fraction is adjusted to

$$g^{V}_{SE} = \frac{(1 - \phi)}{(1 - \phi) + \frac{\phi}{g^{S}_{SE}}} \tag{5}$$

Equation 5 calculates the solid volume fraction that has to be occupied by electrolyte in the SE-substructure. Hence, at the point of SE-substructure generation, AM is not yet present but will later (in the marriage) consume parts of the SE-substructure, so that finally the desired composition and/or porosity is achieved.

Combining the microstructure with the material properties, the ionic and electronic conduction clusters can be identified. Due to the fact that desirable SEs are purely ion conductors and do not provide any electronic conduction paths, they only contribute to the ionic conduction cluster. The AM is assumed to have negligible ionic conductivity compared with the electrolyte (about 5 to 6 orders of magnitude lower[35]) and is therefore solely assigned to the electronic conduction cluster.

These clusters are computed by checking for connected components, starting from one boundary plane, which is fully connected to either the current collector in the electronic case or to the SE separator in the ionic conduction case. In Figure 1, these conduction clusters are shown in yellow (electronic) and light blue (ionic), respectively.

To model thick electrodes that reflect the demands of future solid-state technology, a relatively large electrode thickness of 140 μm is chosen at a resolution of 200 nm, which is reasonable to model particle sizes down to 3 μm. The general microstructural modeling input parameters can be found in Table 1.

RESULTS AND DISCUSSION

For the evaluation of ionic and electronic percolation in composite cathode microstructures, different microstructural parameters, reflecting the percolation properties, can be studied.

DOI: 10.1021/acs.jpcc.8b11043
J. Phys. Chem. C 2019, 123, 1626−1634

Table 1. General Microstructural Modeling Input Parameters

parameter	value
microstructure dimensions	(80 × 80 × 140) μm^3
resolution	0.2 μm/voxel
shape of AM	spherical
particle size of AM	{3,4,5,6,7,8,9,10,15} μm
particle size distribution of AM	uniform
shape of SE	convex polyhedra
particle size of SE	3 μm

A comparison of the volume fraction of both solid components allows computing the utilization level, which, for example, indicates the ratio of the volume of AM that is assigned to the conduction cluster and the volume of AM that is not part of the cluster and therefore lost in terms of battery performance. The utilization level can be expressed as

$$\theta_\nu = \frac{V_c}{V_\nu} \tag{6}$$

where subscript c refers to the cluster, either ionic or electronic, and ν refers to the solid component, either AM or SE.

Other than that, the surface area A_{spec}, specific to the structure volume and measured in m^2/m^3, can be computed for the ionic or electronic cluster separately or as the active interface area between the ionic and the electronic conduction cluster $A_{spec,a}$. In terms of cell performance, the active interface area is the area available for intercalation of lithium ions into the AM and should be maximized to assure high energy and power density. Apart from ionic intercalation, electronic conduction has to be assured as well: the AM is assumed to be the only electronically conducting material in the modeled composite, so electrons have to be transferred from one AM particle to the other. In the current study, because of the percolation theory approach, conduction networks are analyzed. These do not take into account possible resistances occurring at particle−particle interfaces and constriction resistances which reflect the fact, that electric contacts have to be regarded as a large number of interacting mircrocontacts.[36]

Electronic Conduction. We will first consider electronic conduction clusters only, varying the fraction of AM in the microstructures. Furthermore, the impact of particle size is examined by generation of microstructures with particle sizes between 3 and 15 μm, demonstrating the applicability of the power law of percolation theory (see eq 1). As an example, Figure 2 presents three microstructures and their electronic conduction clusters, all at an AM fraction of 55 vol%. From left to right, the AM particle sizes grow from 5 to 15 μm. The electronic cluster percolates well for the small particles, whereas medium-sized particles involve a smaller utilization level of AM and the large particles do not feature a percolating cluster, at all.

Computation of utilization level and specific surface area for different AM fractions shows a percolation transition for 5 μm-sized particles (Figure 3). According to their definitions, both properties obey the same curve progression: when more AM is used and the utilization level rises, the surface area of the electronic cluster increases. At this point, the main difference is that the utilization level is a normalized property, whereas the change for the absolute values of the surface area depends on particle size. For AM fractions below 48 vol%, both values are very low, indicating that the particles are poorly connected and the conduction cluster does not reach far into the composite microstructure. The small perturbation at 45 vol% is due to the fact that these data points are based on one particle arrangement for each volume fraction. In the transition region between 48 and 52 vol%, 10 random microstructures were computed for each fraction to avoid too high uncertainties and to attain a statistically more profound conclusion. The uncertainties arise because of statistical fluctuations from particle arrangement to particle arrangement. Depending on the random packing, some arrangements percolate with AM utilization levels around 70%, while others, at the same AM fraction, do not percolate and therefore exhibit utilization levels around 30%. In this region, the utilization level steeply increases, indicating that the transition takes place, while above 52 vol% AM fraction, the gradient diminishes and both characteristics reach a saturation-like level, where the volume-specific surface area is close to the geometric maximum

$$A_{spec,geo} = g_{AM}^{V} \frac{A_{sphere}}{V_{sphere}} = g_{AM}^{V} \frac{6}{d} \tag{7}$$

and only few particles remain isolated.

To verify, whether the power law of percolation theory (eq 1) is applicable for this kind of particle arrangements, the specific surface area just above the percolation threshold of the electronic cluster was calculated for a particle size of 10 μm, based on eight particle arrangements for each AM packing density. The data in the log−log plot in Figure 4 can indeed be fitted by a power law with a critical exponent of 0.41, even though the error bars, computed as the standard deviation, tend to become large in the vicinity of the transition. The particle size was arbitrarily chosen, and we expect the power law to apply for any of the particle sizes studied in this work. The critical exponent of 0.41 is in good agreement with a study of 3D site-percolation in a simple cubic lattice performed by Sur et al.,[37] indicating that the power law of percolation is applicable.

Model arrangements with particle sizes between 3 and 15 μm were built to compare the findings for 5 μm to other particle sizes. As before, one microstructure was computed for each AM fraction in sub- and super-critical regions and 10

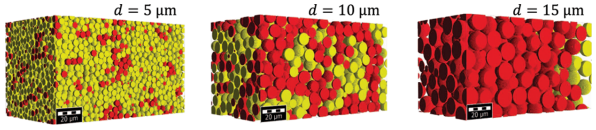

Figure 2. Exemplary AM microstructures at 55 vol% fraction for {5,10,15} μm particle diameter and respective electronic clusters (yellow). Unconnected particles are shown in red.

DOI: 10.1021/acs.jpcc.8b11043
J. Phys. Chem. C 2019, 123, 1626−1634

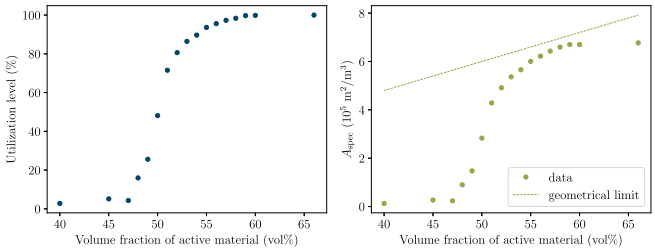

Figure 3. Utilization level of AM (left) and specific surface area of the electronic conduction cluster (right) at varying fraction of AM with 5 μm diameter. The geometrical limit (eq 7) of the specific surface area is indicated by the dashed line.

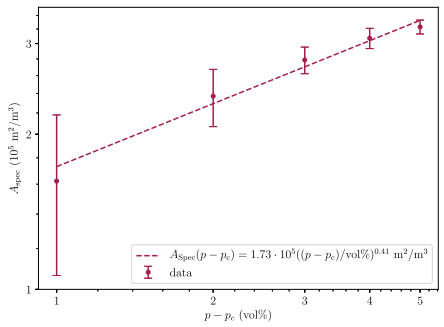

Figure 4. Specific surface area of the electronic cluster above percolation threshold for arbitrarily chosen AM particle size d = 10 μm featuring the power law predicted by percolation theory with a critical exponent of β = 0.41. The surface area is computed on the basis of eight particle arrangements for each packing density.

microstructures for each fraction in the transition region to avoid fluctuations. The utilization level and specific surface area for all different particle sizes are shown in Figure 5. As observed before (arrangements in Figure 2), smaller particles are in general more likely to develop percolation clusters at low AM fractions than larger particles. While the transition region of 3 μm particles is located within the interval of 41−46 vol%, it shifts toward higher fractions up to the interval of 52−57 vol% for 15 μm-sized particles. The steepness of the transition region is similar for all particle sizes. Here, the difference in the behaviors of utilization level and specific surface area can be observed: the smaller the particles, the higher the specific surface area gets. To quantify the effect of particle size, the percolation threshold is defined to be the AM volume fraction at which the majority of the 10 arrangements features a percolating cluster. This corresponds to the AM volume fraction at which the mean utilization level is at 40 vol%. These thresholds with respect to the particle size are presented in Figure 6 and can be fitted by

$$p_c = [7.83 \ln(d/\mu\text{m}) + 36.67] \text{ vol\%} \quad (8)$$

indicating a logarithmic relationship between the AM particle size and percolation threshold.

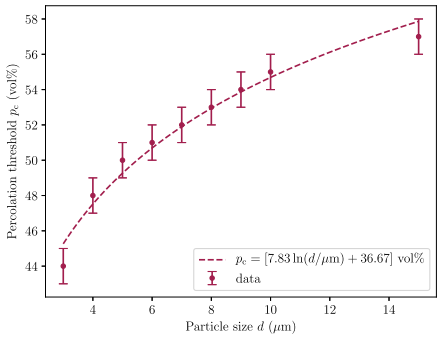

Figure 6. Dependence of the percolation threshold (in vol% of AM) of the electronic conduction cluster on AM particle size, fitted by a logarithmic function, which represents the data sufficiently accurate.

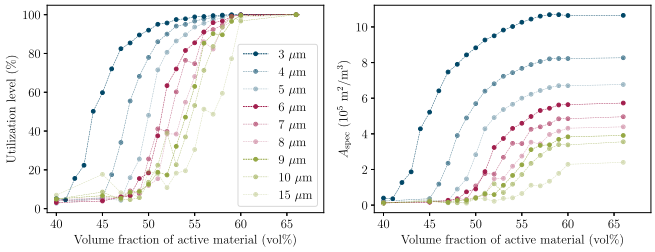

Figure 5. Utilization level of AM (left) and specific surface area of the electronic conduction cluster (right) at varying fraction of AM for various AM particle sizes between 3 and 15 μm.

DOI: 10.1021/acs.jpcc.8b11043
J. Phys. Chem. C 2019, 123, 1626−1634

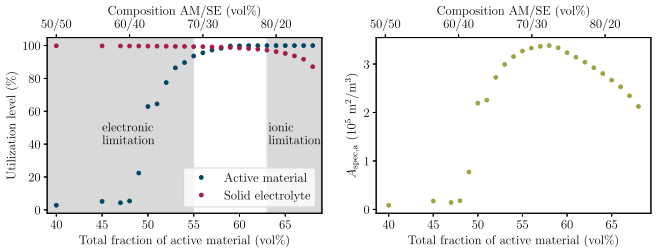

Figure 7. Utilization level of AM and SE (left) and specific active interface area between the ionic and electronic conduction cluster (right) for composite cathode arrangements at a constant porosity of 20% and AM particle size d = 5 μm. The lower x-axis reflects the total fraction of AM in the whole electrode, including porous space and SE, while the composition shown in the upper x-axis reflects the AM and SE volume in the solid phase, only.

These findings correlate well with the observation of high fractions of inactive NCM-622 for large AM particle sizes, measured via ex situ X-ray diffraction and with their attributed low effective electronic conductivity studied by Strauss et al.[13] As large AM particles exhibit a smaller surface area, they offer less possibilities for percolating electronic clusters and thus lead to lower effective electronic conductivity. Unfortunately, the total packing density of AM used by Strauss et al.[13] is not known, as the porosity was not measured.

Overall and according to the microstructural modeling, the effective electronic conduction within carbon-free composite cathodes is highly dependent on the packing density of the AM particles and on their size. Dense packing enables more intimate contact and higher connectivity between AM particles, increases the fraction of active (connected) particles, and therefore enhances electrode performance. Besides, small particles enable high utilization levels at lower packing density and might hence be a possibility to compensate for high porosities, even though the high surface area is vulnerable for chemical degradation and formation of passivating cathode/electrolyte interfacial layers upon charging,[7] which may result in performance decrease.

Ionic Conduction. In addition to the electronically conducting microstructures, we will now take ionic conduction into account and examine its characteristics. Because small AM particles suggested good performance in the previous section and an AM particle diameter of 5 μm, according to Strauss et al.,[13] is realistic for NCM-particles, this size is chosen for the calculation in this section. As the cathode composition and its porosity are not well-defined for a given total fraction of AM, two cases are distinguished: constant porosity at varying composition and constant composition at varying porosity.

In the case of constant porosity, the composition (namely g^S_{AM}/g^S_{SE}) is calculated by

$$g^S_{AM} = \frac{g^V_{AM}}{1-\phi} \tag{9}$$

the two substructures are merged and the conduction clusters are computed as described previously. As before, g^V_{AM} is the AM fraction with respect to the total structure volume involving pore volume. It is also referred to as the total fraction of AM and has to be distinguished from the AM fraction in the solid phase g^S_{AM}, which does not include pore volume but can be found directly in the composition indication.

For a porosity of 20%, the resulting utilization levels of AM and SE, as well as the volume-specific interface area, are shown in Figure 7. The presented utilization level reveals the limitations for cathode performance. While electronic conduction is the limiting factor at compositions below 69 vol% AM and 31 vol% SE (referred to as 69/31 vol%, subsequently), ionic conduction becomes restricting at high AM fractions and compositions above 79/21 vol%. Accordingly, the interval of well-performing composites is fairly small. Even though designed to overlap in the model, the SE does not suffice to build well-connected ionic conduction clusters in highly AM-dominated microstructures. Correspondingly, the active interface area diminishes at higher AM fraction and an optimal composition can be identified at 72/28 vol% which corresponds to 86/14 wt% for NMC-622 and LPS.

In an analogous manner, the ideal composition can be modeled for other porosities, as demonstrated in Figure 8 for

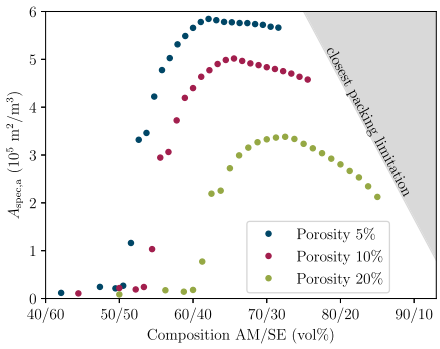

Figure 8. Specific active interface area between the ionic and electronic conduction cluster at different porosities for 5 μm-sized AM particles.

5, 10, and 20% porosity. As small porosities go along with high packing density and high mass loading, the active interfaces are significantly higher for 5% porosity than for 10 or 20%. Moreover, the electronic percolation transition takes place with smaller AM fractions than for more porous microstructures. Accordingly, an optimal composition is reached at 62/38 vol% (80/20 wt% for NMC-622 and LPS) for 5% porosity, whereas 10% porosity features an optimal composition of 66/34 vol%

DOI: 10.1021/acs.jpcc.8b11043
J. Phys. Chem. C 2019, 123, 1626−1634

The Journal of Physical Chemistry C Article

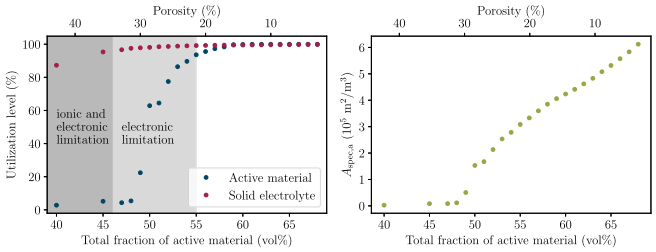

Figure 9. Porosity dependence of the utilization level of AM and SE (left) and the specific active interface area between the ionic and electronic conduction cluster (right) for composite cathode microstructures at a constant composition of 70/30 vol% AM with electrolyte and AM particle size d = 5 μm. The lower x-axis reflects the total fraction of AM in the whole microstructure including porous space and SE.

(82/18 wt% for NMC-622 and LPS). Apart from the shift of the optimal composition toward higher AM fractions for rising porosity, the ionic conduction limitation gains importance for higher porosities: the drop at compositions above the optimum is more pronounced at a porosity of 20% compared to 5 and 10%.

Keeping a constant composition and varying the porosity, the effect of densification of composite electrodes can be studied. Figure 9 shows the percolation properties for porosities from 43% down to 3% at a composition of 70/30 vol%. Evaluating the utilization of both materials, high porosities above 34% are accompanied by ionically and electronically isolated regions in the cathode. The active interface is negligible in this section and increases for porosities below 30%. Down to 21% porosity, the electronic limitation is still present, but below this value, the cathodes ought to perform well. The behavior of the active interface area in Figure 9 is not as significant as in the case of constant porosity because a lowering of porosity goes along with densification of the electrode and thus more particles (both AM and SE) in the microstructure become connected, leading to higher surface areas. The reader may bear in mind that the active interface area is not normalized with respect to porosity but with respect to the electrode volume.

Electrode Thickness. Another key issue in composite electrode design for high-energy batteries is the electrode thickness: how thick can an electrode get that performs well, even at higher C rates?[38,39] Percolation represents one important aspect in the description of thick electrodes: sufficient conduction networks are required, but diffusion lengths in the storage phase, tortuosity, and resulting effective conductivities play an additional role in thick electrodes and are not explicitly treated in this study.

To analyze the effects of electrode thickness on ionic and electronic percolation, the initially created particle arrangements of 140 μm thickness were cut at different thicknesses between 20 and 120 μm. The associated active interface areas are shown in Figure 10 for varying compositions at 20% porosity. For most thicknesses, the active interface area is very similar throughout the whole composition range. The optimum is located at the same composition for all electrode arrangements studied, but the curve shape below the optimum differs, especially for thin electrodes. This is due to the electronic conduction cluster, whose starting point is located at the current collector side of the composite. In thin electrode microstructures, the initially connected particles take a higher fraction of the whole structure. Therefore, the specific active

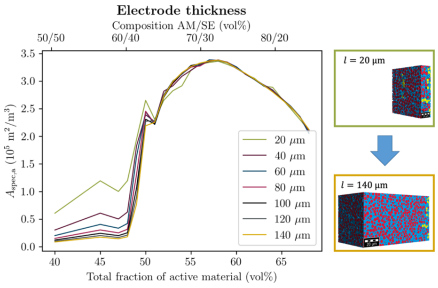

Figure 10. Specific interface area between the electronic and ionic cluster for different electrode thicknesses between 20 and 140 μm at a constant porosity of 20% and an AM particle size of d = 5 μm. The lower x-axis reflects the total fraction of AM in the whole composite, including porous space and SE, while the composition shown in the upper x-axis reflects the AM and SE volume in the solid phase, only. The microstructure models for minimal and maximal electrode thickness at 47 vol% AM fraction are shown (right).

interface area is enhanced for thin electrodes even for low AM fractions. Furthermore, a slight shift in the percolation threshold can be observed: thin composites tend to percolate at smaller AM fractions, even though the shift is not as distinct as it was for different particle sizes. As a result, percolation effects are suppressed in thin electrodes, giving the impression of favorable electrode properties. This is a direct effect of the reduced model size, also known as a finite size effect. The microstructures on the right of Figure 10 illustrate this phenomenon at an AM fraction of 47 vol% for an AM particle size of 5 μm. In contrast to the electronic conduction, ionic conduction is not affected by the electrode thickness: The drop of volume-specific active interface area (compare Figure 7) is indistinguishable for all thicknesses.

This shows that, solely judged by microstructural modeling, thick electrodes could provide conduction clustering properties comparable to those of thin electrodes. Even though the modeling technique does certainly not account for long diffusion paths and can therefore not directly reflect the charging and discharging performance, it is very efficient in identifying conduction clusters of composite cathodes based on particle size, shape, and overlap properties.

The method has the potential to serve as a basis for studying composite electrode's behavior in more detail, incorporating the mathematical modeling of electrochemical reactions or the

DOI: 10.1021/acs.jpcc.8b11043
J. Phys. Chem. C 2019, 123, 1626−1634

transformation of particle arrangements into resistor networks as performed by Sunde[40] and Ott et al.[41] for fuel cells.

CONCLUSIONS

We have established a microstructural modeling method with the aim to asses the electronic and ionic percolation behavior of composite cathodes for ASSBs. Consisting of AM and SE, the resulting composite microstructures represent carbon-free solid-state cathodes, as experimentally corroborated by Strauss et al.[13] Ionic and electronic conduction clusters have been calculated according to percolation theory and the resulting utilization levels and active interface areas were evaluated. Porosity, composition, electrode thickness, and AM particle size were taken into account to collect information on how to design composite cathodes. We ultimately found that boundary conditions for well-connected cathodes can be defined.

In particular, small AM particles are desirable in terms of electronic conduction in carbon-free composites because they offer higher active surface areas and more possibilities to form percolating electronic clusters. Contrariwise, high AM surfaces may enhance degradation processes at the cathode electrolyte interface and therefore negatively influence cell performance.[7]

Although not provided in many studies,[5,7,11−15,17] the porosity has shown to be an important property for ASSB composite electrodes that can crucially influence conduction clusters and therefore cell performance. Accordingly, we strongly propose for future experimental studies to take the impact of porosity into account. It is worthwhile to make the effort and measure or calculate this important characteristic for the sake of comparability between experimental studies. As expected, small porosities are favorable in terms of conduction clustering, which leads to the necessity of manufacturing low-porous electrodes as proposed by Kim et al.,[42] who infiltrated a sulfide-based SE into conventional LCO and graphite Li-ion battery electrodes, achieving calculated porosities around 6−8% and demonstrating intimate ionic contacts.

Moreover, we have managed to identify ideal compositions that ensure both ionic and electronic conduction at given porosities, based on pure microstructural modeling, in which no material characteristics except for the particle's shape, size, and overlap behavior have been used. Anyhow, the effective conductivity optimum may differ from the optimum in specific active interface area, especially for the electronic cluster, because therein the AM particles are designed to avoid overlap and, at low AM fraction, are mainly connected by point contacts leaving aside constriction resistances. At higher fractions, the overlap increases and the connection of the interfaces of the AM particles is improved.

In general, real solid-state battery cells are a time-variant system and the initial composition may change during cycling, incorporating particle cracks, volume changes, and other mechanical or (electro-)chemical issues.[43] AM coating, binder, and conductive agent may influence the performance as well as inhomogeneities in the electrode composition, which may arise because of processing conditions and lead to nonuniform current distribution that causes even more difficulties. However, these issues are beyond the scope of this study, whose intent is to provide design guidelines and a performance estimation, forming a foundation for microstructural modeling of all-solid-state batteries which offers multiple possibilities to be expanded.

AUTHOR INFORMATION

Corresponding Authors

*E-mail: anja.bielefeld@volkswagen.de (A.B.).
*E-mail: juergen.janek@phys.chemie.uni-giessen.de (J.J.).

ORCID

Anja Bielefeld: 0000-0003-2193-8375
Jürgen Janek: 0000-0002-9221-4756

Notes

The authors declare no competing financial interest.

ACKNOWLEDGMENTS

The authors thank the consortium of the "FELIZIA" project (03XO0026G), funded by the German Federal Ministry of Education and Research (BMBF) for fruitful discussions.

REFERENCES

(1) Gallagher, K. G.; Trask, S. E.; Bauer, C.; Woehrle, T.; Lux, S. F.; Tschech, M.; Lamp, P.; Polzin, B. J.; Ha, S.; Long, B.; et al. Optimizing Areal Capacities through Understanding the Limitations of Lithium-Ion Electrodes. *J. Electrochem. Soc.* **2016**, *163*, A138−A149.

(2) Luntz, A. C.; Voss, J.; Reuter, K. Interfacial Challenges in Solid-State Li Ion Batteries. *J. Phys. Chem. Lett.* **2015**, *6*, 4599−4604.

(3) Zhang, Z.; Shao, Y.; Lotsch, B.; Hu, Y.-S.; Li, H.; Janek, J.; Nazar, L. F.; Nan, C.-W.; Maier, J.; Armand, M.; et al. New Horizons for Inorganic Solid State Ion Conductors. *Energy Environ. Sci.* **2018**, *11*, 1945−1976.

(4) Janek, J.; Zeier, W. G. A Solid Future for Battery Development. *Nat. Energy* **2016**, *1*, 16141.

(5) Kato, Y.; Hori, S.; Saito, T.; Suzuki, K.; Hirayama, M.; Mitsui, A.; Yonemura, M.; Iba, H.; Kanno, R. High-Power All-Solid-State Batteries using Sulfide Superionic Conductors. *Nat. Energy* **2016**, *1*, 16030.

(6) Wu, B.; Wang, S.; Evans, W. J., IV; Deng, D. Z.; Yang, J.; Xiao, J. Interfacial Behaviours between Lithium Ion Conductors and Electrode Materials in Various Battery Systems. *J. Mater. Chem. A* **2016**, *4*, 15266−15280.

(7) Koerver, R.; Aygün, I.; Leichtweiß, T.; Dietrich, C.; Zhang, W.; Binder, J. O.; Hartmann, P.; Zeier, W. G.; Janek, J. Capacity Fade in Solid-State Batteries: Interphase Formation and Chemomechanical Processes in Nickel-Rich Layered Oxide Cathodes and Lithium Thiophosphate Solid Electrolytes. *Chem. Mater.* **2017**, *29*, 5574−5582.

(8) Yamamoto, K.; Iriyama, Y.; Asaka, T.; Hirayama, T.; Fujita, H.; Fisher, C. A. J.; Nonaka, K.; Sugita, Y.; Ogumi, Z. Dynamic Visualization of the Electric Potential in an All-Solid-State Rechargeable Lithium Battery. *Angew. Chem., Int. Ed.* **2010**, *49*, 4414−4417.

(9) Raj, R.; Wolfenstine, J. Current Limit Diagrams for Dendrite Formation in Solid-State Electrolytes for Li-Ion Batteries. *J. Power Sources* **2017**, *343*, 119−126.

(10) Kerman, K.; Luntz, A.; Viswanathan, V.; Chiang, Y.-M.; Chen, Z. Review-Practical Challenges Hindering the Development of Solid State Li Ion Batteries. *J. Electrochem. Soc.* **2017**, *164*, A1731−A1744.

(11) Nam, Y. J.; Oh, D. Y.; Jung, S. H.; Jung, Y. S. Toward Practical All-Solid-State Lithium-Ion Batteries with High Energy Density and Safety: Comparative Study for Electrodes Fabricated by Dry- and Slurry-Mixing Processes. *J. Power Sources* **2018**, *375*, 93−101.

(12) Zhang, W.; Weber, D. A.; Weigand, H.; Arlt, T.; Manke, I.; Schröder, D.; Koerver, R.; Leichtweiss, T.; Hartmann, P.; Zeier, W. G.; et al. Interfacial Processes and Influence of Composite Cathode Microstructure Controlling the Performance of All-Solid-State Lithium Batteries. *ACS Appl. Mater. Interfaces* **2017**, *9*, 17835−17845.

(13) Strauss, F.; Bartsch, T.; de Biasi, L.; Kim, A.-Y.; Janek, J.; Hartmann, P.; Brezesinski, T. Impact of Cathode Material Particle

DOI: 10.1021/acs.jpcc.8b11043
J. Phys. Chem. C 2019, 123, 1626−1634

Size on the Capacity of Bulk-Type All-Solid-State Batteries. *ACS Energy Lett.* **2018**, *3*, 992−996.
(14) Siroma, Z.; Sato, T.; Takeuchi, T.; Nagai, R.; Ota, A.; Ioroi, T. AC Impedance Analysis of Ionic and Electronic Conductivities in Electrode Mixture Layers for an All-Solid-State Lithium-Ion Battery. *J. Power Sources* **2016**, *316*, 215−223.
(15) Noh, S.; Nichols, W. T.; Park, C.; Shin, D. Enhanced Energy Density and Electrochemical Performance of All-Solid-State Lithium Batteries through Microstructural Distribution of Solid Electrolyte. *Ceram. Int.* **2017**, *43*, 15952−15958.
(16) Hlushkou, D.; Reising, A. E.; Kaiser, N.; Spannenberger, S.; Schlabach, S.; Kato, Y.; Roling, B.; Tallarek, U. The Influence of Void Space on Ion Transport in a Composite Cathode for All-Solid-State Batteries. *J. Power Sources* **2018**, *396*, 363−370.
(17) Kato, Y.; Shiotani, S.; Morita, K.; Suzuki, K.; Hirayama, M.; Kanno, R. All-Solid-State Batteries with Thick Electrode Configurations. *J. Phys. Chem. Lett.* **2018**, *9*, 607−613.
(18) Arora, P.; Doyle, M.; Gozdz, A. S.; White, R. E.; Newman, J. Comparison between Computer Simulations and Experimental Data for High-Rate Discharges of Plastic Lithium-Ion Batteries. *J. Power Sources* **2000**, *88*, 219−231.
(19) Lagadec, M. F.; Zahn, R.; Müller, S.; Wood, V. Topological and Network Analysis of Lithium Ion Battery Components: The Importance of Pore Space Connectivity for Cell Operation. **2018**, pp 1−8, ArXiv e-prints.
(20) Kesten, H. *Percolation Theory for Mathematicians; Progress in Probability and Statistics*; Birkhäuser, 1982; Vol. *2*.
(21) Grimmett, G. In *Lectures on Probability Theory and Statistics: Ecole d'Eté de Probabilités de Saint-Flour XXVI-1996*; Bernard, P., Ed.; Springer Berlin Heidelberg: Berlin, Heidelberg, 1997; pp 153−300.
(22) Hoshen, J.; Kopelman, R. Percolation and Cluster Distribution. I. Cluster Multiple Labeling Technique and Critical Concentration Algorithm. *Phys. Rev. B: Solid State* **1976**, *14*, 3438−3445.
(23) Zhang, W.; Leichtweiß, T.; Culver, S. P.; Koerver, R.; Das, D.; Weber, D. A.; Zeier, W. G.; Janek, J. The Detrimental Effects of Carbon Additives in Li10GeP2S12-Based Solid-State Batteries. *ACS Appl. Mater. Interfaces* **2017**, *9*, 35888−35896.
(24) Hakari, T.; Deguchi, M.; Mitsuhara, K.; Ohta, T.; Saito, K.; Orikasa, Y.; Uchimoto, Y.; Kowada, Y.; Hayashi, A.; Tatsumisago, M. Structural and Electronic-State Changes of a Sulfide Solid Electrolyte during the Li Deinsertion-Insertion Processes. *Chem. Mater.* **2017**, *29*, 4768−4774.
(25) Ohta, N.; Takada, K.; Zhang, L.; Ma, R.; Osada, M.; Sasaki, T. Enhancement of the High-Rate Capability of Solid-State Lithium Batteries by Nanoscale Interfacial Modification. *Adv. Mater.* **2006**, *18*, 2226−2229.
(26) Yada, C.; Lee, C. E.; Laughman, D.; Hannah, L.; Iba, H.; Hayden, B. E. A High-Throughput Approach Developing Lithium-Niobium-Tantalum Oxides as Electrolyte/Cathode Interlayers for High-Voltage All-Solid-State Lithium Batteries. *J. Electrochem. Soc.* **2015**, *162*, A722−A726.
(27) Ohta, N.; Takada, K.; Sakaguchi, I.; Zhang, L.; Ma, R.; Fukuda, K.; Osada, M.; Sasaki, T. $LiNbO_3$-coated $LiCoO_2$ as cathode material for all solid-state lithium secondary batteries. *Electrochem. Commun.* **2007**, *9*, 1486−1490.
(28) Ohtomo, T.; Hayashi, A.; Tatsumisago, M.; Tsuchida, Y.; Hama, S.; Kawamoto, K. All-solid-state lithium secondary batteries using the $75Li_2S{\cdot}25P_2S_5$ glass and the $70Li_2S{\cdot}30P_2S_5$ glass-ceramic as solid electrolytes. *J. Power Sources* **2013**, *233*, 231−235.
(29) Ito, S.; Fujiki, S.; Yamada, T.; Aihara, Y.; Park, Y.; Kim, T. Y.; Baek, S.-W.; Lee, J.-M.; Doo, S.; Machida, N. A rocking chair type all-solid-state lithium ion battery adopting Li_2O-ZrO_2 coated $LiNi_{0.8}Co_{0.15}Al_{0.05}O_2$ and a sulfide based electrolyte. *J. Power Sources* **2014**, *248*, 943−950.
(30) Math2Market GmbH, K. G. *GeoDict—The Digital Material Laboratory*, Version 2018 SP 5, 2018.
(31) Tóth, L. F. *Dichteste Kugelpackung. Eine Idee von Gauß; Abhandlungen der Braunschweigischen Wissenschaftlichen Gesellschaft*; Goltze: Göttingen, 1977; Vol. 27.
(32) Sakuda, A.; Hayashi, A.; Tatsumisago, M. Sulfide Solid Electrolyte with Favorable Mechanical Property for All-Solid-State Lithium Battery. *Sci. Rep.* **2013**, *3*, 2261.
(33) Yang, Y.; Wu, Q.; Cui, Y.; Chen, Y.; Shi, S.; Wang, R.-Z.; Yan, H. Elastic Properties, Defect Thermodynamics, Electrochemical Window, Phase Stability, and Li^+ Mobility of Li_3PS_4: Insights from First-Principles Calculations. *ACS Appl. Mater. Interfaces* **2016**, *8*, 25229−25242.
(34) Deng, Z.; Wang, Z.; Chu, I.-H.; Luo, J.; Ong, S. P. Elastic Properties of Alkali Superionic Conductor Electrolytes from First Principles Calculations. *J. Electrochem. Soc.* **2015**, *163*, A67−A74.
(35) Amin, R.; Chiang, Y.-M. Characterization of Electronic and Ionic Transport in $Li_{1-x}Ni_{0.33}Mn_{0.33}Co_{0.33}O_2$(NMC333) and Li1-xNi0.50Mn0.20Co0.30O2(NMC523) as a Function of Li Content. *J. Electrochem. Soc.* **2016**, *163*, A1512−A1517.
(36) Greenwood, J. A. Constriction Resistance and the Real Area of Contact. *Br. J. Appl. Phys.* **1966**, *17*, 1621.
(37) Sur, A.; Lebowitz, J. L.; Marro, J.; Kalos, M. H.; Kirkpatrick, S. Monte Carlo Studies of Percolation Phenomena for a Simple Cubic Lattice. *J. Stat. Phys.* **1976**, *15*, 345−353.
(38) Singh, M.; Kaiser, J.; Hahn, H. Thick Electrodes for High Energy Lithium Ion Batteries. *J. Electrochem. Soc.* **2015**, *162*, A1196−A1201.
(39) Danner, T.; Singh, M.; Hein, S.; Kaiser, J.; Hahn, H.; Latz, A. Thick Electrodes for Li-Ion Batteries: A Model Based Analysis. *J. Power Sources* **2016**, *334*, 191−201.
(40) Sunde, S. Simulations of Composite Electrodes in Fuel Cells. *J. Electroceram.* **2000**, *5*, 153−182.
(41) Ott, J.; Völker, B.; Gan, Y.; McMeeking, R. M.; Kamlah, M. A Micromechanical Model for Effective Conductivity in Granular Electrode Structures. *Acta Mech. Sin.* **2013**, *29*, 682−698.
(42) Kim, D. H.; Oh, D. Y.; Park, K. H.; Choi, Y. E.; Nam, Y. J.; Lee, H. A.; Lee, S.-M.; Jung, Y. S. Infiltration of Solution-Processable Solid Electrolytes into Conventional Li-Ion-Battery Electrodes for All-Solid-State Li-Ion Batteries. *Nano Lett.* **2017**, *17*, 3013−3020.
(43) Koerver, R.; Zhang, W.; de Biasi, L.; Schweidler, S.; Kondrakov, A. O.; Kolling, S.; Brezesinski, T.; Hartmann, P.; Zeier, W. G.; Janek, J. Chemo-Mechanical Expansion of Lithium Electrode Materials - On the Route to Mechanically Optimized All-Solid-State Batteries. *Energy Environ. Sci.* **2018**, *11*, 2142−2158.

DOI: 10.1021/acs.jpcc.8b11043
J. Phys. Chem. C 2019, 123, 1626−1634

3.2. Effective Ionic Conductivity and the Influence of Binders (Publication 2)

Another issue for ASSBs to play a significant role in the transformation to e-mobility is their industrialization that requires large scale roll-to-roll processing. Adopting manufacturing steps from the conventional LIBs to ASSBs is economically appealing, so wet slurry cathode fabrication was brought to the fore, which requires the use of polymeric binders and these have shown to crucially affect the cell performance.[94,99–101]

The study goals were to understand in what conditions binders limit the ionic percolation and how they influence the effective ionic conductivity as well as to refine what application-based requirements, such as high energy or high performance cell layouts, imply for the cell, its microstructure and materials. Therefore, the effect of the electrode composition, the CAM particle size, the void space and the binder content was investigated in 3D microstructure models, similar to the first publication but with an additional component – the binder. The percolation network analysis was combined with a stationary, flux-based simulation of the effective ionic conductivity and tested on the cathode reported by Kato et al. [13].

One way to view an electrode is as interwoven ion and electron networks that result in a maze for the charge carriers. To describe how winding the mean conduction path is, the tortuosity factor is used and oftentimes assessed by the Bruggeman relation that links the tortuosity solely to the porosity.[62] The tortuosity factor is an important characteristic in conventional electrodes, but both the parameter itself and its relation to the porosity are controversially discussed.[64–66]

For ASSBs, the flux-simulation elucidates that the non-wetting behavior of the solid electrolyte aggravates tortuosity issues and that the Bruggeman relation is not suitable in these systems. The importance of void reduction is fortified further and even small binder fractions can be crucial for the ion conduction paths. Minnmann et al. [20] later measured the effective partial conductivity of NCM622/lithium phosphorus sulfur chloride, Li_6PS_5Cl (LPSCl)-composites in ion- or electron-blocking symmetrical cells with different compositions and calculated slightly higher tortuosity factors than the model predicts. A possible explanation is the particle distribution: Reducing the LPSCl-particle size by grinding, Minnmann et al. [20] observe higher effective ionic and lower effective electronic conductivities. The smaller LPSCl-particles are distributed more homogeneously in the composite which resembles more the randomized particle placement in the model microstructures. Another explanation for the discrepancy are grain boundary effects: Albeit, the model accounts for contact resistances at the CAM/SE-interface, it neglects the grain boundary resistance among SE particles which is known to impede the effective ionic conduction.[102,103]

Considering the current densities in the context of future mobility, the work reveals that a bulk conductivity of solid electrolytes above 10 mS cm^{-1} should be targeted to break even with LIBs.

I created the study concept under the supervision of D. Weber. The modeling and simulation

was done by me using GeoDict[104] (Version 2019, Service Pack 2). The Math2Market-Team supported me with a script to accurately meet the binder content. The batch processing was realized by the Matlab-interface GeoLab and Matlab.[44] All authors contributed to editing the article that was written by me.

Reprinted with permission from Bielefeld, A.; Weber, D. A.; Janek, J. Modeling Effective Ionic Conductivity and Binder Influence in Composite Cathodes for All-Solid-State Batteries. *ACS Appl. Mater. Interfaces* **2020**, *12*, 12821–12833, DOI: 10.1021/acsami.9b22788
Copyright © 2020 American Chemical Society

ACS APPLIED MATERIALS & INTERFACES

www.acsami.org Research Article

Modeling Effective Ionic Conductivity and Binder Influence in Composite Cathodes for All-Solid-State Batteries

Anja Bielefeld,* Dominik A. Weber, and Jürgen Janek*

Cite This: ACS Appl. Mater. Interfaces 2020, 12, 12821−12833 Read Online

ACCESS | Metrics & More | Article Recommendations | Supporting Information

ABSTRACT: In the pursuit for future mobility, solid-state batteries open a wide field of promising battery concepts with a variety of advantages, ranging from energy density to power capability. However, trade-offs need to be addressed, especially for large-scale, cost-effective processing, which implies the use of a polymeric binder in the composite electrodes. Here, we investigate three-dimensional microstructure models of the active material, solid electrolyte, and binder to link cathode design and binder content with electrode performance. Focusing on lithium-ion transport, we evaluate the effective ionic conductivity and tortuosity in a flux-based simulation. Therein, we address the influence of electrode composition and active material particle size as well as the process-controlled design parameters of the void space and binder content. Even though added in small amounts, the latter has a strong negative influence on the ion transport paths and the active surface area. The simulation of ion transport within four-phase composites is supplemented by an estimation of the limiting current densities, illustrating that application-driven cell design starts at the microstructure level.

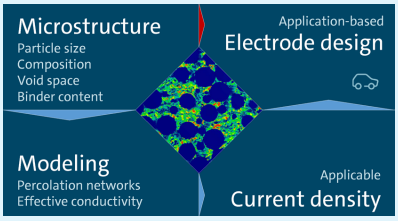

KEYWORDS: *all-solid-state batteries, cathode composite, percolation, NCM materials, polymer binder*

1. INTRODUCTION

Paving the way toward e-mobility, high-energy battery cells, produced on a large-scale, are highly sought-after. While conventional Li-ion battery technology and its processing is well-established,[1] it is also about to hit its physicochemical limits,[2] and all-solid-state batteries (ASSBs) are widely treated as jack of all trades in battery technology. They offer the potential to outperform conventional technology in terms of energy density, charging, and power capability[3] at a wide thermal stability window,[4] but a major issue yet to be resolved is cost-effective upscaling.[5]

When enabling the lithium-metal anode, ASSBs hold promise to reach ambitious energy density targets, albeit a dense, thin, and dendrite-safe solid electrolyte (SE) separator layer remains yet to be realized.[6] Reconciliation with the aforementioned goals is what poses major challenges in ASSB research on various levels: on the material level, solid electrolytes are still driven toward higher conductivities[7] and wider electrochemical windows,[8] with adequate tuning of interfaces[9,10] and interphases[11] gaining importance as they strongly influence cell performance. The controversial discussion on space charge layers[12−14] goes along with degradation prevention by particle coatings on the cathode side[10,15−19] and the introduction of sacrificial layers on Li-metal anodes.[20] On the cell level, the electrode design, especially on the cathode side, can be crucial for cell performance and has to be designed according to the use case of the cell: particle morphologies, sizes, and their distributions as well as residual voids influence the percolation behavior, thereby affecting ionic and electronic conduction and the active surface area, available for Li insertion.[21−28] Furthermore, the volume change of cathode active material particles may lead to contact loss upon cycling[29,30] and therefore influences performance as well. When it comes to processing ASSB cells cost-efficiently, upscaling for industrial application[5] is crux of the matter. Accordingly, processing of materials and composites in a wet slurry-based fabrication comparable to state-of-the-art Li-ion technology would be favorable but requires the incorporation of a binder, which has a negative impact on cell performance.[15,25,31−34]

The role of a binder, apart from enabling a high-throughput roll-to-roll process, is to act as a buffer for mechanical strain, induced upon cycling by the volume change of active material particles and to prevent peel-off and brittleness of the electrodes.[31] While the volume change of $LiCoO_2$ (LCO) is limited to around 2 vol % expansion upon cell charging, $LiNi_xCo_yMn_zO_2$ (NCM) shrinks by up to 6 vol % when delithiated for nickel-rich NCM811 in particular.[30] Apart from the mechanical issue, solid electrolytes pose challenges for a

Received: December 17, 2019
Accepted: February 25, 2020
Published: February 25, 2020

Downloaded via VOLKSWAGEN AG on March 23, 2020 at 14:21:13 (UTC).
See https://pubs.acs.org/sharingguidelines for options on how to legitimately share published articles.

ACS Publications © 2020 American Chemical Society

https://dx.doi.org/10.1021/acsami.9b22788
ACS Appl. Mater. Interfaces 2020, 12, 12821−12833

suitable binder choice as well: thiophosphate solid electrolytes show high reactivity with polar solvents.[35,36] Therefore, the trade-off between solubility in a non-polar or less polar solvent and sufficient binding ability for compensation of volume changes has to be resolved.[25,31,35] Due to the solubility in less polar solvents, such as xylene or toluene, many studies focus on nitrile butadiene rubber (NBR)[15,25,35,37] or styrene butadiene rubber (SBR)[33] as a binder. In comparison, dry-processed binder-free electrodes outperform wet-processed electrodes[25] because most binders are ionic and electronic insulators that block the active surface area needed for Li insertion and impede ionic and electronic pathways through the composite. Furthermore, wettability, homogeneity, and processability, mainly depending on viscosity, have to be considered as well.[38] One approach to avoid the aforementioned issues and to maintain rate performance similar to dry-processed electrodes is minimizing the binder amount. Hippauf et al.[32] manufactured NCM955 and Li_6PS_5Cl (LPSCl) electrode sheets in a solvent-free process with down to a 0.1 wt % polytetrafluoroethylene (PTFE) binder, which is assumed to have a fibril morphology. Another approach is to remove the binder from the readily formed electrode by heat treatment as performed by Yamamoto et al.,[34] who used a volatile poly(propylene carbonate)-based binder (PPC) in NCM111 and β-Li_3PS_4 (LPS) composites. The binder undergoes thermal depolymerization by unzipping, evaporates at temperatures above 300 °C, and does not impede conduction afterward. Oh et al.[31] suggested the introduction of a lithium ion-conducting ionic liquid, Li(G3)TFSI (G3, triethylene glycol dimethyl ether; LiTFSI, lithium bis(trifluoromethanesulfonyl)imide), into NBR in NCM622 and NCM711 cathodes with the LPSCl electrolyte for sufficient ionic pathways and contact, achieving enhanced performance compared to pure NBR and enabling quite high cathode thicknesses of 200 μm.

In this work, we address processing and cell design issues for composite cathodes based on thiophosphate solid electrolytes and NCM active material from a modeling perspective. We shed light on effective ionic conductivity, the associated tortuosity of composite electrodes, and their dependence on cell design parameters, such as active material (AM) particle size and size distribution, composition, void space, and binder content. Based on the effective conductivity and a couple of basic assumptions, we estimate maximum current densities achievable with these cathodes, judging the impact that the microstructural electrode layout and its modifications can have in ASSBs.

2. METHODS

The starting point for this work was our recently published conduction cluster analysis and percolation study.[21] Therein, electronic and ionic percolation of computed two-component ASSB cathode microstructures was evaluated: particle arrangements consisting of AM and SE particles were generated in GeoDict[39] in a rectangular parallelepiped of voxels, where the voxel length is associated with the microstructure's resolution. In order to reconstruct realistic composites of NCM and thiophosphate SE, the AM was represented by spherical, non-overlapping secondary particles. The introduction of single-crystal NMC in the model microstructures would imply moving to more complex particle shapes. However, anisotropic ion transport in these particles would not have to be taken into account for the effective ionic conductivity as the ionic conductivity of the solid electrolyte is 4 orders of magnitude higher than in the NMC (see assumption 2 below). The morphology of the SE particles was emulated by convex polyhedra that were allowed to exhibit overlap to take account for the relatively low Young's modulus of ~25 GPa of thiophosphates,[40,41] which reflects the materials' good ductility.

Two basic assumptions were made to compute the conductive networks: (1) The SE is a single-ion conductor with negligible electronic conductivity. (2) The AM's ionic conductivity is 4 orders of magnitude smaller than its SE equivalent and can therefore be neglected. Interconnected neighboring particles were considered to form a conduction cluster, so ionic conduction clusters consisted of connected SE particles and electronic conduction clusters were formed by connected AM particles, while no carbon additives were introduced. The material fraction that belongs to the conduction cluster was then referred to as the utilization level. For the AM, the utilization level can be seen as an equivalent to the accessible electrode capacity because isolated AM particles cannot be addressed upon cycling. Combined with the active interface area between the conduction clusters, the utilization level provides a hint on electronic or ionic limitations in the microstructure properties, even though this network analysis does not contain information on diffusion lengths and the tortuosity of ionic or electronic pathways.

The model microstructures in our previous work can be associated with pressed lab cells, which are based on carbon-free and binder-free composites. In this work, we target at modeling electrodes manufactured in a casting process: we suppose that electronic conduction is not the limiting factor because conductive carbon will be introduced into ASSB electrodes on their way to commercialization. A recent analysis of solid-state systems by Randau et al.[42] indicates that many studies already do so, and our focus therefore lies on ionic conduction. Furthermore, we study the influence of the binder and go beyond the computation of utilization levels and active interface areas by calculating effective properties. However, the study on the active material size, the void space, and the electrode composition are not restricted to electrodes manufactured in a casting process.

2.1. Tortuosity. In cells with a liquid electrolyte, two properties are used to characterize ion diffusion within the liquid electrolyte in porous electrodes at a continuum level: porosity ε and tortuosity τ (or the tortuosity factor $\kappa = \tau^2$). The porosity ε is defined as the volume fraction available for the fluid or, correspondingly, as the volume fraction not filled with the solid matrix. Tortuosity τ accounts for the tortuous and curvy trajectory the dissolved ions have to follow passing through the porous volume. In homogenizing the complex microstructure, its effective diffusion coefficient $D_{\mathrm{eff}}^{\mathrm{ion}}$ is then given by

$$D_{\mathrm{eff}}^{\mathrm{ion}} = \frac{\varepsilon}{\tau^2} D_{\mathrm{bulk}}^{\mathrm{ion}} = \frac{\varepsilon}{\kappa} D_{\mathrm{bulk}}^{\mathrm{ion}} \tag{1}$$

where $D_{\mathrm{bulk}}^{\mathrm{ion}}$ represents the ion diffusion coefficient of the bulk material.

Even though there is no fluid involved in ASSBs and the prevailing transport mechanism is ionic migration rather than diffusion, it is common to transfer the description of fluids to ASSB electrodes. On the assumption that interactions between lithium ions and lattice vacancies in the SE can be neglected,[43] the Nernst−Einstein equation can be used to link the lithium diffusion coefficient $D_{\mathrm{bulk,\,SE}}^{\mathrm{ion}}$ and the ionic bulk conductivity of the SE $\sigma_{\mathrm{bulk,\,SE}}^{\mathrm{ion}}$

$$D_{\mathrm{bulk,SE}}^{\mathrm{ion}} = \frac{\sigma_{\mathrm{bulk,SE}}^{\mathrm{ion}} RT}{c_{\mathrm{bulk,SE}}^{\mathrm{ion}} F^2} \tag{2}$$

Ionic conduction in the (now) solid electrolyte is tortuous as well, and the effective conductivity $\sigma_{\mathrm{eff}}^{\mathrm{ion}}$ may differ significantly from the bulk conductivity:[44]

$$\sigma_{\mathrm{eff}}^{\mathrm{ion}} = \frac{\varepsilon_{\mathrm{SE}}}{\tau^2} \sigma_{\mathrm{bulk,SE}}^{\mathrm{ion}} \tag{3}$$

The gentle reader may keep in mind that the term porosity can be ambiguous for ASSB electrodes as it is also used for the volume fraction, which is not filled by any electrode component.[21,26,35] In the composite microstructures, we therefore distinguish between the void

https://dx.doi.org/10.1021/acsami.9b22788
ACS Appl. Mater. Interfaces 2020, 12, 12821−12833

space ϕ, the total volume fraction of the SE with respect to the entire electrode volume (including void space ϕ) ε_{SE}, and the SE volume fraction related to the solid electrode volume v_{SE}, which are correlated by $\varepsilon_{SE} = (1 - \phi)v_{SE}$.

Geometrically, tortuosity is defined as the shortest pathway Δl through the microstructure scaled by its length Δx[45]

$$\tau = \frac{\Delta l}{\Delta x} \tag{4}$$

However, this tortuosity only accounts for the shortest pathway and does not average with wider but longer pathways, which are also used by the fluid and have an influence on effective diffusion. The geometrical tortuosity therefore underestimates the tortuosity compared to experiment-based values or flux-based simulations.[45]

To determine the tortuosity of electrode samples practically, bulk and effective properties can be measured and compared according to eq 1,[27,44] or (for conventional cells) electrochemical impedance spectroscopy is used in a symmetric cell setup with an electrolyte salt that does not contain lithium and therefore inhibits lithium insertion to achieve information on the tortuosity.[46,47] Furthermore, 3D reconstruction of X-ray tomography data[48] or focused ion beam-scanning electron microscopy data (FIB-SEM)[49] may be used. To extract tortuosity from tomography data, either geometry-based or flux-based calculations are applied.[45] Because of the abovementioned issues with the geometry-based method, we simulate the effective ionic conductivity $\sigma_{\text{eff, ion}}$ in a flux-based approach and calculate the tortuosity according to eq 3 but for ionic conductivity.

We further want to point out that both systems, liquid and solid, hold complications that are not considered in this continuum description: in liquid systems, adsorption and space charge affect charge transport, while grain boundary diffusion is an additional issue in solid systems.

2.2. Flux-Based Calculation of Effective Conductivity. The calculation of the effective conductivity is a problem of a complex composite consisting of multiple phases with different conductivities. Hence, the effective conductivity σ_{eff} of a three-dimensional microstructure is a symmetrical second-order 3 × 3 tensor. Since conduction in ASSB cathodes is essentially taking place perpendicular to the current collector plane, which we define as the x_3 direction, it is sufficient to compute the diagonal term σ_{33} and its off-diagonal neighbors σ_{13}, σ_{23}, which indicate the tendency of ions to deviate in the x_1 and x_2 directions, during their predominant motion in the x_3 direction. The tensor then takes the form

$$\sigma_{\text{eff}} = \begin{pmatrix} \sigma_{11} & \sigma_{12} & \sigma_{13} \\ \sigma_{21} & \sigma_{22} & \sigma_{23} \\ \sigma_{31} & \sigma_{32} & \sigma_{33} \end{pmatrix} = \begin{pmatrix} - & - & \sigma_{13} \\ - & - & \sigma_{23} \\ - & - & \sigma_{33} \end{pmatrix} \tag{5}$$

The common approach in GeoDict[39] is to describe electrical conduction or charge transport in general, analogous to heat conduction, as the governing mathematical equations for these processes are of the same kind. Therefore, a solver for the stationary heat equation

$$\nabla\cdot(\beta\nabla T) = f \text{ in } \Omega \tag{6}$$

developed by Wiegmann and Zemitis[50] is used, with the local conductivity $\beta(\mathbf{x})$, the temperature T, and heat sources or sinks f in the model volume $\Omega = (0, l_1) \times (0, l_2) \times (0, l_3)$. Under the assumption that each voxel's properties are known and that the interfaces of two materials are defined by the voxel faces, the so-called EJ-heat solver uses harmonic averaging and introduces explicit jumps across material interfaces to solve for the effective conductivity tensor.[50]

For ionic conductivity, Ohm's law

$$\mathbf{j} = \sigma\mathbf{E} = -\sigma\nabla\varphi \tag{7}$$

links the current density $\mathbf{j}$ to the gradient of the electric potential φ and the ionic conductivity σ. The electric field is referred to as $\mathbf{E}$. In the stationary case, the continuity equation for charge

$$\frac{\partial\rho}{\partial t} + \nabla\cdot\mathbf{j} = 0 \tag{8}$$

with the charge density ρ becomes

$$\nabla\cdot\mathbf{j} = 0 \tag{9}$$

$$\nabla\cdot(-\sigma\nabla\varphi) = 0 \tag{10}$$

and therefore takes the form of a Poisson equation analogous to the stationary heat (eq 6), which can be solved by applying a potential difference on both sides of the microstructure as a boundary condition. Different from our percolation study,[21] an ionic conductivity is assigned to both components (see Table S1, Supporting Information), where the ionic conductivity of the AM (here NCM532, measured by Amin and Chiang[51]) is 4 orders of magnitude smaller than that for the SE. As the contact resistance between the two components, we take the value of 40 Ω cm^2 estimated by Braun et al.[52] from EIS and SEM data of Kato et al.[4]

Since the effective ionic conductivity is provided by the simulation, the ionic tortuosity factor has finally been calculated as

$$\tau^2 = \frac{\sigma_{\text{bulk,SE}}^{\text{ion}}}{\sigma_{\text{eff}}^{\text{ion}}}\varepsilon_{\text{SE}} \tag{11}$$

2.3. Incorporation of Binder. Concerning microstructure reconstruction based on FIB-SEM or X-ray tomography and modeling, the presence of a binder, as well as conductive carbon, poses challenges: while the size of AM and SE particles are on the micrometer scale, the size of binder molecules and conductive carbon particles are rather on the nanoscale,[53,54] requiring either a combination of imaging methods or appropriate resolution, thereby still ensuring a representative volume.[49] Moreover, the distinction of the solid phases in the images is non-trivial as sufficient contrast is required.[49] Therefore, there is a lack of knowledge on the distribution of the binder in battery electrodes. The morphology of the carbon-binder conductive (CBC) network is not well-known, strongly dependent on processing, and can have a significant influence on effective properties. Nanoporosity of the CBC network can amplify the effect of surface coverage by the binder and lead to a reduced active interface area.[48]

Moreover, binders can exhibit quite different characteristics, depending on the functionality they are tailored to, with wettability, mechanical stability, resistivity, density, and morphology[38] as factors that have not yet been accounted for in microstructural modeling. Our approach is to set up a model where the binder does not exhibit a specific morphology (such as, e.g., PTFE, which takes the shape of fibrils) on the microscale but preferably smears up voids between AM particles. Accordingly, the binder covers active interface area and may affect ionic transport throughout the cathode, as observed previously.[25]

We use the AM microstructures generated in our previous work[21] and add the binder according to the procedure in GeoDict,[39] which targets the shape of a concave meniscus in locations where surfaces come close together. The process is explained and illustrated in the Supporting Information (Figures S1 and S2).

2.4. Estimation of Current Densities. When current is applied to an electrode, internal resistance will cause a voltage drop over the composite. To quantitatively judge the role of effective ionic conductivity and microstructure, we estimate the current density through a composite electrode and its associated C-rate that evolves from the electrode design, material-inherent parameters, and the voltage drop (also known as IR drop). The approach is schematically shown in Figure S3, Supporting Information. Similar to Kato et al.,[44] we assume that the potential drop originates from ionic conduction, while electronic transport is not limiting due to the presence of conductive carbon. Furthermore, we neglect all non-ohmic behaviors such as charge-transfer effects or ionic diffusion in the AM. Accordingly, the scalar current density j can be calculated by Ohm's law

https://dx.doi.org/10.1021/acsami.9b22788
ACS Appl. Mater. Interfaces 2020, 12, 12821−12833

ACS Applied Materials & Interfaces www.acsami.org Research Article

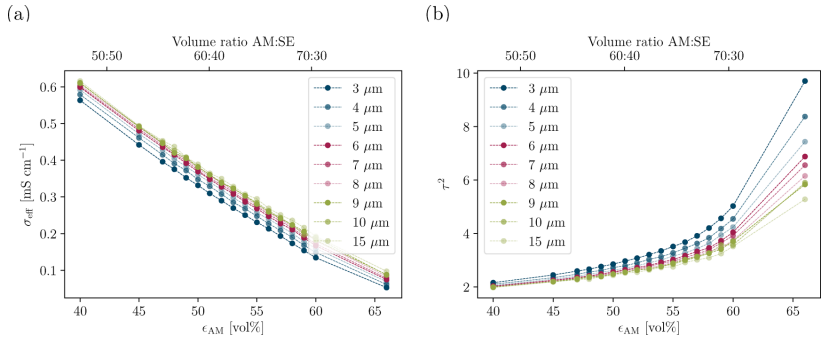

Figure 1. (a) Effective ionic conductivity and (b) ionic tortuosity factor of composite microstructures versus composition for uniformly distributed AM; particle sizes between $d \in [3,15]$ μm; electrode void space held constant at ϕ = 15%.

$$j^{ion} = \frac{I^{ion}}{A} = \frac{\Delta U}{R^{ion} A} \tag{12}$$

with the given voltage drop ΔU, the electrode surface area A, and the electrode resistance R^{ion} that, when expressed in terms of the specific resistance ρ_{eff}^{ion}, is dependent on the electrode thickness l

$$\rho_{eff}^{ion} = \frac{1}{\sigma_{eff}^{ion}} = R^{ion}\frac{A}{l} \tag{13}$$

Insertion of the effective ionic conductivity in eq 3 then allows us to estimate the current density as

$$j^{ion} = \sigma_{bulk,SE}^{ion}\frac{\varepsilon_{SE}}{\tau^2}\frac{\Delta U}{l} \tag{14}$$

$$j^{ion} = \sigma_{bulk,SE}^{ion}\frac{v_{SE}\cdot(1-\phi)}{\tau^2}\frac{\Delta U}{l} \tag{15}$$

The associated C-rate can then be calculated for a chosen AM with the specific capacity c_{AM}, density ρ_{AM}, and solid volume fraction v_{AM}.

$$C = \frac{j^{ion}}{c_{AM}\,\rho_{AM}\,v_{AM}(1-\phi)l} \tag{16}$$

$$C = \frac{\sigma_{bulk,SE}^{ion}}{c_{AM}\,\rho_{AM}}\frac{v_{SE}}{\tau^2 v_{AM}}\frac{\Delta U}{l^2} \tag{17}$$

Analog to the solid electrolyte volume fractions v_{SE} and ε_{SE}, the AM volume fraction referring to the solid volume is denoted as v_{AM} and related to the AM total volume fraction ε_{AM} by $\varepsilon_{AM} = v_{AM}(1-\phi)$.

3. RESULTS AND DISCUSSION

3.1. Effective Conduction. Sufficient effective ionic conductivity is essential for power capability and fast charging. We therefore study the ionic conduction properties for a variety of model microstructures. If not indicated otherwise, a void space of 15% in the particle arrangements is chosen. The data availability on the void space is sparse, but we are confident that our choice is a reasonable compromise for slurry-based electrodes, which are reported to possess 20−30% residual porosity in an uncalendered state,[55] as well as pressed electrodes with 13.2% residual porosity.[26] Infiltration of LPSCl into conventional LCO and graphite electrodes followed by cold-pressing is reported to decrease the void space to 6−8%.[35]

3.1.1. Comparison with the Literature. In order to validate that we are indeed capable of reproducing practically obtained effective properties with our microstructures, we reconstructed a LCO:$Li_{10}GeP_2S_{12}$ (LGPS):Acetylene Black cathode microstructure based on a cross-sectional SEM image from Kato et al.[44] Figure S4 (Supporting Information) shows the SEM image and a cross section of our reconstruction. Since LCO does not exhibit a spherical morphology like NCM, we modeled the AM as five-edged planar polyhedra and assumed Gaussian distributions for the particle thickness l_{AM} and ray length r_{AM}, which is defined as the distance from the polyhedron center to the outer face center. Unfortunately, no information on the void space in the pressed electrode is provided, and the SEM image does not allow us to distinguish between acetylene black and void space. As the residual void space is an important electrode characteristic, we assumed 15% for our model, similar to the measured void space from Hlushkou et al.[26] An overview of the model parameters is provided in Table S2, Supporting Information.

In the flux-based simulation, we get an effective ionic conductivity of 0.68 mS cm^{-1} with an associated ionic tortuosity factor of 2.29, while Kato et al.[44] report 0.73 mS cm^{-1} and 2.47, respectively. The reader should be aware that the calculation of the tortuosity factor is ambiguous because Kato et al.[44] do not account for the residual void space, which is undoubtedly not absent in a pressed electrode. The SE volume fraction ε_{SE} in eq 11 should not ignore the voids and therefore be calculated as $\varepsilon_{SE} = (1-\phi)v_{SE}$, which reduces the tortuosity value slightly. Still, the effective properties of the reconstructed microstructure are in good accordance with the experimental values and confirm the potential of the flux-based simulation approach.

3.1.2. AM Particle Size. To date, the impact of the AM particle size in ASSB composite electrodes is not intuitive: on the one hand, a previous work shows that the conduction networks are affected by AM particle size with small AM diameters leading to enhanced electronic percolation[23] and increased active surface area;[21] one the other hand, Froboese et al.[27] reported the tendency of high ionic tortuosity for small particles in their experimental model study on electrochemically inert glass particles in a composite with polymer SE, and Shi et al.[28] recommended a high AM/SE particle size ratio for enhanced ionic percolation properties. This indicates a possible trade-off between electronic and ionic conduction, connected with the choice of particle size for the AM. We therefore computed the effective ionic conductivity for uniform AM particle diameters between 3 and 15 μm as these are

https://dx.doi.org/10.1021/acsami.9b22788
ACS Appl. Mater. Interfaces 2020, 12, 12821−12833

typical sizes available for NCM secondary particles.[56,57] In order to avoid potential bias by the choice of the distribution settings, we chose to keep the parameter space smallest possible and to model uniform particle sizes. An extension to multimodal size distributions follows thereinafter. Figure 1a shows that the effective ionic conductivity does not only strongly depend on the electrode composition but is also influenced by AM particle size: an increasing AM fraction, which is needed for high energy application, linearly reduces the effective ionic conductivity for all particle sizes. Beyond that, smaller AM particles lead to reduced effective conductivity as well. This behavior can also be observed in the ionic tortuosity factor in Figure 1b, which starts at $\tau^2 \simeq 2$ for an AM to SE volume ratio of 50:50 and rises monotonously at a close-to-linear slope until 65:35 AM:SE. In this region, the tortuosity factors are in the range of $\tau^2 \in [2,5]$ and therefore similar to those observed in conventional NCM cathodes.[46,47,58] Above a volume ratio of 65:35 AM:SE, the ionic tortuosity rises abruptly, especially for small particle sizes. This tendency is also reported by Froboese et al.,[27] who explained that small AM particles lead to a higher total amount of particles in the structure that act as obstacles for bypassing ions. In a joint model and experimental study on NMC:LPS composites, Shi et al.[28] showed that increasing the AM/SE particle size ratio is favorable for ionic percolation networks and becomes particularly important for high AM loading, where ionic percolation is critical. Our results are in accordance as we model the SE at a fixed particle size of 3 μm and find enhanced ionic conductivity for increased AM particle size, which is equivalent with a high AM/SE particle size ratio. In general, pore size scales with particle size,[59] which means that smaller AM particles may offer more ionic pathways. One the other hand, these pathways are narrow and do not allow for ionic currents as high as with the wider pathways in composites with coarse particles.

3.1.3. Comparison with the Bruggeman Relation. The Bruggeman relation is commonly used to calculate the tortuosity factor for battery electrodes or to compare it to measured values. Therefore, it is worthwhile to judge its applicability to our model system. The Bruggeman relation itself is a mathematically derived equation for a porous medium of spherical particles in an ideal homogeneous distribution,[60] describing the ionic tortuosity factor solely with regard to the porosity

$$\tau^2(\varepsilon) = \varepsilon^{-1/2} \tag{18}$$

Due to the constraints in the underlying assumptions, a wide variety of modifications has been applied to the Bruggeman equation for more complex structures.[61] In the context of battery electrodes, an additional factor γ and the use of the exponent α as a fit parameter are common,[27,45,47,62] resulting in the modified Bruggeman equation

$$\tau^2(\varepsilon) = \gamma\varepsilon^{-\alpha} \tag{19}$$

Naturally, the modified Bruggeman eq 19 describes data more accurately than eq 18 because it incorporates two additional degrees of freedom within the fit parameters α and γ. For $\alpha = 0.5$ and $\gamma = 1$, the modified equation reduces to the original Bruggeman equation.

To compare the flux-based computed tortuosity factors of this work with the Bruggeman equation(s), we chose to take a closer look at the minimal and maximal particle size since the tortuosity factors of all other AM particle sizes lie in between. Figure 2 shows the ionic tortuosity factor's dependence on the

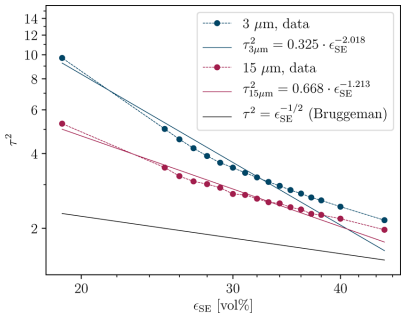

Figure 2. Simulated ionic tortuosity factor and comparison with the Bruggeman eq 18 and the modified Bruggeman eq 19 for composite microstructures versus total fraction of SE; uniformly distributed AM at particle size $d = \{3,15\}$ μm; electrode void space held constant at $\phi = 15\%$.

total fraction of SE $\varepsilon_{SE} = (1 - \phi) \cdot \nu_{SE}$ in context with the Bruggeman eq 18 and the modified/fitted Bruggeman eq 19. Clearly and similar to studies on conventional battery electrodes,[47,49] the Bruggeman equation significantly underestimates the tortuosity factor and does not adequately describe the complexity of electrode microstructures. The mismatch is pronounced especially for small AM particles and small SE fractions, where the values of the model microstructures are 4-fold larger than the Bruggeman eq 18 predicts. The modified Bruggeman eq 19 describes the behavior acceptably but incorporates parameters of $\alpha \in [2.02,1.21]$ and $\gamma \in [0.32,0.67]$, which are far off from 0.5 and 1, but similar to the ones found by Froboese et al.[27] In our opinion, these parameters do not offer any further scientific insight. In contrast to conventional electrodes, further characteristics like the morphology, particle size and distribution of the SE particles in ASSB electrodes can affect ionic tortuosity. These properties are not taken into account in the Bruggeman equation(s), making it even less applicable for ASSB cathodes than for conventional cathodes.

3.1.4. Multimodal AM Particle Size Distributions. The idea of multimodal size distributions is to improve densification since the limit for dense packing of equally sized spheres at 74%[63] does not apply. In particular, both the hexagonal and the cubic close packing of equally sized spheres r_L contain octahedral and tetrahedral voids, which can be filled with medium-sized spheres of radius $r_M = (\sqrt{2} - 1)r_L$ and small spheres with $r_S = \left(\sqrt{\frac{3}{2}} - 1\right)r_L$. For ideal packing with n large spheres (L) with radius r_L, $2n$ small spheres (S) with radius r_S are needed to fill the tetrahedral voids, and n medium spheres (M) with radius r_M are necessary to fill the octahedral voids.[64] We therefore focused on trimodal distributions with a number ratio of 1:1:2 for L:M:S and used the abovementioned ideal size distribution with $d_S = 2 \cdot r_S = 3$ μm as the lower limit for secondary NCM particles. Accordingly, the medium-sized particles were 5.5 μm in size, and the associated large particle size was 13.3 μm. The effect of the particle size was then studied by variation of the large particle size within

https://dx.doi.org/10.1021/acsami.9b22788
ACS Appl. Mater. Interfaces 2020, 12, 12821−12833

ACS Applied Materials & Interfaces www.acsami.org Research Article

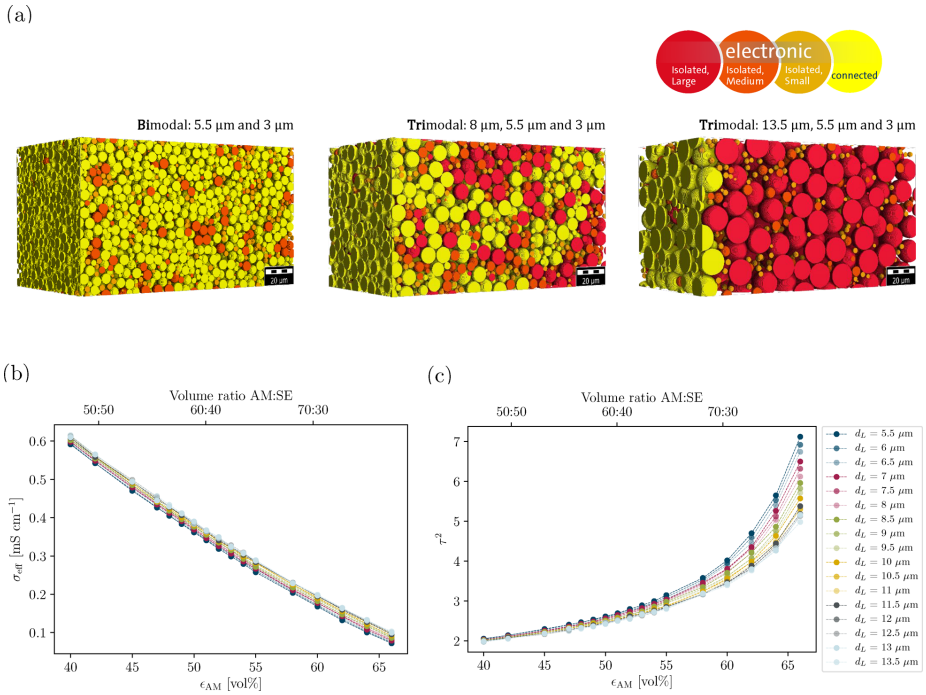

Figure 3. (a) Multimodal particle size distributions for AM with resulting electronic conduction clusters at 55 vol % AM fraction. (b) Effective ionic conductivity and (c) the ionic tortuosity factor of composite microstructures versus the fraction of the active material for trimodally distributed AM; particle sizes of the largest particles vary linearly between $d_L \in [5.5,13.5]$ μm; medium and small particle's size is held constant at $d_M = 5.5$ μm and $d_S = 3$ μm, while the electrode void space is held constant at $\phi = 15\%$.

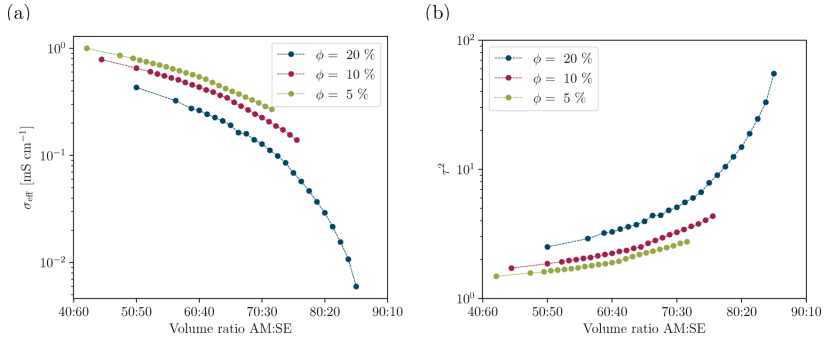

Figure 4. (a) Effective ionic conductivity and (b) ionic tortuosity factor of composite microstructures versus AM:SE volume ratio for uniformly distributed AM and their dependence on void space at an AM particle size of $d = 5$ μm.

$d_L \in [5.5,13.5]$ μm so that the distribution became bimodal in the lower limit of 5.5 μm, as illustrated in Figure 3a.

Figure 3b,c shows that also, in multimodal distributions, arrangements of smaller particles result in reduced effective ionic conduction and higher tortuosity for multimodal distributions. The effect of the particle size on tortuosity is observable in regions where ionic conduction becomes limiting and high energy density is achieved due to a large AM fraction. Compared to monomodal particle arrangements, the tortuosity is generally lower, even though the average particle size is smaller. We chose a specific composition (70:30 SE:AM volume ratio) to provide further insight into the discrepancies

https://dx.doi.org/10.1021/acsami.9b22788
ACS Appl. Mater. Interfaces 2020, 12, 12821−12833

ACS Applied Materials & Interfaces www.acsami.org Research Article

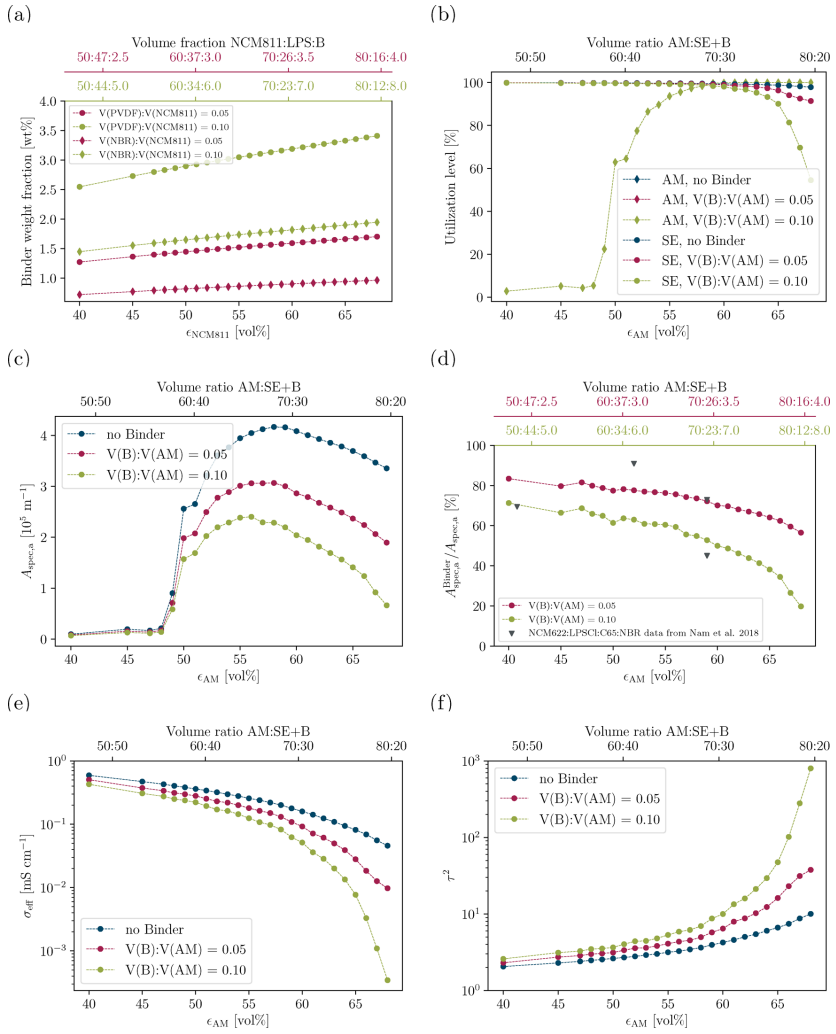

Figure 5. Influence of two different binder fractions on (a) binder weight fraction for PVDF and NBR in NCM811:LPS composites, (b) utilization level of the AM and SE, (c) active interface area between conductive clusters, (d) relative active interface area (normalized to values of binder-free electrodes), blue points represent data from GITT experiments on NCM622:LPSCl:C65:NBR, reported by Nam et al.,[25] (e) effective ionic conductivities and (f) ionic tortuosity factors in composite microstructures versus AM:SE+B (Binder) volume ratio. For the simulation, the AM particle size is d = 5 μm, and the electrode void space is constant at ϕ = 15%.

between mono- and multimodal distributions and their AM particle size dependence. The tortuosity factor versus the AM particle size for this composition is shown in Figure S5, Supporting Information. The linear behavior in the log−log plot to the right suggests that power law functions $\tau^2(d) = a \cdot d^{-b}$, with the fit parameters a and b can be used to acquire reasonable fits with the data sets. The fits indicate that the upper limit of the tortuosity factor, which would be reached for vanishing AM particle size, is at a tortuosity factor of $\lim_{d\to 0\mu m} \{\tau_{mono}^2(d)\} = 6.40$ for a monomodal AM particle distribution and $\lim_{d\to 0\mu m} \{\tau_{tri}^2(d)\} = 5.55$ for the chosen group of trimodal distributions at 15% void space and 70:30 AM:SE volume fraction. We conclude that, in comparison to monomodal AM particles, the trimodal particle size distribution reduces ionic tortuosity in this case.

https://dx.doi.org/10.1021/acsami.9b22788
ACS Appl. Mater. Interfaces 2020, 12, 12821−12833

Targeting an ionic tortuosity factor of 3.5, both distributions, mono- and multimodal, require an AM particle size of 12 μm.

3.1.5. Electrode Void Space. Even when fabricated thoroughly, ASSB electrodes exhibit void space that, in contrast to conventional electrodes, cannot be easily penetrated by the (solid) electrolyte. This additional characteristic is rarely thought of, even though there is evidence that it has a strong effect on the conduction properties:[21,26] utilizing FIB/SEM reconstruction of a pressed composite cathode of $LiNbO_3$-coated LCO and amorphous Li_2S-P_2S_5-LiI, Hlushkou et al.[26] found 13.2% of void space coupled with an ionic tortuosity factor of 1.6 and 1.74 by electrochemical impedance spectroscopy (EIS) and simulation in a random-walk particle-tracking technique, respectively. To impart an impression on the impact of void space, they compared the reconstructed microstructure to a fictitious electrode, in which all voids were filled with SE, and found a significantly reduced tortuosity factor of 1.27 in the simulation.

Figure 4 displays the effective ionic conductivity and tortuosity factor versus the AM:SE volume ratio for void spaces between 5 and 20% with 5 μm-sized AM particles. Volume ratios with an AM content above 73:27 AM:SE are challenging to obtain in microstructures of 5% void space because the limit of dense packing of spheres applies to the AM volume fraction in the entire volume, not to the fraction related to the solid volume v_{AM}. As observed before, the effective ionic conductivity decreases upon introduction of higher AM fractions for all void spaces. Furthermore, it is evident that a higher void space significantly lowers the ionic conductivity, with 2-fold higher effective conductivities for 5% void space, compared to 20%. This originates in the loss of ionic pathways in the cathode when more voids are present. Toward higher AM loading, the effective ionic conductivity drops, and the tortuosity factor steeply increases. Since the crucial effect of void space on electronic and ionic conduction clusters and the specific surface area between the two clusters has been reported,[21] we like to emphasize that void space is indeed an important and inherent electrode property that should not be neglected.

3.2. Binder. Studies of conventional battery electrodes used EIS[47] or tomography data and simulation[48] to show that binders can significantly change effective conduction properties. However, since the binder morphology is usually not properly resolved in tomography data,[49] it is challenging to quantify and to understand the effects. To provide insight into the impact of the binder in ASSB cathodes, we conducted a binder study evaluating the active surface area between the SE and AM, the effective ionic conductivity, and the associated ionic tortuosity factor. The volumetric binder fraction was hereby linked to the fraction of the AM in the electrode and is denoted by $V(B) : V(AM)$, which implies that the binder content in wt % is not constant with changing composition but increases slightly with AM content. As binder materials exhibit quite different gravimetric densities, we calculated the associated binder weight fractions for polyvinylidene difluoride (PVDF) (ρ_{PVDF} = 1.78 g cm^{-3}[65]) and NBR (ρ_{NBR} = 1 g cm^{-3}[66]) exemplarily and display them in Figure 5a: the fact that $V(NBR) : V(AM) = 0.1$ equals weight fractions lower than 2 wt % for NBR already indicates that even small binder weight fractions consume a significant volume and can therefore critically influence cell performance.

3.2.1. Percolation Study. Analogous to our previous work,[21] we identified ionic and electronic conduction networks in the model microstructures. The fraction of the AM or SE in the conductive network, the so-called utilization level, is shown for varying AM:SE volume ratio in Figure 5b. Owing to the mechanism of binder generation that was used on an existing AM microstructure, the utilization level of the AM is not affected by the presence of the binder, but there is a significant effect on the SE utilization for compositions with AM content larger than the 70:30 AM:SE volume ratio. We observed ionic limitation for binder-free microstructures in our previous study as well, in particular when voids occupy more space in the electrode.[21] The incorporation of binder impairs this effect: the binder impedes and blocks ionic pathways in the microstructure; hence, not all SE particles contribute to ionic conduction.

This can also be observed in the specific active surface area $A_{spec,\,a}$ in Figure 5c, which is reduced for both binder contents and decreases for compositions with more than 65 vol % AM. Figure 5d shows the same data, normalized to the specific active surface area of binder-free microstructures. The available interface for lithium insertion is reduced by at least 17% for the smaller binder content and 29% for the larger binder content in the case of low AM fractions. For high AM fractions, the reduction even amounts to 43 and 82%, respectively. The effect on the cell performance can thus be crucial. In a study on NCM622:LPSCl:C65:NBR composites, Nam et al.[25] obtained a lower capacity and rate capability for slurry-processed electrodes than binder-free dry-mixed electrodes. To gain insight on the AM/SE contact area, Nam et al.[25] performed galvanostatic intermittent titration technique (GITT) measurements on half-cells and correlated the contact area to N_2 adsorption−desorption isotherm experiments on NCM622 powders. In their study, the binder content in the slurry-mixed electrodes was held constant at 1.4 wt % for all compositions, corresponding to around 10 vol % NBR:NCM622 in the model microstructures. The experimental data on the AM/SE surface area is incorporated in Figure 5d, and it is obvious that for the small (70 wt % ≃ 48 vol %) and the large AM fraction (85 wt % ≃ 69 vol %), the data and model match quite well. The intermediate AM:SE composition exhibits better contact than predicted by our model, a fact that Nam et al.[25] do not comment on either. We are aware that a direct comparison is difficult because not all microstructure-determining properties of the composites are known: the void space may have a significant influence on the active surface area and is possibly inherently different between the experiment and simulation and between the dry- and wet-processed electrodes. Moreover, the AM and SE particle sizes and distributions are unknown, and only the AM particle size can be estimated from field-emission scanning electron microscopy surface images[25] to be around 5 μm. Another aspect is the presence of C65, a carbon additive that naturally provides a high surface area due to its small particle size. Therefore, it blocks parts of the AM surface and can reduce the overall interface area between SE and AM. Finally, experimental results obtained by GITT measurements have shown to be subject to large errors.[67]

3.2.2. Effective Conduction. Beyond that, the influence of the binder is also predominant in the effective ionic conductivity and the ionic tortuosity factor, as shown in Figure 5e,f. While the binder impedes the effective ionic conduction for all compositions, it becomes especially crucial in high-energy cells with more AM than in the volume ratio of 70:30 AM:SE+B. In these cases, the conductivity drops abruptly, and the ionic tortuosity increases steeply, indicating

https://dx.doi.org/10.1021/acsami.9b22788
ACS Appl. Mater. Interfaces 2020, 12, 12821−12833

ACS Applied Materials & Interfaces www.acsami.org Research Article

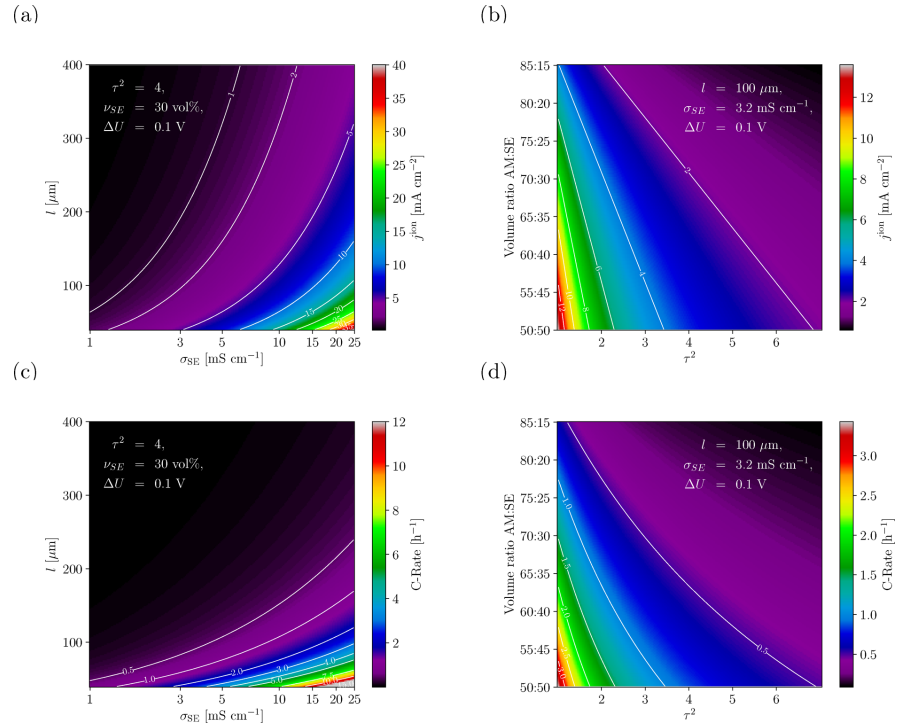

Figure 6. Estimated current densities depending on (a) electrode thickness and SE ionic bulk conductivity and (b) AM:SE composition and ionic tortuosity factor. Resulting C-rates for NCM811 for varying (c) electrode thickness and SE ionic bulk conductivity and (d) AM:SE composition and ionic tortuosity factor, assuming NCM811 and 15% void space.

that ionic transport becomes critical. We like to highlight that, although this effect is enhanced for the higher binder content, it is in general also observable for the small binder content. We expect that this tendency will hold for even higher binder amounts and lead to impaired properties in these cases.

3.3. Applicable Current Densities. As we gained a better understanding of the different aspects that can influence or impede ionic conduction, the next step is to link these insights to ASSB application and to discuss the influence of the microstructure on performance. The approach of estimating the practical current density in different cathode microstructures is basic and relies exclusively on ionic, ohmic losses.

We calculated the current density according to eq 15 and show its dependence on electrode thickness, SE bulk conductivity, AM:SE composition, and ionic tortuosity in Figure 6a,b. As before, a void space of 15% is assumed, and we used NCM811 with a specific capacity of 196 mA h g^{-1} and a gravimetric density of 4.76 g cm^{-3} to compute the associated C-rates from eq 17 and display them in Figure 6c,d. We restricted the allowed voltage drop ΔU to 0.1 V as the focus was not on high current pulses, where increased overpotential is commonly accepted, but on a stable and healthy usage. Of course, the current is linearly dependent on the voltage drop (eq 15), and higher current values can be calculated when higher voltage drops are tolerated. However, one should also keep in mind that the ionic, ohmic loss is not the only contribution: in the assessment of ASSB cathodes, charge transfer at the interfaces and Li diffusion within the AM are important aspects that may limit electrode performance as well. Consequently, our calculation should rather be considered a good case scenario because interface kinetics and AM diffusion limitation can become crucial for cell performance, even though the effective ionic conduction through the composite may be sufficient. Apart from that, the entire cell can be understood as a series of anode, separator, and cathode impedance.[52]

Figure 6a illustrates the effect of electrode thickness and ionic bulk conductivity on the estimated current density for an AM to SE volume fraction of 70:30 and an ionic tortuosity factor of 4, similar to conventional cathodes.[47] It indicates that common SEs, with conductivities below 5 mS cm^{-1}, are not necessarily enablers for thick electrode designs. Instead, highly conductive SE materials are needed for thick electrodes. Thus, when targeting a current density of 5 mA cm^{-2}, electrodes thinner than 70 μm are required for a SE with ionic bulk conductivity of 5 mS cm^{-1}. This effect is even more pronounced, when considering the C-rate in Figure 6c, which depends quadratically on the electrode thickness. In this case, an electrode thickness of 100 μm does not allow C-

https://dx.doi.org/10.1021/acsami.9b22788
ACS Appl. Mater. Interfaces 2020, 12, 12821−12833

rates above 2 C for SEs with an ionic conductivity below 17 mS cm^{-1}.

Figure 6b shows the influence of composition and ionic tortuosity on the applicable current density for LGPS as a common SE with 3.2 mS cm^{-1}[144] at 100 μm electrode thickness, suggesting two ways to compensate insufficient SE bulk conductivity when targeting a certain current density: the usage of higher SE fractions in the electrode or the tuning of the ionic tortuosity. While the first approach counteracts the high capacity, targeted by a thick electrode setup, we previously showed that the ionic tortuosity factor can be influenced by the AM particle size, electrode composition, void space, and binder content: actually, large SE fractions in the composite are likely to involve a reduction of ionic tortuosity (Figure 2) as the amount of AM obstacles in the ionic pathway decreases. The translation into C-rates in Figure 6d highlights that the tortuosity can indeed be a determining electrode characteristic for electrode design since, even for relatively high SE fractions in the composite (45 vol % SE), ionic tortuosity factors above 3 do not allow C-rates higher than 1 C. To analyze the influence of the binder, we have to reconsider Figure 5f: The tortuosity, τ^2, is likely to reach values of 10 for the higher content and 6.4 for the lower binder content, respectively, at a composition of 70 vol % AM and 15% void space. In a NMC811:LPS:NBR composite, this corresponds to 1.8 and 0.9 wt % NBR, respectively (Figure 5a). Compared to a tortuosity of 4.2 in the binder-free microstructure, this discrepancy illustrates that even small binder contents can adversely affect the tortuosity. For the electrode performance, this implies that the applicable current density for 1.8 wt % NBR is at 0.82 mA cm^{-2} (0.15 C), 0.9 wt % NBR suggests 1.3 mA cm^{-2} (0.23 C) and even the binder-free composite exhibits a current density below 2 mA cm^{-2} (0.35 C).

In order to assess what this means for ASSB application, we further estimated the current density for LGPS and the highly conductive $Li_{9.54}Si_{1.74}P_{1.44}S_{11.7}Cl_{0.3}$ (LSiPSCl) with 25 mS cm^{-1}[4] and distinguished between three use cases: an energy-driven electrode layout, a high-power cathode, and an intermediate setup. The specifications as well as the resulting current densities and C-rates can be found in Table 1. For the high-energy cathode, dense packing of AM particles is essential, so we assumed a thick electrode and a high AM fraction of 80 vol %, which leads to increased tortuosity factors around 10, depending on the particle size (Figures 1−3 and Figure S5), residual void space (Figure 4), and the binder content (Figure 5). The power-based electrode was thinner and featured a higher SE fraction. We referred to the Bruggeman equation to estimate its lower tortuosity limit. The intermediate cathode possesses a tortuosity of 4, as previously, and a medium thickness.

Table 1. Application Cases

parameter	symbol	unit	high energy	intermediate	high power
electrode thickness	l	[μm]	300	140	100
AM:SE volume fraction	v_{AM}/v_{SE}		80:20	70:30	60:40
ionic tortuosity factor	τ^2		10	4	1.7
current density, LGPS	j^{ion}_{LGPS}	[mA cm^{-2}]	0.18	1.46	7.25
current density, LSiPSCl	$j^{ion}_{LSiPSCl}$	[mA cm^{-2}]	1.42	11.4	56.7
C-rate, LGPS	C_{LGPS}	[h^{-1}]	0.010	0.19	1.5
C-rate, LSiPSCl	$C_{LSiPSCl}$	[h^{-1}]	0.074	1.46	11.9

The applicable current densities for LGPS are quite low for the high-energy and the intermediate case, with C-rates far below 0.2 C. Only the high-power setup would allow for 1.5 C, when a potential drop of 0.1 V is accepted. This highlights the strong influence of the cathode layout and its associated microstructure: a thick, tortuous electrode reaches its limit in ionic conductivity already at small current densities and is therefore inappropriate for fast (dis-)charging, revealing that the trade-off energy versus power density is not restricted to conventional Li-ion cells. Even though the current density in the high-power layout is clearly higher, the absolute value of 1.5 C is also not convincing and points out the importance of bulk ionic conductivity for the SE. In comparison to LGPS, the fast-ion conductor LSiPSCl enables enhanced current densities, albeit the high-energy layout is still ionically limited to currents below C/10. This stresses that, apart from material conductivity, microstructural tuning is essential for an energy-optimized electrode design. The choice of particle sizes, size distributions, and morphologies of the AM and SE should be considered as important as the SE material conductivities. Furthermore, we like to emphasize that processing is another key driver because it determines the residual void space, the binder content, and its distribution.

The case study and Figure 6a in particular suggest that lithium-ion conductivities of 10 mS cm^{-1} should be targeted in material design to achieve good performance at enhanced C-rates and reasonable energy density. In their electrochemical simulation of a garnet-based ASSB full cell, Finsterbusch et al.[43] find that an ionic SE conductivity of 2 mS cm^{-1} is sufficient to be on par with lithium-ion batteries containing a liquid electrolyte for a 50 μm-thick composite cathode at a rate of 1 C. However, for an increased electrode thickness of 100 μm, they observe transport limitations in the SE with 2 mS cm^{-1}, which significantly affect the discharge curves and the cell capacity. As these limitations do not occur for a SE conductivity of 11 mS cm^{-1}, we are confident that the evaluation is consistent with our model and the resulting estimate of current densities.

In liquid electrolytes, the ionic conductivity is in the range of 5 − 10 mS cm^{-1} (at room temperature) depending on the electrolyte system, the salt concentration, and the temperature.[68] However, liquid electrolytes are not single-ion conductors, and the migration current is carried by lithium ions and the corresponding salt anions (commonly PF_6^-). Therefore, the cationic transference number, used to describe the current fraction carried by the lithium ions, has to be considered. In the case of 1 M $LiPF_6$ at 20 °C, a typical transference number is 0.27,[68] implying a maximum partial lithium-ion conductivity of 2.7 mS cm^{-1}. So why does our assessment suggest that SEs require a higher ionic conductivity? The essential difference is that the SE does not easily wet the AM surface but introduces its own microstructure into the electrode with the void space and binder strongly affecting (and impeding) ionic pathways.

https://dx.doi.org/10.1021/acsami.9b22788
ACS Appl. Mater. Interfaces 2020, 12, 12821−12833

In any case, the production of high-performance ASSBs will require advanced processing on all levels of materials, electrodes, and cells.

4. CONCLUSIONS

For a fundamental understanding of the interdependencies between cathode design, processing, and performance, we set up a microstructural modeling procedure for ASSB cathodes, featuring the SE, AM, and binder. Focusing on the effective ionic conductivity and its associated ionic tortuosity, we studied the influence of the AM particle size and distribution, residual void space, and binder content. The calculation of the effective ionic conductivity was done in a flux-based approach on a 3D voxel microstructure. We eventually presented the trade-offs and showed that application-based design starts at the microstructure level.

The choice of the AM particle size can be seen as a trade-off between ionic and electronic conduction: while small AM particles have shown to offer a high surface area and good electronic percolation properties[21,23] as well as short lithium diffusion paths within the AM, in accordance to Froboese et al.,[27] we point out that they also impede ionic conduction and lead to tortuous pathways for mono- and multimodal size distributions. The electronic percolation issue could be solved by adding conductive carbon or by the usage of high AM fractions if degradation reactions at the SE/AM and the carbon/SE interfaces are prevented by coating.[10,17,19,29] To control the ionic tortuosity, while maintaining short diffusion paths within the AM, a sophisticated multimodal particle size distribution can be useful. Furthermore, experimentalists should consider moving on to a single-crystal AM instead of secondary particles as these offer different morphologies and small particle sizes,[57,69,70] connected with a smaller surface to bulk ratio, and therefore reduced area for decomposition between the AM and SE.

Since it is commonly used in the context of battery electrodes, we compared our results of ionic tortuosity to the Bruggeman relation for spherical particles and found that it is not valid for complex ASSB microstructures and significantly underestimates the tortuosity. Even though the modified Bruggeman relation could be fit to the data, we want to raise awareness that the Bruggeman equation(s) should be used cautiously.

The residual void space and the binder content are two processing-rooted properties, which critically influence ionic transport and the active surface area available for Li insertion. They are therefore essential for electrode performance, highlighting the importance of large-scale processing that either minimizes the binder amount[32,34] or incorporates an ion-conductive binder[31] and reduces void space.

Finally, we demonstrated that the current densities that can be realized in a composite cathode are strongly dependent on the microstructure and the electrode layout.

Generally, a model microstructure can only be understood as the snapshot of a real ASSB cathode because the latter are time-variant and influenced by mechanical and chemical effects during cycling[30] and aging. Accordingly, future work on the cathode microstructure should focus on elastic modeling and the effects of volume changes, as well as on a full electrochemical simulation, which has the potential to shed light on the impact of microstructure heterogeneities arising from processing or aging and to show how bottlenecks in ion transport develop.

ASSOCIATED CONTENT

Supporting Information

The Supporting Information is available free of charge at https://pubs.acs.org/doi/10.1021/acsami.9b22788.

Explanation and scheme of binder generation procedure; modeling parameters for flux-based simulation; scheme of elements for current density estimation; reconstruction of microstructure from Kato et al.:[44] SEM image comparison, overview of modeling parameters; and comparison of tortuosity dependence on the active material particle size for mono- and trimodal particle size distribution (PDF)

AUTHOR INFORMATION

Corresponding Authors

Anja Bielefeld − *Physikalisch-Chemisches Institut, Justus-Liebig-Universität, 35392 Giessen, Germany; Volkswagen AG, Group Innovation, 38436 Wolfsburg, Germany;* orcid.org/0000-0003-2193-8375; Email: anja.bielefeld@volkswagen.de

Jürgen Janek − *Physikalisch-Chemisches Institut and Center of Materials Research (LaMa), Justus-Liebig-Universität, 35392 Giessen, Germany;* orcid.org/0000-0002-9221-4756; Email: juergen.janek@phys.chemie.uni-giessen.de

Author

Dominik A. Weber − *Volkswagen AG, Group Innovation, 38436 Wolfsburg, Germany;* orcid.org/0000-0003-4357-9713

Complete contact information is available at: https://pubs.acs.org/10.1021/acsami.9b22788

Notes

The authors declare no competing financial interest.

ACKNOWLEDGMENTS

The authors thank Volkswagen AG for the financial support of this work. J.J. thanks the German Federal Ministry of Education and Research (BMBF) for funding within the Cluster of Competence "FESTBATT" (03XP0177A). The authors acknowledge helpful discussion with Philipp Minnmann (JLU) and thank the Math2Market-team for providing a smart script to accurately meet the binder content.

REFERENCES

(1) Hawley, W. B.; Li, J. Electrode Manufacturing for Lithium-Ion Batteries—Analysis of Current and Next Generation Processing. *J. Energy Storage* **2019**, *25*, 100862.

(2) Luntz, A. C.; Voss, J.; Reuter, K. Interfacial Challenges in Solid-State Li Ion Batteries. *J. Phys. Chem. Lett.* **2015**, *6*, 4599−4604.

(3) Zhu, G.-L.; Zhao, C.-Z.; Huang, J.-Q.; He, C.; Zhang, J.; Chen, S.; Xu, L.; Yuan, H.; Zhang, Q. Fast Charging Lithium Batteries: Recent Progress and Future Prospects. *Small* **2019**, *15*, 1805389.

(4) Kato, Y.; Hori, S.; Saito, T.; Suzuki, K.; Hirayama, M.; Mitsui, A.; Yonemura, M.; Iba, H.; Kanno, R. High-Power All-Solid-State Batteries using Sulfide Superionic Conductors. *Nat. Energy* **2016**, *1*, 16030.

(5) Schnell, J.; Günther, T.; Knoche, T.; Vieider, C.; Köhler, L.; Just, A.; Keller, M.; Passerini, S.; Reinhart, G. All-Solid-State Lithium-Ion and Lithium Metal Batteries − Paving the Way to Large-Scale Production. *J. Power Sources* **2018**, *382*, 160−175.

(6) Zhang, Z.; Shao, Y.; Lotsch, B.; Hu, Y.-S.; Li, H.; Janek, J.; Nazar, L. F.; Nan, C.-W.; Maier, J.; Armand, M.; Chen, L. New Horizons for Inorganic Solid State Ion Conductors. *Energy Environ. Sci.* **2018**, *11*, 1945−1976.

https://dx.doi.org/10.1021/acsami.9b22788
ACS Appl. Mater. Interfaces 2020, 12, 12821−12833

(7) Culver, S. P.; Koerver, R.; Krauskopf, T.; Zeier, W. G. Designing Ionic Conductors: The Interplay between Structural Phenomena and Interfaces in Thiophosphate-Based Solid-State Batteries. *Chem. Mater.* **2018**, *30*, 4179−4192.
(8) Dewald, G. F.; Ohno, S.; Kraft, M. A.; Koerver, R.; Till, P.; Vargas-barbosa, N. M.; Janek, J.; Zeier, W. G. Experimental Assessment of the Practical Oxidative Stability of Lithium Thiophosphate Solid Electrolytes. *Chem. Mater.* **2019**, 8328−8337.
(9) Krauskopf, T.; Hartmann, H.; Zeier, W. G.; Janek, J. Toward a Fundamental Understanding of the Lithium Metal Anode in Solid-State Batteries—An Electrochemo-Mechanical Study on the Garnet-Type Solid Electrolyte $Li_{6.25}Al_{0.25}La_3Zr_2O_{12}$. *ACS Appl. Mater. Interfaces* **2019**, *11*, 14463−14477.
(10) Wang, C.; et al. Manipulating Interfacial Nanostructure to Achieve High-Performance All-Solid-State Lithium-Ion Batteries. *Small Methods* **2019**, *3*, 1900261.
(11) Dietrich, C.; Koerver, R.; Gaultois, M. W.; Kieslich, G.; Cibin, G.; Janek, J.; Zeier, W. G. Spectroscopic Characterization of Lithium Thiophosphates by XPS and XAS − A Model to Help Monitor Interfacial Reactions in All-Solid-State Batteries. *Phys. Chem. Chem. Phys.* **2018**, *20*, 20088−20095.
(12) de Klerk, N. J. J.; Wagemaker, M. Space-Charge Layers in All-Solid-State Batteries; Important or Negligible? *ACS Appl. Energy Mater.* **2018**, *1*, 5609−5618.
(13) Yamamoto, K.; Iriyama, Y.; Asaka, T.; Hirayama, T.; Fujita, H.; Fisher, C. A. J.; Nonaka, K.; Sugita, Y.; Ogumi, Z. Dynamic Visualization of the Electric Potential in an All−Solid−State Rechargeable Lithium Battery. *Angew. Chem., Int. Ed.* **2010**, *49*, 4414−4417.
(14) Haruyama, J.; Sodeyama, K.; Han, L.; Takada, K.; Tateyama, Y. Space−Charge Layer Effect at Interface between Oxide Cathode and Sulfide Electrolyte in All-Solid-State Lithium-Ion Battery. *Chem. Mater.* **2014**, *26*, 4248−4255.
(15) Ito, S.; Fujiki, S.; Yamada, T.; Aihara, Y.; Park, Y.; Kim, T. Y.; Baek, S.-W.; Lee, J.-M.; Doo, S.; Machida, N. A Rocking Chair Type All-Solid-State Lithium Ion Battery Adopting Li_2O−ZrO_2 Coated $LiNi_{0.8}Co_{0.15}Al_{0.05}O_2$ and a Sulfide Based Electrolyte. *J. Power Sources* **2014**, *248*, 943−950.
(16) Xiao, Y.; Miara, L. J.; Wang, Y.; Ceder, G. Computational Screening of Cathode Coatings for Solid-State Batteries. *Joule* **2019**, *3*, 1252−1275.
(17) Culver, S. P.; Koerver, R.; Zeier, W. G.; Janek, J. On the Functionality of Coatings for Cathode Active Materials in Thiophosphate-Based All-Solid-State Batteries. *Adv. Energy Mater.* **2019**, *9*, 1900626.
(18) Nakamura, T.; Amezawa, K.; Kulisch, J.; Zeier, W. G.; Janek, J. Guidelines for All-Solid-State Battery Design and Electrode Buffer Layers Based on Chemical Potential Profile Calculation. *ACS Appl. Mater. Interfaces* **2019**, *11*, 19968−19976.
(19) Li, X.; et al. Unravelling the Chemistry and Microstructure Evolution of a Cathodic Interface in Sulfide-Based All-Solid-State Li-Ion Batteries. *ACS Energy Lett.* **2019**, *4*, 2480−2488.
(20) Keller, M.; Varzi, A.; Passerini, S. Hybrid Electrolytes for Lithium Metal Batteries. *J. Power Sources* **2018**, *392*, 206−225.
(21) Bielefeld, A.; Weber, D. A.; Janek, J. Microstructural Modeling of Composite Cathodes for All-Solid-State Batteries. *J. Phys. Chem. C* **2019**, *123*, 1626−1634.
(22) Park, J.; Kim, D.; Appiah, W. A.; Song, J.; Bae, K. T.; Lee, K. T.; Oh, J.; Kim, J. Y.; Lee, Y.-G.; Ryou, M.-H.; Lee, Y. M. Electrode Design Methodology for All-Solid-State Batteries: 3D Structural Analysis and Performance Prediction. *Energy Storage Mater.* **2019**, *19*, 124−129.
(23) Strauss, F.; Bartsch, T.; de Biasi, L.; Kim, A.-Y.; Janek, J.; Hartmann, P.; Brezesinski, T. Impact of Cathode Material Particle Size on the Capacity of Bulk-Type All-Solid-State Batteries. *ACS Energy Lett.* **2018**, *3*, 992−996.
(24) Siroma, Z.; Sato, T.; Takeuchi, T.; Nagai, R.; Ota, A.; Ioroi, T. AC Impedance Analysis of Ionic and Electronic Conductivities in Electrode Mixture Layers for an All-Solid-State Lithium-Ion Battery. *J. Power Sources* **2016**, *316*, 215−223.
(25) Nam, Y. J.; Oh, D. Y.; Jung, S. H.; Jung, Y. S. Toward Practical All-Solid-State Lithium-Ion Batteries with High Energy Density and Safety: Comparative Study for Electrodes Fabricated by Dry- and Slurry-Mixing Processes. *J. Power Sources* **2018**, *375*, 93−101.
(26) Hlushkou, D.; Reising, A. E.; Kaiser, N.; Spannenberger, S.; Schlabach, S.; Kato, Y.; Roling, B.; Tallarek, U. The Influence of Void Space on Ion Transport in a Composite Cathode for All-Solid-State Batteries. *J. Power Sources* **2018**, *396*, 363−370.
(27) Froboese, L.; van der Sichel, J. F.; Loellhoeffel, T.; Helmers, L.; Kwade, A. Effect of Microstructure on the Ionic Conductivity of an All Solid-State Battery Electrode. *J. Electrochem. Soc.* **2019**, *166*, A318−A328.
(28) Shi, T.; Tu, Q.; Tian, Y.; Xiao, Y.; Miara, L. J.; Kononova, O.; Ceder, G. High Active Material Loading in All-Solid-State Battery Electrode via Particle Size Optimization. *Adv. Energy Mater.* **2020**, *10*, 1902881.
(29) Koerver, R.; Aygün, I.; Leichtweiß, T.; Dietrich, C.; Zhang, W.; Binder, J. O.; Hartmann, P.; Zeier, W. G.; Janek, J. Capacity Fade in Solid-State Batteries: Interphase Formation and Chemomechanical Processes in Nickel-Rich Layered Oxide Cathodes and Lithium Thiophosphate Solid Electrolytes. *Chem. Mater.* **2017**, *29*, 5574−5582.
(30) Koerver, R.; Zhang, W.; de Biasi, L.; Schweidler, S.; Kondrakov, A. O.; Kolling, S.; Brezesinski, T.; Hartmann, P.; Zeier, W. G.; Janek, J. Chemo-Mechanical Expansion of Lithium Electrode Materials - On the Route to Mechanically Optimized All-Solid-State Batteries. *Energy Environ. Sci.* **2018**, *11*, 2142−2158.
(31) Oh, D. Y.; Nam, Y. J.; Park, K. H.; Jung, S. H.; Kim, K. T.; Ha, A. R.; Jung, Y. S. Slurry-Fabricable Li^+-Conductive Polymeric Binders for Practical All-Solid-State Lithium-Ion Batteries Enabled by Solvate Ionic Liquids. *Adv. Energy Mater.* **2019**, *9*, 1802927.
(32) Hippauf, F.; Schumm, B.; Doerfler, S.; Althues, H.; Fujiki, S.; Shiratsuchi, T.; Tsujimura, T.; Aihara, Y.; Kaskel, S. Overcoming Binder Limitations of Sheet-Type Solid-State Cathodes using a Solvent-Free Dry-Film Approach. *Energy Storage Mater.* **2019**, *21*, 390−398.
(33) Inada, T.; Takada, K.; Kajiyama, A.; Kouguchi, M.; Sasaki, H.; Kondo, S.; Watanabe, M.; Murayama, M.; Kanno, R. Fabrications and Properties of Composite Solid-State Electrolytes. *Solid State Ionics* **2003**, *158*, 275−280.
(34) Yamamoto, M.; Terauchi, Y.; Sakuda, A.; Takahashi, M. Binder-Free Sheet-Type All-Solid-State Batteries with Enhanced Rate Capabilities and High Energy Densities. *Sci. Rep.* **2018**, *8*, 1212.
(35) Kim, D. H.; Oh, D. Y.; Park, K. H.; Choi, Y. E.; Nam, Y. J.; Lee, H. A.; Lee, S.-M.; Jung, Y. S. Infiltration of Solution-Processable Solid Electrolytes into Conventional Li-Ion-Battery Electrodes for All-Solid-State Li-Ion Batteries. *Nano Lett.* **2017**, *17*, 3013−3020.
(36) Oh, D. Y.; Nam, Y. J.; Park, K. H.; Jung, S. H.; Cho, S.-J.; Kim, Y. K.; Lee, Y.-G.; Lee, S.-Y.; Jung, Y. S. Excellent Compatibility of Solvate Ionic Liquids with Sulfide Solid Electrolytes: Toward Favorable Ionic Contacts in Bulk-Type All-Solid-State Lithium-Ion Batteries. *Adv. Energy Mater.* **2015**, *5*, 1500865.
(37) Oh, D. Y.; Kim, D. H.; Jung, S. H.; Han, J.-G.; Choi, N.-S.; Jung, Y. S. Single-Step Wet-Chemical Fabrication of Sheet-Type Electrodes from Solid-Electrolyte Precursors for All-Solid-State Lithium-Ion Batteries. *J. Mater. Chem. A* **2017**, *5*, 20771−20779.
(38) Riphaus, N.; Strobl, P.; Stiaszny, B.; Zinkevich, T.; Yavuz, M.; Schnell, J.; Indris, S.; Gasteiger, H. A.; Sedlmaier, S. J. Slurry-Based Processing of Solid Electrolytes: A Comparative Binder Study. *J. Electrochem. Soc.* **2018**, *165*, A3993−A3999.
(39) Math2Market GmbH, K. G. *GeoDict — The Digital Material Laboratory*, Version 2019 SP 2. Math2Market GmbH, 2019.
(40) Sakuda, A.; Hayashi, A.; Tatsumisago, M. Sulfide Solid Electrolyte with Favorable Mechanical Property for All-Solid-State Lithium Battery. *Sci. Rep.* **2013**, *3*, 2261.

https://dx.doi.org/10.1021/acsami.9b22788
ACS Appl. Mater. Interfaces 2020, 12, 12821−12833

(41) Deng, Z.; Wang, Z.; Chu, I.-H.; Luo, J.; Ong, S. P. Elastic Properties of Alkali Superionic Conductor Electrolytes from First Principles Calculations. *J. Electrochem. Soc.* **2016**, *163*, A67−A74.
(42) Randau, S.; Weber, D. A.; Kötz, O.; Koerver, R.; Braun, P.; Weber, A.; Ivers-Tiffée, E.; Adermann, T.; Kulisch, J.; Zeier, W. G.; Richter, F. H.; Janek, J. Benchmarking the Performance of All-Solid-State Lithium Batteries. *Nature Energy* **2020**, DOI: 10.1038/s41560-020-0565-1.
(43) Finsterbusch, M.; Danner, T.; Tsai, C.-L.; Uhlenbruck, S.; Latz, A.; Guillon, O. High Capacity Garnet-Based All-Solid-State Lithium Batteries: Fabrication and 3D-Microstructure Resolved Modeling. *ACS Appl. Mater. Interfaces* **2018**, *10*, 22329−22339.
(44) Kato, Y.; Shiotani, S.; Morita, K.; Suzuki, K.; Hirayama, M.; Kanno, R. All-Solid-State Batteries with Thick Electrode Configurations. *J. Phys. Chem. Lett.* **2018**, *9*, 607−613.
(45) Tjaden, B.; Brett, D. J. L.; Shearing, P. R. Tortuosity in Electrochemical Devices: A Review of Calculation Approaches. *Int. Mater. Rev.* **2018**, *63*, 47−67.
(46) Landesfeind, J.; Ebner, M.; Eldiven, A.; Wood, V.; Gasteiger, H. A. Tortuosity of Battery Electrodes: Validation of Impedance-Derived Values and Critical Comparison with 3D Tomography. *J. Electrochem. Soc.* **2018**, *165*, A469−A476.
(47) Landesfeind, J.; Hattendorff, J.; Ehrl, A.; Wall, W. A.; Gasteiger, H. A. Tortuosity Determination of Battery Electrodes and Separators by Impedance Spectroscopy. *J. Electrochem. Soc.* **2016**, *163*, A1373−A1387.
(48) Trembacki, B. L.; Mistry, A. N.; Noble, D. R.; Ferraro, M. E.; Mukherjee, P. P.; Roberts, S. A. Editors' Choice—Mesoscale Analysis of Conductive Binder Domain Morphology in Lithium-Ion Battery Electrodes. *J. Electrochem. Soc.* **2018**, *165*, E725−E736.
(49) Almar, L.; Joos, J.; Weber, A.; Ivers-Tiffée, E. Microstructural Feature Analysis of Commercial Li-Ion Battery Cathodes by Focused Ion Beam Tomography. *J. Power Sources* **2019**, *427*, 1−14.
(50) Wiegmann, A.; Zemitis, A. *EJ-HEAT: A Fast Explicit Jump Harmonic Averaging Solver for the Effective Heat Conductivity of Composite Materials*. Report of the Fraunhofer ITWM 2006, *94*.
(51) Amin, R.; Chiang, Y.-M. Characterization of Electronic and Ionic Transport in $Li_{1-x}Ni_{0.33}Mn_{0.33}Co_{0.33}O_2$ (NMC_{333}) and $Li_{1-x}Ni_{0.50}Mn_{0.20}Co_{0.30}O_2$ (NMC_{523}) as a Function of Li Content. *J. Electrochem. Soc.* **2016**, *163*, A1512−A1517.
(52) Braun, P.; Uhlmann, C.; Weiss, M.; Weber, A.; Ivers-Tiffée, E. Assessment of All-Solid-State Lithium-Ion Batteries. *J. Power Sources* **2018**, *393*, 119−127.
(53) Zielke, L.; Hutzenlaub, T.; Wheeler, D. R.; Chao, C.-W.; Manke, I.; Hilger, A.; Paust, N.; Zengerle, R.; Thiele, S. Three-Phase Multiscale Modeling of a $LiCoO_2$ Cathode: Combining the Advantages of FIB−SEM Imaging and X-Ray Tomography. *Adv. Energy Mater.* **2015**, *5*, 1401612.
(54) Bauer, W.; Nötzel, D.; Wenzel, V.; Nirschl, H. Influence of Dry Mixing and Distribution of Conductive Additives in Cathodes for Lithium Ion Batteries. *J. Power Sources* **2015**, *288*, 359−367.
(55) Ates, T.; Keller, M.; Kulisch, J.; Adermann, T.; Passerini, S. Development of an All-Solid-State Lithium Battery by Slurry-Coating Procedures using a Sulfidic Electrolyte. *Energy Storage Mater.* **2019**, *17*, 204−210.
(56) Tsai, P.-C.; Wen, B.; Wolfman, M.; Choe, M.-J.; Pan, M. S.; Su, L.; Thornton, K.; Cabana, J.; Chiang, Y.-M. Single-Particle Measurements of Electrochemical Kinetics in NMC and NCA Cathodes for Li-Ion Batteries. *Energy Environ. Sci.* **2018**, *11*, 860−871.
(57) Li, J.; Li, H.; Stone, W.; Weber, R.; Hy, S.; Dahn, J. R. Synthesis of Single Crystal $LiNi_{0.5}Mn_{0.3}Co_{0.2}O_2$ for Lithium Ion Batteries. *J. Electrochem. Soc.* **2017**, *164*, A3529−A3537.
(58) Ebner, M.; Chung, D.-W.; García, R. E.; Wood, V. Tortuosity Anisotropy in Lithium-Ion Battery Electrodes. *Adv. Energy Mater.* **2014**, *4*, 1301278.
(59) Giesche, H. Mercury Porosimetry: A General (Practical) Overview. *Part. Part. Syst. Charact.* **2006**, *23*, 9−19.
(60) Bruggeman, D. A. G. Berechnung verschiedener physikalischer Konstanten von heterogenen Substanzen. I. Dielektrizitätskonstanten und Leitfähigkeiten der Mischkörper aus isotropen Substanzen. *Ann. Phys.* **1935**, *416*, 636−664.
(61) Shen, L.; Chen, Z. Critical Review of the Impact of Tortuosity on Diffusion. *Chem. Eng. Sci.* **2007**, *62*, 3748−3755.
(62) Thorat, I. V.; Stephenson, D. E.; Zacharias, N. A.; Zaghib, K.; Harb, J. N.; Wheeler, D. R. Quantifying Tortuosity in Porous Li-Ion Battery Materials. *J. Power Sources* **2009**, *188*, 592−600.
(63) László, F. T., Ed. Dichteste Kugelpackung. Eine Idee von Gauß. *Abhandlungen der Braunschweigischen Wissenschaftlichen Gesellschaft*; Goltze: Göttingen, 1977; Vol. 27.
(64) Müller, U. Anorganische Strukturchemie. 6th edn.; *Teubner Studienbücher Chemie*; Vieweg+Teubner Verlag: Wiesbaden, 2008.
(65) Sigma Aldrich, *Safety Data Sheet according to Regulation (EC) No. 1907/2006: Poly(vinylidene fluoride)*. 17.12.2018.
(66) Sigma Aldrich, *Safety Data Sheet according to Regulation (EC) No. 1907/2006: Poly(acrylonitrile-co-butadiene)*. 17.12.2018.
(67) Shen, Z.; Cao, L.; Rahn, C. D.; Wang, C.-Y. Least Squares Galvanostatic Intermittent Titration Technique (LS-GITT) for Accurate Solid Phase Diffusivity Measurement. *J. Electrochem. Soc.* **2013**, *160*, A1842−A1846.
(68) Landesfeind, J.; Gasteiger, H. A. Temperature and Concentration Dependence of the Ionic Transport Properties of Lithium-Ion Battery Electrolytes. *J. Electrochem. Soc.* **2019**, *166*, A3079−A3097.
(69) Li, J.; Cameron, A. R.; Li, H.; Glazier, S.; Xiong, D.; Chatzidakis, M.; Allen, J.; Botton, G. A.; Dahn, J. R. Comparison of Single Crystal and Polycrystalline $LiNi_{0.5}Mn_{0.3}Co_{0.2}O_2$ Positive Electrode Materials for High Voltage Li-Ion Cells. *J. Electrochem. Soc.* **2017**, *164*, A1534−A1544.
(70) Li, H.; Li, J.; Ma, X.; Dahn, J. R. Synthesis of Single Crystal $LiNi_{0.6}Mn_{0.2}Co_{0.2}O_2$ with Enhanced Electrochemical Performance for Lithium Ion Batteries. *J. Electrochem. Soc.* **2018**, *165*, A1038−A1045.

https://dx.doi.org/10.1021/acsami.9b22788
ACS Appl. Mater. Interfaces 2020, 12, 12821−12833

3.3. Electrochemical Simulation of the Charge Performance (Publication 3)

The first publications focus on conduction networks and pathways in ASSB composite cathodes and emphasize the important role that the non-wetting behavior of the SE and its particle morphology play. Their assumptions are quite general, the required computing power is manageable, but despite the low model complexity, they are capable to answer burning research questions. However, the works neglect aspects that are essential for the electrochemical cell, e.g. the (de-)intercalation of lithium at the SE/CAM-interface and the lithium kinetics inside the cathode host material.
The third publication features a mathematical model that is not as straightforward as its predecessors, but rather falls in the category of electrochemical charge/discharge simulations[26,38,86,87] (see figure 2.4). By means of a FEM-simulation, microstructural influences are studied at different levels: The reconstruction of a previously reported LPSCl/NCM811-cathode[23] is used to validate the model setup and to study the impact of seemingly small modifications in the CAM particle size distribution. The interdependence of simulation and experiment becomes evident with the closer look at the lithium diffusion coefficient $\tilde{D}_{\mathrm{Li}}$ in the NCM and the exchange current density j_0 at the LPSCl/NCM811-interface. By nature, the values of these input parameters depend on the degree of lithiation of the NCM, but in the simulations, they are commonly assumed to be constant. The study highlights the significance of properly measured input parameters and their impact on the simulation results, emphasizing the need of a reliable input parameter set.
As the previous studies have pointed out that voids in the composite can crucially influence the conduction networks, the third publication zooms in on the LPSCl/NCM811-interface under the presence of voids and analyzes the impact of the surface coverage, the void size and distribution. Smaller voids can be associated with residual porosity that results from manufacturing and larger voids, in the order of the SE particle size, with the contact loss due to volume change in the composite upon cycling.[19]
Finally, the work provides an outlook toward (laser-patterned) tortuosity-optimized cone microstructures and their required channel thickness for a sufficient CAM-SE-interface area.

D. Weber and me came up with the study idea; the model concept and assumptions were developed together with J. Janek. R. Ruess conducted the experiments for the validation and the model input parameters. I set up the mathematical and geometrical model(s) and implemented the charge simulation in Comsol 5.4[50] using the Batteries and Fuel Cells- and the CADImport-interfaces. I created the particle-type microstructures in GeoDict[104] (Version 2019, Service Pack 2) with the GrainGeo-module and imported them to Comsol via the Matlab[44]-interfaces GeoLab and Matlab-LiveLink. V. Glavas supervised the simulation. The article was written by me and reviewed by all authors.

Reprinted with permission from Bielefeld, A.; Weber, D. A.; Ruess, R.; Glavas, V.; Janek, J. Influence of Lithium Ion Kinetics, Particle Morphology and Voids on the Electrochemical Performance of Composite Cathodes for All-Solid-State Batteries. *J. Electrochem. Soc.* **2022**, *169*, 020539, DOI: 10.1149/1945-7111/ac50df

Copyright © The Electrochemical Society. Reproduced by permission of IOP Publishing Ltd. All rights reserved.

Journal of The Electrochemical Society, 2022 **169** 020539
1945-7111/2022/169(2)/020539/13/$40.00 © 2022 The Electrochemical Society ("ECS"). Published on behalf of ECS by IOP Publishing Limited

Influence of Lithium Ion Kinetics, Particle Morphology and Voids on the Electrochemical Performance of Composite Cathodes for All-Solid-State Batteries

Anja Bielefeld,[1,2,z] Dominik A. Weber,[3] Raffael Rueß,[1,2] Vedran Glavas,[3] and Jürgen Janek[1,2,z]

[1]*Physikalisch-Chemisches Institut, Justus-Liebig-Universität, 35392 Giessen, Germany*
[2]*Center of Materials Research (LaMa), Justus-Liebig-Universität, 35392 Giessen, Germany*
[3]*Volkswagen AG, 38440 Wolfsburg, Germany*

With the ongoing transformation to e-mobility, lithium all-solid-state batteries are promising candidates for advanced mobile energy storage. Other than in conventional lithium ion cells, the rigid solid electrolyte entails its own morphology and does not wet residual voids in composite electrodes, which can limit the cell performance. We therefore take a closer look at the influence of microstructural characteristics on different scales in composite cathodes by means of electrochemical simulation using the finite element method. Cathode active material particle arrangements are constructed to validate the model against experimental data. We highlight the significance of the active material particle size distribution and state-of-charge dependent input parameters, such as the lithium diffusion coefficient in NCM811 and the exchange current density at the interface of NCM811 and Li_6PS_5Cl. We zoom in on that interface under the presence of void space that can result from manufacturing or arise from inter-particle contact loss upon volume changes. In a 1-particle-void model, the impact of the active surface area covered by voids is studied as well as the influence of the void distribution and the void size on the electrochemical performance. Beyond that, we simulate a tortuosity-optimized structured electrode and provide first guidelines for laser-patterned all-solid-state cathodes.
© 2022 The Electrochemical Society ("ECS"). Published on behalf of ECS by IOP Publishing Limited. [DOI: 10.1149/1945-7111/ac50df]

Manuscript submitted December 2, 2021; revised manuscript received January 5, 2022. Published February 16, 2022.

Supplementary material for this article is available online

As e-mobility is evolving, the requirements on battery technology are getting tight as well. Lithium all-solid-state batteries (SSBs) are considered as promising candidates for automotive application, as they are potential enablers of lithium metal anodes that promote high energy densities.[1,2] Albeit highly conductive solid electrolytes (SEs) are known, e.g. the thiophosphates $Li_{5.5}PS_{4.5}Cl_{1.5}$ with 12 mS cm^{-1} ionic conductivity on sintering[3] and $Li_{9.54}Si_{1.74}P_{1.44}S_{11.7}Cl_{0.3}$ with 25 mS cm^{-1},[4] the performance of SSBs oftentimes undercuts those of conventional lithium ion batteries[5] due to insufficient electrode design,[6] such as composition, loading and density and high internal resistance,[7] arising amongst others from chemical and electrochemical reactions, poor contact and volume changes.

In the composite cathode, highly conductive SEs and conventional high-capacity cathode active materials (CAMs), such as polycrystalline $LiNi_xCo_yMn_zO_2$ (NCM), do not garantee a high-performance SSB. Instead, one faces chemo-mechanical issues linked to the volume changes that the CAM undergoes upon delithiation,[8,9] and Rueß et al.[10] and Trevisanello et al.[11] report that the cracking of polycrystalline NCM811 particles around 3.8 V offers new electrochemically active surface area for liquid electrolytes that seemingly improves the lithium diffusion coefficient in the NCM, while it actually shortens the diffusion paths. SSBs, however, cannot benefit from this phenomenon, because the SE cannot infiltrate into the pores built upon cracking. One idea to solve this issue in SSBs and to move to smaller particle sizes, is to rely on single-crystalline NCM instead.[12–14]

Another challenge in the cathode is the (electro-)chemical stability of the materials[15–18] that is to be overcome by different coating strategies.[19–22] However, material compatibility is not only a question of chemical degradation at interfaces and the formation of interphases, but also one of ionic and electronic conduction networks through the composite. The electrode design of SSB cathodes includes the choice of particle sizes and size distributions, particle morphologies, the composition, and microstructure-affecting manufacturing choices, such as the binder chemistry, its fraction and distribution as well as undesired voids that remain in the composite.[23–28]. A major trade-off between high energy density and fast charging capability in SSB cathodes has been identified: Superior energy density requires a high utilization degree of the CAM and an elevated CAM loading and therefore, favorable inter-particle connection is needed. That can either be achieved by a high CAM fraction in the composite[24,27] or by carbon additives. High CAM fractions naturally lower the fraction of SE and cause tortuous ion paths. And in terms of energy density, the SE is undesirable in the cathode, as it occupies volume that is not available for the chemically active CAM and high-density SEs, such as halides or oxides, contribute significantly to the cell weight. Meanwhile, elevated charge rates demand fast and short ion paths that involve a higher fraction of SE.[25,27,29,30].

The above trade-off is not entirely new in the field of battery cell design: In conventional lithium ion battery electrodes, optimization has developed toward (micro-)structured electrodes with various targets and different techniques: Chen et al.[31] created pore channels to be infiltrated by the liquid electrolyte in graphite electrodes to obtain laser-patterned microstructures that show improved fast charge performance at 4 and 6 C charge rates. Bolsinger et al.[32] did not structure the electrode in its entire thickness, but performed superficial laser ablation of NCM cathodes to open binder-blocked pores for the liquid electrolyte, while Bae et al.[33] and Chiang et al.[34] obtained pore channels in $LiCoO_2$ electrodes by co-extrusion and Wood et al.[35] and Billaud et al.[36] used magnetic fields to align graphite particles and reduce the tortuosity for the ion transport in the electrolyte.

Though the structuring techniques will have to be different in SSBs, microstructure tuning of SE composite electrodes might be a way to improve performance and to tailor the electrode to the cell requirements. In this work, we aim to shed light on the importance of the microstructure and the limitations it entails in SSB cathodes with the focus on a NCM811/Li_6PS_5Cl-composite. Setting up a mathematical model for simulation of electrochemical charge we use the finite element method (FEM) to approximate the underlying partial differential equations. We reconstruct CAM particle arrangements and validate the resulting charge profiles against experimental data, meanwhile highlighting the influence of the particle size distribution (PSD) and state-of-charge(SOC)-dependent simulation input, such as the lithium diffusion coefficient in NCM811 and the exchange

[z]E-mail: anja.bielefeld@phys.chemie.uni-giessen.de; juergen.janek@phys.chemie.uni-giessen.de

Journal of The Electrochemical Society, 2022 **169** 020539

current density at the NCM811/Li_6PS_5Cl-interface. We then assess the effect of residual voids and their partial interface coverage in a 1-particle-void model. Finally, we suggest a tortuosity-optimized microstructure that is feasible with laser ablation and provide first recommendations on its layout.

Model

Mathematical model.—With the aim to simulate charge transport and charge transfer processes in the simulated 3D domain, we set up a mathematical model comparable to Finsterbusch et al.[37] and Neumann et al.[38] which describes the time-dependent electrical potential and lithium ion concentration distribution by partial differential Eqs. based on charge and energy conservation.

To picture an SSB, we model two main types of material domains (SE and CAM) with their charge transport properties and two types of interfaces (SE/CAM and SE/lithium metal) that feature charge transfer from one material to the other. Generally, the origin of particle transport is due to either migration which is the field-driven movement of charged particles, due to diffusion, i.e. the particle movement driven by a concentration gradient or convection, i.e. thermal movement. Since convection can be neglected in solid-state battery cells, the molar flux $\vec{J}_\nu$ of any charged species ν consists of a diffusion and a migration term. It can be described by

$$\vec{J}_\nu = -\tilde{D}_\nu \nabla c_\nu + D_{0,\nu}\frac{c_\nu}{RT} F z_\nu \nabla\varphi, \qquad [1]$$

where $\tilde{D}_\nu$ refers to the chemical diffusion coefficient of species ν, given by

$$\tilde{D}_\nu = D_{0,\nu}\left(1 + \frac{\partial \ln \gamma_\nu}{\partial \ln c_\nu}\right). \qquad [2]$$

$D_{0,\nu}$ is its self-diffusion coefficient, the species concentration is referred to as c_ν and γ_ν is the activity coefficient; the term $\left(1 + \frac{\partial \ln \gamma_\nu}{\partial \ln c_\nu}\right)$ is also called the thermodynamic factor. The universal gas constant is referred to as R, φ is the electrical (Galvani) potential, T the temperature, F the Faraday constant, z_ν the charge number of the species ν.

The overall electric current density $\vec{j}$ can then be computed as

$$\vec{j} = \sum_\nu F z_\nu \vec{J}_\nu. \qquad [3]$$

The SE is modeled as a single-ion conductor, because we focus on a thiophosphate SE, such as Li_6PS_5Cl, with negligible electronic conductivity.[27]

Assuming solely ionic conduction in the SE implies no buildup of a lithium ion concentration gradient in the material, as there is no counter-ion that can balance this charge shift. The buildup of space charge layers at the interface is neglected in this model, because it is expected to be in the order of nanometers and its interfacial resistance is not significant.[39] From a mathematical point of view, this means, we can describe the SE as an (ionic) Ohmic conductor wherein charge transport is solely driven by the electric field, and hence drop the first term of the charge transport Eq. 1 to express the current density of lithium ions in the SE as

$$\vec{j}^{\,\mathrm{SE}} = \sigma_{\mathrm{ion}}^{\mathrm{SE}} \nabla\varphi, \qquad [4]$$

wherein $\sigma_{\mathrm{ion}}^{\mathrm{SE}}$ refers to the specific ionic conductivity of the SE.

The second material domain is the CAM which features ionic and electronic transport. However, as we model NCM811 in this work, the electronic transport is orders of magnitude faster than the ionic transport.[40] Accordingly, on the one hand, ions do not experience an electric field within the NCM phase, because it is already dissipated by the fast electron movement. Hence, for the ionic species ($\nu = \mathrm{ion}$) in the CAM, Eq. 1 reduces to the diffusion term

$$\vec{J}_{\mathrm{ion}}^{\mathrm{CAM}} = -\tilde{D}_{\mathrm{ion}}^{\mathrm{CAM}} \nabla c_{\mathrm{ion}}^{\mathrm{CAM}} \qquad [5]$$

and the continuity equation becomes

$$\frac{\partial c_{\mathrm{ion}}^{\mathrm{CAM}}}{\partial t} + \nabla(\tilde{D}_{\mathrm{ion}}^{\mathrm{CAM}} \nabla c_{\mathrm{ion}}^{\mathrm{CAM}}) = R_{\mathrm{I}}. \qquad [6]$$

The reaction rate R_{I} links the ion transport in the CAM to the (de-) intercalation that takes place at the CAM/SE-interface and $\tilde{D}_{\mathrm{ion}}^{\mathrm{CAM}}$ refers to the chemical lithium diffusion coefficient inside the CAM host structure which, in NCM, is amongst others dependent on the degree of lithiation and therefore SOC of the SSB. We will take a closer look at this parameter in the results.

On the other hand, the fast electron movement does not allow the buildup of an electron concentration gradient in the CAM and the transport of electrons ($\nu = \mathrm{eon}$) is solely caused by the electric field, reducing Eq. 1 to the migration term which is equivalent to Ohm's law, when inserted to Eq. 3:

$$\vec{j}_{\mathrm{eon}}^{\,\mathrm{CAM}} = -\sigma_{\mathrm{eon}}^{\mathrm{CAM}} \nabla\varphi \qquad [7]$$

To be consistent with the assumption of a negligible electric field in the CAM, we assume a high electronic conductivity of the CAM in the simulation (see Table S2). We accordingly loose the ability to quantify electronic limitations as reported by Neumann et al.[38] who, based on computer tomography data, reconstructed a NCM622/β-Li_3PS_4-composite cathode and simulated the cell discharge. They attribute capacity losses to the decrease of the specific electronic conductivity of their CAM upon its lithiation which gets even more severe when the contact of the electrode layer and the current collector is reduced.

The advantage of this simplification is that it decouples the flux Eqs. for electrons and ions and reduces computation significantly, as otherwise, one would have to treat the flux Eq. 1 for both species, ions and electrons and solve the Poisson equation additionally, which then leads to the Nernst-Planck-Poisson equation system.

At both interfaces, CAM/SE and SE/Lithium metal, charge transfer reactions take place whose reaction rates (as current densities) are usually described by the Butler-Volmer-Equation[41]

$$j_{\mathrm{BV}} = j_0\left[\exp\left(\frac{\alpha F\eta}{RT}\right) - \exp\left(-\frac{(1-\alpha)F\eta}{RT}\right)\right]. \qquad [8]$$

with the exchange current density j_0, the symmetry factor α and the overpotential η. The overpotential at the CAM/SE-interface is defined by

$$\eta = (\varphi^{\mathrm{CAM}} - \varphi^{\mathrm{SE}}) - E_{\mathrm{eq}}^{\mathrm{CAM}}, \qquad [9]$$

where $E_{\mathrm{eq}}^{\mathrm{CAM}}$ refers to the equilibrium potential difference, thus the state in which the anodic and the cathodic current are equal and there is no net current. The electric (Galvani) potential at the CAM particle surface is φ^{CAM} and the local electric (Galvani) potential of the electrolyte is φ^{SE}. The insertion and extraction of lithium ions from the electrolyte into the CAM host lattice can be described as

$$\mathrm{Li}^+ + \mathrm{e}^- + \mathrm{V}_{Li^+} \rightleftharpoons \mathrm{Li}^I; \qquad [10]$$

here Li^+ refers to a lithium ion in the electrolyte, e^- is the required electron, V_{Li^+} is a lithium vacancy of the host lattice and Li^{I} describes the intercalated lithium. With this, the exchange current density can be written as Ref. 42, 43

Journal of The Electrochemical Society, 2022 **169** 020539

$$j_0 = F \exp\left(-\frac{\alpha E_{ex}}{RT}\right) \exp\left(-\frac{(1-\alpha)E_{in}}{RT}\right) \times [k_{ex} c_{Li^+}]^{\alpha} [k_{in} c_{Li^+} c_{V_{Li}^+} c_{e^-}]^{1-\alpha}. \quad [11]$$

Here, the activation energies for lithium insertion and extraction are referred to as E_{in} and E_{ex}, the associated rate constants are k_{in} and k_{ex} and the concentrations of lithium ions, electrons, lithium vacancies and intercalated lithium are c_{Li^+}, c_{e^-}, $c_{V_{Li}^+}$ and c_{Li^i}, respectively.

Most terms in Expression 11 are constant during the cell charge: The concentration of lithium ions in the SE is assumed to be constant at the interface, because, as described above, the single-ion conduction property of the SE forbids the buildup of concentration gradients. Also the electron concentration can be assumed constant due to the high electronic conductivity of the CAM.

However, the concentration of lithium in the CAM and the availability of lithium vacancies in the host structure change upon charge, and the exchange current density at the CAM/SE-interface is therefore dependent on the SOC. A way to experimentally obtain the exchange current density is via the charge transfer resistance R_{CT} that can be measured by electrochemical impedance spectroscopy (EIS)[10] and contains the exchange current density[43]

$$R_{CT} = \frac{RT}{zFAj_0}. \quad [12]$$

On the anode interface we model the plating of lithium metal by the Butler-Volmer equation as well. However, as this work is focused on the cathode composite, we assume a high and SOC-independent anode exchange current density.

The model parameter values are specified in Table S2, accompanied by an overview of all model equations, including the boundary conditions, in Fig. S3 and Table S1.

Geometrical model.—In order to validate the mathematical model, to study the influence of residual voids, different PSDs, SOC-dependent input parameters and to provide a prospective on microstructured SSB cathodes, we set up different instances of the geometrical model:

- reconstruction of CAM particle microstructure
- 1-particle model with voids
- cone-type microstructures

The particle-type microstructure is an attempt to reconstruct the electrode microstructure reported by Rueß et al.[10] with 70 wt% polycrystalline NCM811 and 30 wt% Li_6PS_5Cl and a residual void space of 14%. As Rueß et al. explain, the ASSB cell does not show major issues with electronic percolation, albeit the absence of carbon black in the composite, and the CAM particles therefore have to be well-connected. The microstructure generation is not entirely analogue to Park et al.,[44] but with a similar Ansatz in GeoDict[45] using the GrainGeo Module followed by an import to Comsol Multiphysics 5.4[46] for the electrochemical simulation. The CAM particles are represented by interconnected spherical particles that follow a particle size distribution and the SE is assumed to be in ideal contact, filling all remaining volume. Figure 1 provides an overview of the microstructure generation process that is described in detail in the supplementary information . The simulation volume of the cathode composite is $(40 \times 40 \times 40)\mu m^3$ with a 10 μm SE separator in positive z-direction and a 1 μm current collector in negative z-direction (see Fig. 1, lower right).

The 1-particle model consists of one CAM particle with a given particle diameter, which is connected to the current collector as displayed in Fig. 2. To assess the influence of residual voids in SSB cathodes, voids with the shape of hemispheres are generated at the particle surface. The void distribution is random, the void size and the CAM/SE interface covered by the voids can be chosen. The void generation is described in the supporting information and different void-containing microstructures are displayed in Fig. 2 next to an SEM-image of a NCM811/Li_6PS_5Cl-cathode composite that was manufactured in a press cell. The advantage is its simplicity, both phenomenologically and computationally in comparison to the reconstructed electrode microstructure.

The idea of optimizing the electrode microstructure leads to studying a cone-type geometry as displayed in Fig. 3, wherein the CAM has the shape of a truncated cone and the SE fills all remaining space. In order to obtain realizable microstructures, the thick end of the CAM-cone is at the current collector and the thin end at the separator. This way, one can either imagine a dense SE separator with a porous SE structure (e.g. mitigated by pore builders) on top whose porosity is filled with CAM or a thick dense SE layer which is laser structured and whose resulting laser-formed "pores" are filled with CAM particles.

These geometries are simpler than the reconstructed CAM particle arrangements as they do not resolve each CAM particle, but only the macroscopic arrangement. The use of periodic boundary conditions permits to simulate a unit cell instead of a many-particle geometry as in the reconstructed particle arrangements. For further explanation on the geometry properties and the meshes we refer to the supplementary information, with mesh examples and parameters in Fig. S5.

Results/Discussion

We focus on simulating a constant current charge step, because we use experimental input that was measured during the 1st charge as well. Even though the lithium diffusion coefficient and the exchange current density should be material (combination) coefficients, Rueß et al.[10] show that the charge transfer resistance in particular, can be quite distinctive from charge to discharge. The origin is the formation of a high-impedance cathode solid electrolyte interface (CEI) due to degradation at the CAM/SE-interface.[17,18]

Validation.—The validation is conducted with respect to the SSBs studied by Rueß et al.,[10] Trevisanello et al.[11] and Conforto et al.[47]. The microstructure-describing parameters can be found in Table S3. To assure reproducibility, three types of the microstructure are modeled using different random seeds upon particle creation. The particle arrangements are therefore not identical and have slightly different PSDs (Fig. 5).

The CAM surface area of the particle arrangements is 0.17 $m^2\,g^{-1}$ which is slightly smaller than the experimentally obtained value of 0.2 $m^2\,g^{-1}$.[11] We explain this by the surface roughness of the NCM visible in the SEM-images in Fig. 2 (right) that is not part of the microstructure model, because solely spherical secondary CAM particles are modeled. For the relatively thin model electrode the active surface area relative to the electrode cross section is in the order of 10. This means that about a tenth of the current density applied to the cell arrives at each CAM surface, assuming a homogeneous current distribution.

Figure 4 shows the voltage curve for a galvanostatic charge with charge rates between 0.02 C and 0.5 C for the three microstructure geometry models and the experiment. Overall the three microstructures lead to very similarly shaped voltage curves, indicating a good reproducibility among themselves. At the rate of 0.02 C, the experiment and the simulation start off identical until 50 mAh g^{-1}, where the simulation slightly overestimates the cell voltage. However, this discrepancy is quite low and the curve shape is very similar. At the higher charge rate of 0.1 C, the experimentally obtained voltage curve has a similar shape compared to the lower rate, but a higher overpotential, as expected from the simulation. The simulated cell voltage approaches the experiment for the entire voltage window, but with a slightly different shape. At the beginning of charge below 50 mAh g^{-1} and between 100 mAh $g^{-1} \leqslant$ capacity $\leqslant$ 150 mAh g^{-1}, the simulation underestimates

Journal of The Electrochemical Society, 2022 169 020539

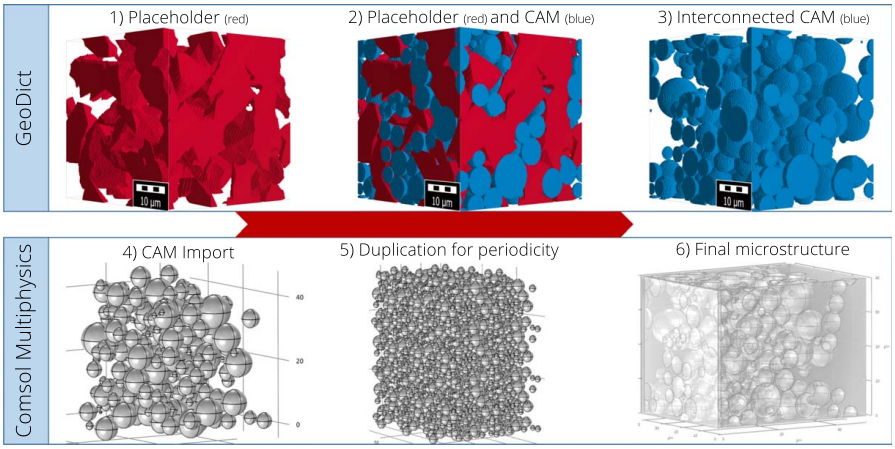

Figure 1. Procedure of geometry generation for the particle-type microstructures in GeoDict[45] and Comsol[46] linked by the corresponding Matlab interfaces.

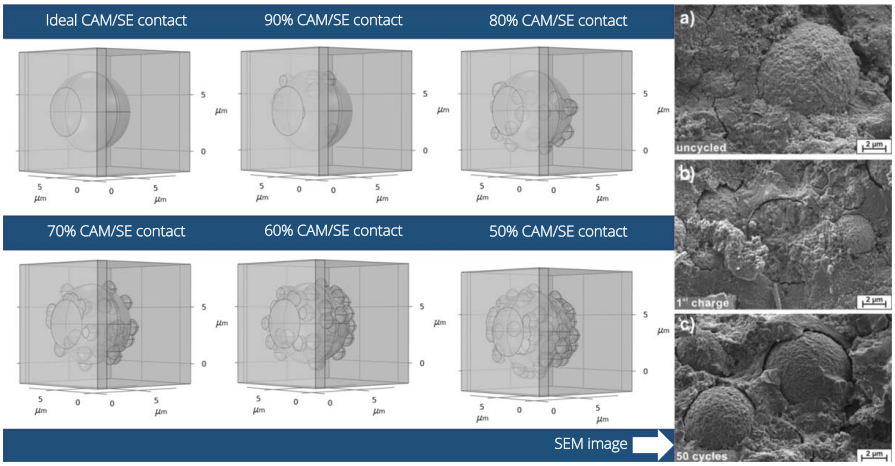

Figure 2. The 1-particle model featuring different void coverage from ideal to 50% CAM/SE contact aside a SEM-image of a composite electrode at a) an uncycled stage, b) after the 1st charge and c) after the 50th charge, adapted with permission from Koerver et al.[8]. Copyright (2017) American Chemical Society.

the overpotential. Between 50 mAh g^{-1} ⩽ capacity ⩽ 100 mAh g^{-1} and above 150 mAh g^{-1} the simulation overpotential is lower than the experimental one. The elevated charge rate of 0.5 C intensifies these discrepancies between simulation and experiment. The simulated overpotential at the beginning of charge is too small, approaches the experimental result around 25 mAh g^{-1} and underestimates it between 50 and 100 mAh g^{-1}. Indeed, the simulated voltage gradient increases significantly around 4.0 V, so the overall cell charge capacity is close to the measured one. The charge profile shape is discussed in more detail in the context of SOC-dependent input parameters.

For further comparison, Fig. 4 shows the differential capacity $dQdV^{-1}$ as function of the cell voltage. Here, the maximum of the simulated curve is not as high as in the experiment, but the overall course of the $dQdV^{-1}$ curve can be recognized. The simulation data at the low rate resembles the one measured in a NCM811/Li half-cell by Märker et al.,[48] where two peaks at 3.7 and 3.8 V can be identified. In the experimental $dQdV^{-1}$ curve, these two peaks become indistinct which indicates that the kinetics is limiting, already at 0.1 C rate. Less pronounced, this is also visible in the simulated data at 0.1 C, where the two peaks blur into one broader peak.

Despite these slight deviations, we consider the simulation and the experiment in good agreement given the complexity of real cells and their microstructure and the comparably simple mathematical representation. However, from the modeling point of view, the underlying geometry, its meshing and the various input parameters are quite challenging, computationally. Furthermore, none of the simulation input has been fitted to meet the experimental data.

Input parameters.—All simulation models are just as valid and as reliable as their input is. We therefore rely on the galvanostatic intermittent transient technique (GITT) and the EIS measurements preformed by Rueß et al.[10] and impedance modeling for the PSD by Conforto et al.[47] All input parameters were measured on the same

Journal of The Electrochemical Society, 2022 **169** 020539

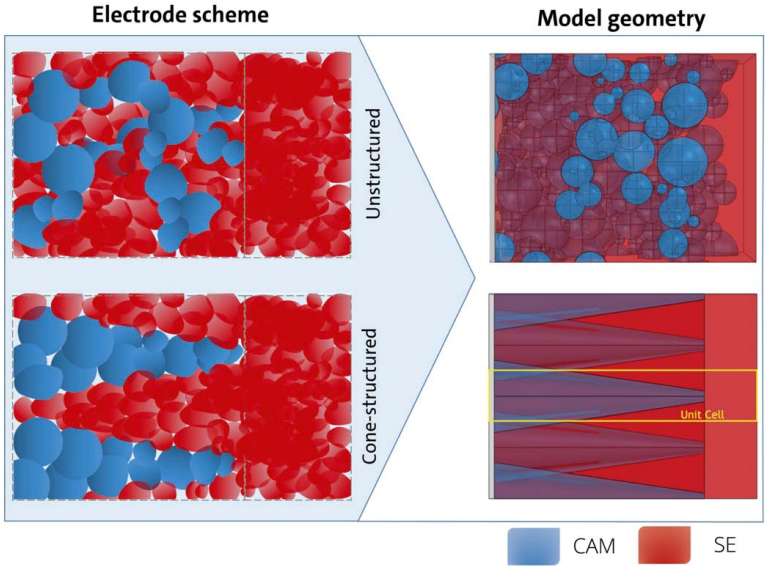

Figure 3. Schematic of electrode structuring and its realization in the model geometry compared to unstructured particle arrangements. The yellow box indicates the unit cell in the cone model.

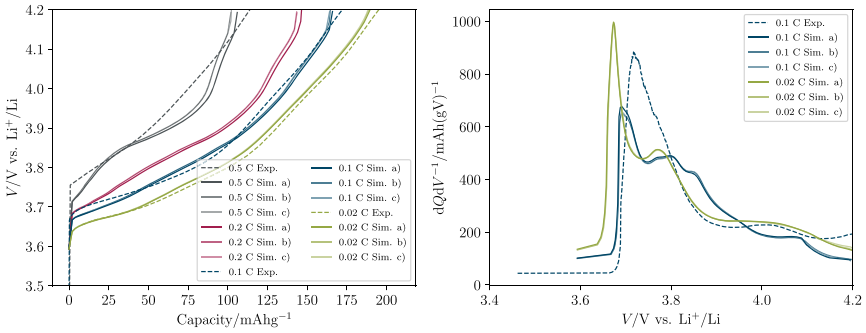

Figure 4. Charge voltage (left) and differential capacity $\mathrm{d}Q\mathrm{d}V^{-1}$ (right) for different charge rates and three microstructures a), b) and c) that differ in their random seed in comparison to experimental data.

materials that we validate the resulting voltage curves against. Two of these input parameters, the lithium diffusion coefficient in NCM811, $\tilde{D}_{\mathrm{Li}}$, and the exchange current density of the NCM811/Li_6PS_5Cl-interface, j_0, depend on the lithiation degree and, together with the PSD, these parameters are discussed in further detail in the following sections.

Particle size distribution.—To understand the impact of the CAM PSD, we considered model geometries with different maximal particle sizes. As explained by Conforto et al.,[47] the measurement uncertainty in the EIS-based technique increases for higher CAM particle sizes, because the method relies on the presence of finite-space diffusion and its reliability suffers from the shift toward semi-infinite diffusion in large particles.

For the simulation, the S-PSD has up to 11 μm-sized particles, the M-PSD features particle sizes below 14 μm and the L-particle arrangement contains particles with up to 20 μm in diameter. The occurrence of the particle sizes is displayed in Fig. 5a) and differences are difficult to notice, because all PSDs are very similar below 11 μm. The few larger particles of the M- and L-PSDs are easily overlooked, but they occupy significant volumes which has consequences for the electrode performance. The simulated voltage profiles of these PSDs are apposed in Figs. 5b–d): The larger the particles get, the higher the overvoltage gets and while the S-PSD results match the experimental data quite well, both the results from PSDs with larger particles deviate from it and the deviation gets more severe with higher C-rates. The L-PSD even shows significant deviations from the experimental data for 0.02 C. The simulated voltage profiles all feature a similar shape, however the increased

Journal of The Electrochemical Society, 2022 **169** 020539

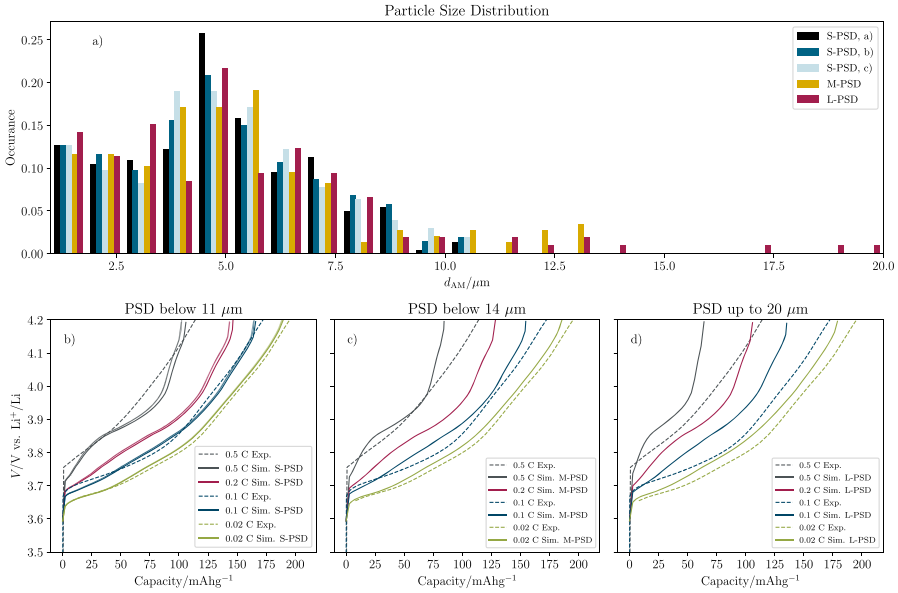

Figure 5. a) PSDs of the microstructure instances and the simulated charge voltage in comparison to experimental data for a PSD b) below 11 μm, c) below 14 μm and d) up to 20 μm.

voltage gradient that we observed above 4 V for 0.5 C is even steeper in the L-PSD.

Figure 6, which shows the lithium concentration in the CAM of the model geometries at the end of a 0.2 C charge for all PSDs, delivers a possible explanation for these discrepancies: Even though the particle size histograms in Fig. 5a) look quite similar, the model geometries are clearly different. Although the larger particles occur comparably seldom, they consume a larger volume fraction than the smaller ones. This results in smaller surface area overall, because the volume fraction of the CAM is held constant and less volume is left for the smaller particles. Table I indicates what this entails for the amount of CAM particles and the CAM surface area for the different PSDs. The CAM surface area for the S-PSDs is around 0.17 m^{2}g^{-1}, the M-PSD has 0.14 m^{2}g^{-1} and the L-PSD offers 0.11 m^{2}g^{-1} which is equivalent to a loss of 35% surface area for the S-PSD to the L-PSD and around 50% less particles.

The higher overpotential in Figs. 5b–d) stems from two causes: The larger particles offer less active surface area for lithium ion

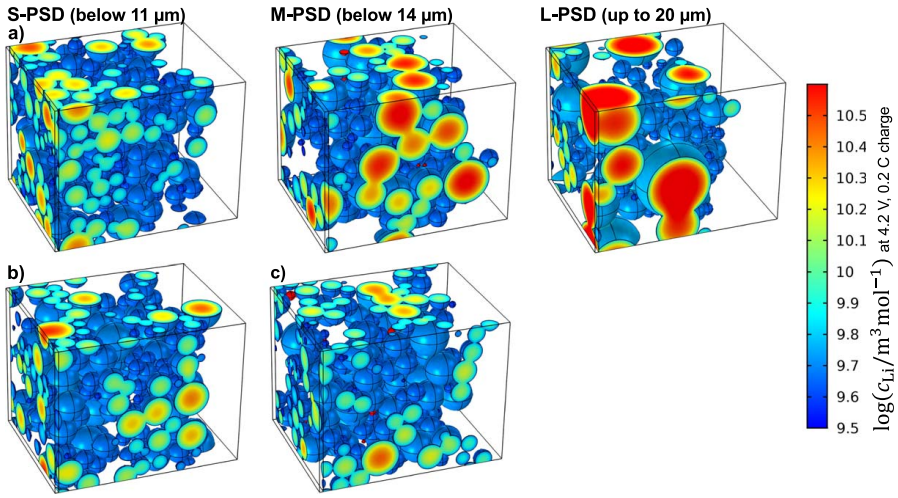

Figure 6. Lithium concentration (logarithmic) in the CAM at the end of a 0.2 C charge for the different PSDs from Fig. 5.

Journal of The Electrochemical Society, 2022 **169** 020539

Table I. Properties CAM PSDs.

PSD	S	S	S	M	L
Realization	a)	b)	c)	—-	—-
# AM particles	266	249	248	177	128
Surface area (m^2g^{-1})	0.173	0.172	0.167	0.139	0.113

extraction out of the NCM particles and, in addition, the diffusion pathways inside these larger particles are longer and therefore the lithium concentration gradient in the NCM particles builds up faster and the cutoff voltage is reached earlier. The logarithmic lithium concentration graph in Fig. 6 confirms this, showing considerably more CAM particle volume of red color for the L-PSD geometry than for the S-PSD geometries. A significant portion of the larger particles is not activated at all and the inner parts remain highly lithiated. This leads to the reduced charge capacities of Fig. 5d).

Lithium diffusion coefficient in NCM811 and exchange current density.—Albeit it is well-known that the diffusion of lithium ions in the NCM host structure is dependent on the degree of lithiation, many simulation studies use constant $\tilde{D}_{Li}$[49–52] (Falconi[53] provides a detailed overview thereof). As Märker et al.[48] and Van der Ven et al.[54] explain, the diffusion of lithium is affected by the diffusion path/mechanism and the energy landscape in the host material. In layered structures, such as NCM811, lithium diffusion can take place as a single and a divacancy hop where the latter has a lower activation energy and is therefore favored. This means that because a delithiated layered structure offers more possibilities for divacancy hops, an increase in the lithium mobility and $\tilde{D}_{Li}$ can be observed, as in Fig. 7a). However, this trend does not prevail until the NCM is completely delithiated, but $\tilde{D}_{Li}$ drops at 4.15 V due to a decreased slab distance whose root cause is the interaction of the oxygen layers.[54] According to Eq. 11

$$j_0 = F \exp\left(-\frac{\alpha E_{ex}}{RT}\right)\exp\left(-\frac{(1-\alpha)E_{in}}{RT}\right) \times [k_{ex} c_{Li'}]^{\alpha} [k_{in} c_{Li} {}^{+} c_{V_{Li}^{+}} c_{e^-}]^{1-\alpha},$$

the exchange current density j_0 at the NCM811/Li_6PS_5Cl-interface is expected to exhibit a negative parabolic shape with a maximum at an intermediate lithiation degree. Figure 7a) shows the course of j_0: At the beginning of charge (3.6 V) the CAM is fully lithiated and the concentration of lithium vacancies approaches zero, leading to a diminished exchange current. With rising vacancy concentration the exchange current increases, even though more vacancies also imply less intercalated lithium. Upon proceeding delithiation of the CAM particle, the concentration of intercalated lithium at the interface drops and a lithium concentration gradient builds up in the particle with a higher lithium density at the particle center than at its surface due to the comparably slow diffusion of lithium inside the particle. This effect can be seen in the intermediate voltage (from 3.8 to 4.0 V) where the exchange current density decreases slightly. The subsequent drop of j_0 above 4.0 V is due to the fact that the concentration of intercalated lithium reaches small values.

With the objective to study the influence of the SOC-dependence of $\tilde{D}_{Li}$ and j_0 to the simulated voltage profile, we perform charge simulations for different C-rates with SOC-dependent and constant input parameters, shown in Figs. 7b–f). For both input parameters, two constant values are chosen: The maximum values $\tilde{D}_{Li,1} = 6.8 \cdot 10^{-12}$ cm^2 s^{-1} and $j_{0,1} = 1.55 \cdot 10^{-5}$ A cm^{-2} and for the diffusion coefficient the value of the plateau at [3.7, 3.9] V and [4.05, 4.15] V which is $\tilde{D}_{Li,2} = 3.5 \cdot 10^{-12}$ cm^2 s^{-1} and a mean exchange current density of $j_{0,2} = 0.90 \cdot 10^{-5}$ A cm^{-2}, accordingly. Figure 7 features one plot for each set of input parameters; for direct comparison of the parameter sets we refer to Fig. S6 in the supporting information where each subplot is dedicated to a C-rate. The SOC-dependent charge profiles in Fig. 7b) are the same as those for S-PSD a) in the Figs. 4 and 5b).

For 0.02 C, all simulated voltage profiles are very similar in a wide voltage range of 3.7 to 4.17 V, but the initial overvoltage of the experimental data is only accurately met with the SOC-dependent input parameters. At high voltages, above 4.17 V, the constant input parameters model the profile better than the SOC-dependent ones. However, the simulation data of the constant input do not differ significantly at the low current rate, indicating that neither lithium diffusion in the NCM nor the interface charge transfer are limiting. At the higher C-rates the above-mentioned effects are more enhanced: The initial voltage increase is best modeled by the SOC-dependent parameters at 0.1 C and the constant coefficients are more suitable to describe the end of charge. Generally, the maximal constant input parameter set $\{\tilde{D}_{Li,1}, j_{0,1}\}$(Fig. 7c)) causes a smaller overvoltage than all other simulations and than the experiment. The set with a decreased exchange current density $\{\tilde{D}_{Li,1}, j_{0,2}\}$ (Fig. 7e)) exhibits the same shape, but slightly higher overvoltage. The simulation that reproduces the experimentally obtained data best stems from the mean diffusion coefficient and the maximum exchange current density (Fig. 7d)), although it does not reproduce the initial voltage increase. Again, a decrease in exchange current density with the combination $\{\tilde{D}_{Li,2}, j_{0,2}\}$ (Fig. 7f)) leads to an increase in overpotential, while maintaining the curve shape.

The voltage profiles in Fig. 7b) clearly reflect the SOC-dependence of their input: The slow lithium diffusion and hindered lithium extraction from the AM at the beginning of charge result in the steep voltage increase that describes the experimentally obtained data better than the constant input parameters do. This steep increase also implies that voltage regions with facilitated charge transfer are reached quickly (rise of the exchange current density in Fig. 7a) with a maximum at 3.8 V). Meanwhile, $\tilde{D}_{Li}$ also increases up to 3.7 V, but plateaus for about 0.2 V and reaches its maximum around 3.95 V. The faster charge transfer at the interface and faster lithium transport in the NCM particle are then reflected by a flatter shape of the charge curve compared to the beginning of charge and compared to the constant input parameter sets. Finally, the lithium depletion at the CAM particle surface advances, the lithium diffusion slows down due to decreasing inter-slab distance and the interface current decreases as well. This is why the simulated voltage increases and the cutoff is reached earlier than for the constant parameter sets.

But why is this increase at elevated voltages not seen in the experimental data? Either this phenomenon is compensated by a different effect which is not described by the mathematical model, one or both of the SOC-dependent parameters are inaccurate in this voltage range or the experimental charge data are incorrect. We presume a combination of all the above, however, we consider the latter as least probable, because other experimental data of SSBs do not show this phenomenon either: E.g. Lee et al.[29] report an SSB featuring a NCM955/Cl-Argyrodite composite cathode under symmetric cycling of 0.5 C with a voltage window of 2.5 to 4.25 V vs. Li^+/Li and do not observe this effect.

What has been shown and explained, is a rapid increase in voltage when a higher cutoff voltage is chosen and lithiation degrees lower than $Li_{0.22}Ni_{0.8}Mn_{0.1}Co_{0.1}O_2$ are reached.[48,55] Concerning the model simplifications, most assumptions, including the neglect of interfacial effects other than the Butler-Volmer kinetics (e.g. degradation effects that kick in at high voltage and elevated C-rate, the formation of voids or the presence of space charge layers) and the assumption of the SE acting as an Ohmic ion conductor should rather underestimate the simulated overvoltage. The only influence that would act contrariwise is the modeling of NCM particles as spherical secondary particles, neglecting their primary particle structure and surface roughness that increases the active surface area and would lower the overpotential.

Journal of The Electrochemical Society, 2022 **169** 020539

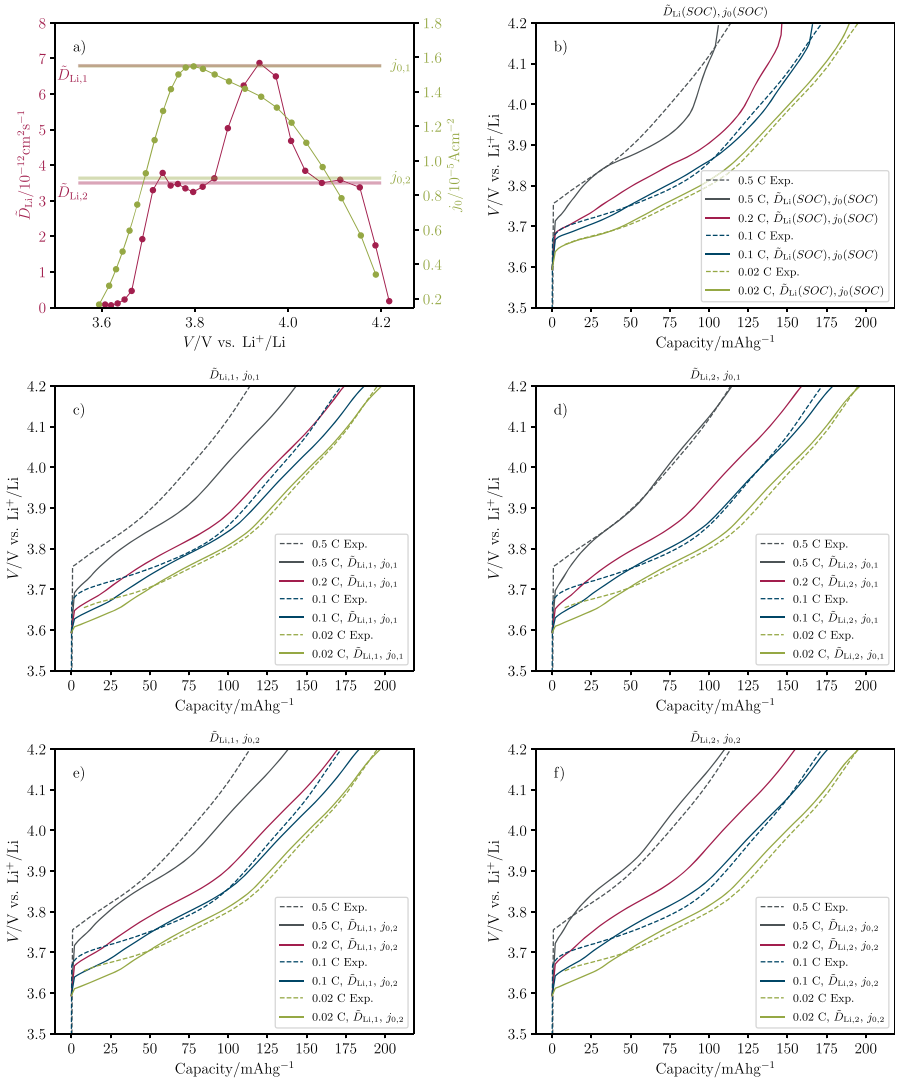

Figure 7. a) SOC-dependent input parameters: Lithium diffusion coefficient in NCM811 $\tilde{D}_{\mathrm{Li}}$(red) and exchange current density j_0(green) and the constant values $\tilde{D}_{\mathrm{Li},1}$, $\tilde{D}_{\mathrm{Li},2}$, $j_{0,1}$ and $j_{0,2}$. b) Voltage profile for the SOC-dependent input parameters and c)-f) voltage profiles for different combinations of constant input parameters whose values are indicated in a).

The SOC-dependent $\tilde{D}_{\mathrm{Li}}$ in NCM811 is indeed difficult to obtain from the typical two-electrode impedance measurements of full cells, because the impedance contribution of the anode interferes with the cathode contribution and the measured $\tilde{D}_{\mathrm{Li}}$ may therefore also contain influences from the anode. In domains where the exchange current is high, but the diffusion is comparably low, between 3.75 and 3.9 V, the composite will not be lithiated homogeneously which leads to an underestimation of $\tilde{D}_{\mathrm{Li}}$. At elevated voltages, however, the miscibility gap of NCM limits the reliability of the typical assumptions in the evaluation of the GITT and EIS measurements. $\tilde{D}_{\mathrm{Li}}$ is therefore not exact in this domain and may be underestimated significantly, which can explain the steep voltage increase in the simulation at the end of charge for elevated C-rates, in particular. The measurement of j_0 is generally more accurate and only the presence and the growth of a CEI leads to discrepancies: The CEI grows during the measurement which results in the asymmetric shape in Fig. 7 and upon advanced degradation, the assumed Butler-Volmer behavior from Eq. 8 may not be correct anymore.

Reflecting upon the SOC-dependent and the constant input parameters in Figs. 7a–f), we notice that the choice of $\tilde{D}_{\mathrm{Li}}$ and j_0 heavily affects the simulation result. While the $\tilde{D}_{\mathrm{Li}}$ inherently varies

Journal of The Electrochemical Society, 2022 **169** 020539

typically by two orders of magnitude with the SoC, there is also a wide scattering of data in the literature, depending on the type of measurement and the evaluation method.[10,53] Clearly, despite its relevance, $\tilde{D}_{Li}$ is not a well and reliably known input parameter and we hope to trigger more work it in the future. Combining this issue of measurement reliability with the simulation sensitivity to $\tilde{D}_{Li}$ and j_0, we want to emphasize this is a potential Achilles heel in electrochemical simulation and that the often performed fitting of j_0 or the reaction rate constant to the simulation[53] should be rethought and used with caution.

Albeit the above mentioned issues, we rely on the SOC-dependent input parameters for the subsequent simulations, as we consider this as the best and physically correct choice.

Void influence.—Different studies,[24,25,27,56] both from experimental and theoretical perspective, have shown that voids in the electrode have an effect on the ionic pathways, the active interface area and correspondingly on the cell performance. The void space in ASSB cathodes is reported to be between 6 and 40%, depending on the manufacturing method, the cell layout and the materials. One the one hand, Ates et al.[57] report void fractions between 20 to 40% in slurry-processed, uncalendered NCM622/β-Li_3PS_4-composites with conductive carbons and oppanol. On the other hand, the infiltration of Li_6PS_5Cl into conventional $LiCoO_2$ cathodes can reduce the void fraction down to 6 to8%.[58] The commonly used technique of lab scale press cells goes along with porosities around 14% in polycrystalline NCM/Li_6PS_5Cl-composites[10,27] and 13% in $LiCoO_2$/Li_2S-P_2S_5-LiI-composites.[56]

However, to date, the effect of interfacial voids and their properties on the lithium diffusion in NCM are not clear and we therefore approach this issue in a 1-particle model studying different active interface coverage, void sizes and distributions.

Depending on the size and distribution, the modeled voids represent different undesired phenomena inside SSB cathodes: The larger voids can be interpreted as partial contact loss between CAM and SE particles resulting from NCM particle shrinkage upon delithiation,[8] while the smaller voids can result from manufacturing or can represent inactive material, such as carbon or binder that reduces the CAM/SE-interface area.

Active interface area.—As it is a common particle size for polycrystalline NCM, we choose a 7 μm-sized particle and cover parts of its surface area with 1.4 μm-sized void hemispheres. Decreasing the number of voids, the remaining active interface area goes down and we generate geometries whose remaining active interface area is no more than 52% of the pristine CAM particle surface area A, illustrated in the lower part of Fig. 8. Simulating different charge rates between 0.02 C and 0.5 C, Fig. 8 shows the resulting voltage profiles and the void-induced overpotential at two arbitrarily chosen capacities of 50 and 100 mAh g^{-1}. The void overpotential is calculated by subtracting the voltage of the void-containing geometry from the geometry with the ideal CAM/SE-interface: At the small charge rate of 0.02 C, the active surface area reduction due to voids does not noticeably affect the voltage profile. Only at the beginning of charge and toward the end of charge, the voids lead to slightly higher overpotential which is likely to be on account of the low $\tilde{D}_{Li}$ at these SOCs (see Fig. 7).

At 0.1 C, the overpotential increases with decreasing active interface area and increasing void density at the surface, because the lithium extraction from the NCM is not as facile as for ideal contact between SE and CAM. The diffusion limitation of the low $\tilde{D}_{Li}$ at elevated voltages kicks in earlier, because the concentration gradient inside the particle builds up faster and the lithium at the particle center is barely extracted. The effect is even more distinctive at 0.2 and 0.5 C rate, where the overpotential rises up to 50 mV for 52% remaining interface area at 100 mAh g^{-1}. Overall, the void overpotential is higher at 50 mAh g^{-1} compared to 100 mAh g^{-1}.

The same study is performed on a 5 μm-sized particle to ascertain that the observed effect is reproducible for other CAM particle sizes and particle-to-void-size-ratios. Figure S7 shows a similar impact of void surface coverage and charge rate as for the larger CAM particle. Since the diffusion pathways are overall shorter in a 5 μm-sized particle, the resulting overpotential is slightly smaller. The values of the void overpotential in lighter coloring in Fig. 8 (right) correspond to the 5 μm-sized CAM particle and one can observe in direct comparison that the trends are the same for both particle sizes, while the magnitude is smaller for the small CAM particle.

Void distribution.—Apart from the CAM coverage with voids, the size and distribution of residual voids in SSB electrodes is widely unknown and to assess its significance, we introduce different void sizes d_{Void} on the $d_{CAM} = 7$ μm-sized CAM-particle at a constant remaining active interface area of 70% and describe these by d_{CAM}/d_{Void}, the particle-to-void-size-ratio. This ratio is altered between 1.2 and 10 corresponding to void sizes of maximum 4 μm and minimum 0.7 μm. The void size can also be regarded as a measure for the homogeneity of the void distribution, because the latter is indirectly affected by the particle-to-void-size ratio: To cover 30% of the active surface area 160 small voids of 0.7 μm diameter are uniformly distributed by random void placement, but only two 4 μm-sized voids are needed for the same surface coverage. These two cases are illustrated in the lower part of Fig. 9 and it is clearly visible that the contact of the CAM particle to the SE is inhomogeneous for the large voids.

There are two main types of voids that occur in actual composite cathodes:

Larger voids that can be considered as a particle contact loss between CAM and SE, e.g. due to the volume changes of NCM particles upon cycling.[8,9] Possibly, SE particles are only partly disconnected, depending on their mechanical rigidity. Still, as an upper boundary, we can think of the interfacial contact loss as whole SE particles that are disconnected from the CAM particle. The void size is then in the range of SE particle sizes, e.g. between 1 and 10 μm.[27]

Smaller voids that can be regarded as residual porosity which results from electrode manufacturing and the morphology of the SE particles.[56] Just like information on the void space itself, information on the void size is scarce and we estimate it to be below 2 μm in size, depending on the electrode homogeneity. Generally, also these voids scale with the SE particle size.[59]

The charge profiles in Fig. 9 indicate that the homogeneity of the void distribution matters for the charge performance, especially at elevated C-rates. Particularly, the largest void size goes along with an elevated overpotential compared to the more homogeneously distributed small-sized voids. In the case of a large void, locally, the inactive interface area is large and the lithium concentration gradient in the particle is comparably abrupt. In contrast, many uniformly distributed voids can partly compensate the local inactive surface area by lithium diffusion inside the CAM particle.

Moreover, assuming that the SE becomes more compact upon cycling due to external pressure, the influence of the smaller voids is expected to decrease.

We are aware that this model approach is not capable to quantify the influence of voids in the cathode composite on ionic percolation, as we are focusing on the role of the active surface area and one CAM particle only. The surface effect, we observe, alone is dependent on the void size, the void distribution and its surface coverage. Unsurprisingly, the void induced overpotential is increased at elevated current densities and a homogeneous void distribution is preferable. This highlights that not only a homogeneous particle distribution in the composite is important,[27] but also a homogeneous void distribution. We encourage to consider this upon cell manufacturing, if voids cannot be avoided generally.

Journal of The Electrochemical Society, 2022 **169** 020539

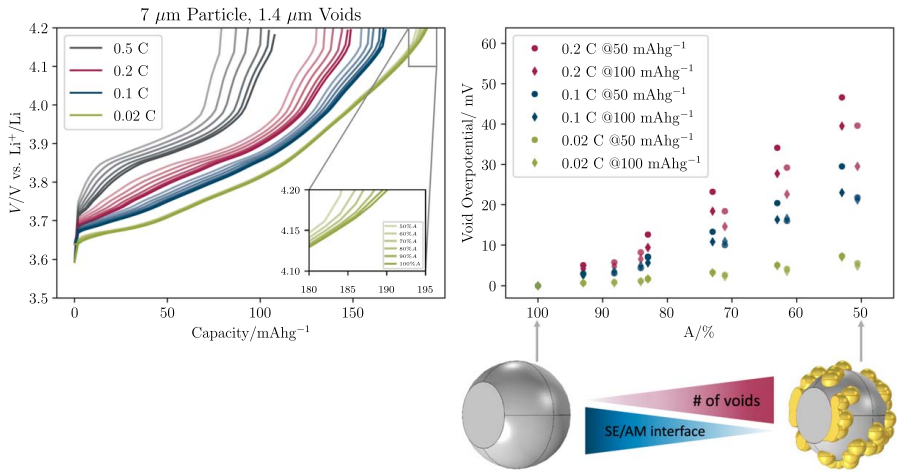

Figure 8. (left) Charge voltage profiles of different remaining void surface coverage in the 1-particle model at various charge rates and (right) the corresponding void overpotential at chosen capacities of 1.4 μm voids covering a 7 μm particle in darker coloring and a 5 μm particle in lighter coloring.

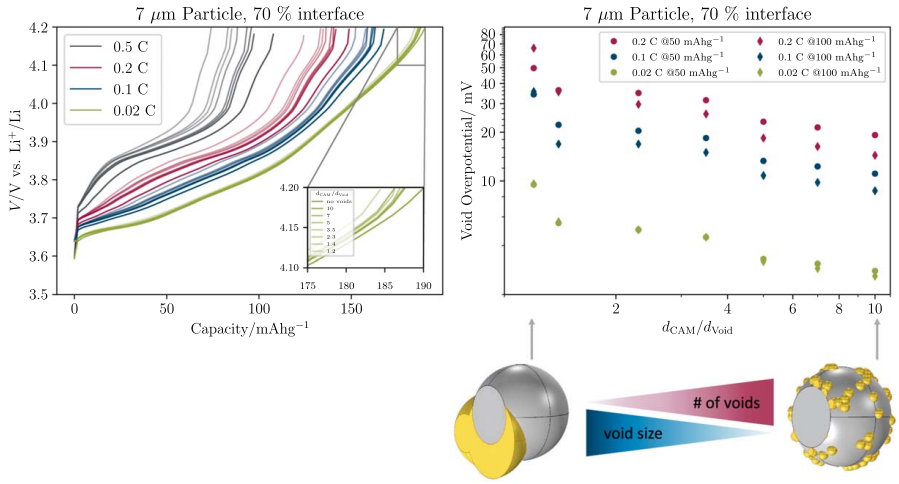

Figure 9. (left) Charge voltage profiles of different void-to-particle-size-ratios in the 1-particle model, various charge rates and (right) the void overpotential at chosen capacities over the particle-to-void-size-ratio. The remaining CAM/SE interface is 70%.

(Micro-)structured cathodes.—Highly tortuous ionic paths in composite cathodes for SSBs can have a crucial impact on the cell performance.[25,27] One way to tune the electrode composite and to minimize the tortuosity effect is to structure the electrode as displayed in Fig. 3, either by laser perforation of a dense SE layer and infiltration of CAM, by growing CAM pillars or similar approaches. To compare the cone-type structure with its disabled tortuosity to the typical microstructure of composites with individual CAM particles as shown above and the corresponding experiments, we choose a cone-type structure with the same features: An CAM volume ratio of 42% and an active surface area of 0.17 g m^{-2}.

Figure 10 (left) shows the charge profiles of the particle-type, unstructured microstructures, the cone-structured cathode and the experimental data. While the overpotential is generally reduced in the structured electrode, especially at elevated C-rates, the profile shape is the same as for the unstructured electrode. We attribute this behavior to the SOC-dependent input parameters, which we studied above and where we state that the curve shape is not primarily influenced be the microstructure, but by $\tilde{D}_{\mathrm{Li}}$ and j_0.

The reduction of the overpotential in the cone-structured model is quite moderate and we expect it to become more significant in thicker electrodes. Admittedly, thicker unstructured electrodes are challenging to simulate, because they require large numbers of CAM particles, which increases computation cost significantly.

For an elaborate electrode design we want to assess which channel/cone size or laser pattern should be targeted in SSB cathodes. For this purpose, we choose a higher CAM volume fraction than above (55 vol%), because high energy densities require

Journal of The Electrochemical Society, 2022 **169** 020539

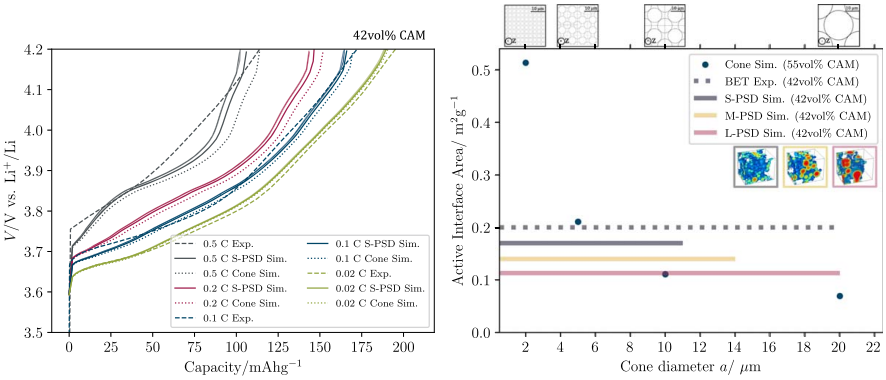

Figure 10. (left) Charge voltage of particle-type, unstructured microstructures and a cone-structured cathode with the same CAM/SE interface area and CAM/SE composition in comparison to experimental data at various rates. (right) Active interface area of cone-type microstructures with 55 vol% CAM depending on the cone diameter a compared to the interface area of the particle-type microstructures presented above that feature 42 vol% CAM.

high CAM loading and we compare different current collector facing cone diameters $a \in \{2, 5, 10, 20\}$ μm. The corresponding smaller cone diameter b at the separator interface is calculated according to Eq. 9 in the supporting information. Figure 10 (right) illustrates how the active interface area changes with the cone diameters a and that the 5 μm-sized cones exhibit a similar surface area as was obtained on the real cathode by BET.[11] Please note that the experiment and the particle-type microstructure models contain less CAM (42 vol%) than the cone-type structures and are therefore not directly comparable. While the larger cone sizes offer a smaller surface area around 0.1 $m^2\,g^{-1}$, the thin 2 μm-sized cones provide five times the interface area. Consequently, the charge profiles in Fig. 11 indicate a significantly higher overpotential for larger cones, and elevated C-rates in particular. The high active interface area and short diffusion paths inside the CAM for 2 μm-sized cones lead to flat voltage profiles even up to 1 C. For 5 μm-sized truncated cones, the voltage profiles are considerably steeper, but still around 100 $mAhg^{-1}$ can be charged at 1 C (constant current) until 4.2 V are reached. The performance of the larger cones of 10 and 20 μm is poor: The reduced interface area and the long diffusion paths inside the CAM are not favorable and the cutoff voltage is reached at low capacities.

To decouple the cone ratio b/a from the CAM volume fraction, we finally study cones that overlap by a factor of $(1 - dn)$ at the current collector. This allows us to obtain a more pointed cone as illustrated in Fig. S4 and to decrease b, while maintaining the CAM volume fraction and a. We compare this kind of truncated, overlapping cone structures for $a = 10$ μm in Fig. S8 with the previous cones structures at constant b/a ratio.The overlap even worsens the performance, so it not helpful to use smaller cone sizes at the separator, if the cone diameter at the current collector is not adjusted. This indicates again that a high surface area is the key for electrode optimization.

What this geometry model does not incorporate, is the surface roughness of the CAM, because we model a cone instead of discrete particles. Therefore, the actual active interface area might be larger and lead to improved performance. However, the model also does not feature voids that, in practice, would occur between CAM particles, between SE particles and at the SE/CAM interface and would lower the performance. It is not straightforward to estimate whether these two effects might compensate each other. Still, in our opinion, structuring of SSB cathodes has to be in the low μm-range, below 5 μm, in order to tune the electrode toward elevated current densities. To date, ultra-fast laser ablation-based electrode structuring has shown channel diameters around 12 μm in a conventional thick-film NCM111 cathode.[60,61] Hence, we like to encourage the generation even smaller channel sizes or other methods for SSB electrode structuring, such as the synthesis of NCM-microrods[62,63] that have to be oriented properly and in order to be infiltrated by small-sized SE-particles afterwards.

An alternative electrode design that abandons the presence of SE in the electrode entirely has been published recently.[64–66] Therein, the lithium ions diffuse through the active material layer instead of the SE and the absence of SE results in a higher CAM packing. Kim et al.[66] explain that this higher packing may compensate the low average voltage (1.9 V[67]) of $LiTiS_2$ with regard to the cell energy density and demonstrate $LiTiS_2$ as an alternative CAM candidate for these diffusion-dependent cathodes, as it possesses a comparably high $\tilde{D}_{Li}$ in the range of 10^{-8} to 10^{-9} $cm^2\,s^{-1}$. In NCM811, $\tilde{D}_{Li}$ is three orders of magnitude lower (see Fig. 7a)), so the diffusion-dependent cathode design is unlikely to become an option and fast ion conduction paths, as the microstructures suggested above, are required, still.

Conclusions

To assess the significance of the cathode microstructure on the SSB charge performance, we set up an electrochemical simulation on the microstructure level using the FEM. We created three different geometry models to validate and reproduce experimental data in typical CAM particle arrangements, to study the influence of remaining void space in a 1-particle model and to provide an outlook toward tortuosity-optimized structured cathodes using cone-type geometries.

In particular, we demonstrated that the SOC-dependence of $\tilde{D}_{Li}$ in NCM811 and j_0 at the NCM811/Li_6PS_5Cl-interface matters for the simulation and influences the charge performance significantly. Constant input parameters are not capable of accurately simulating the voltage curve and of reproducing the effect that e.g. the lithium di-vacancy concentration and the oxygen layer interaction of the NCM host structure have on $\tilde{D}_{Li}$. In our opinion, simulations in this field should assure to use and discuss proper SOC-dependent parameters and not blindly rely on literature findings that might not be appropriate for their study. We also strongly recommend to assure a more reliable and consistent experimental data set for $\tilde{D}_{Li}$.

Furthermore, we find that even relatively small amounts of large CAM particles in the PSD have a notable impact on the active surface area, as they consume a large volume in the microstructure. These large particles hinder lithium extraction due to their long diffusion pathways and the cell performance suffers. A careful design of the PSD that avoids large CAM particles is one way to

Journal of The Electrochemical Society, 2022 **169** 020539

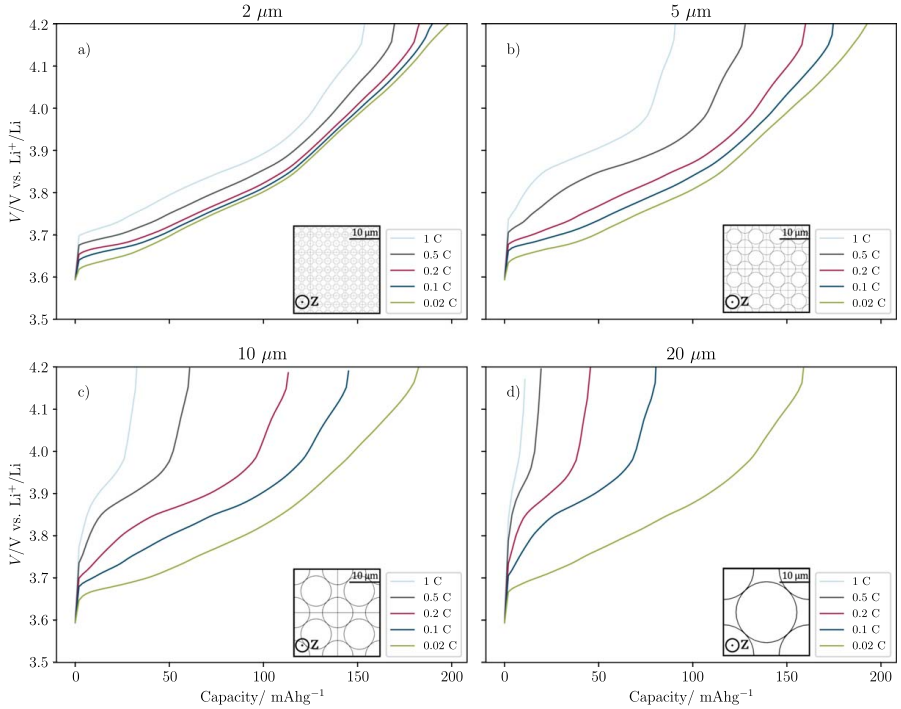

Figure 11. Charge voltage profiles for different cone-type microstructures at 55 vol% CAM differing in current collector facing cone diameter $a \in \{2, 5, 10, 20\}$ µm at C-rates between 0.02 and 1 C.

solve this issue. As an alternative to the polycrystalline NCM that we focused on in this study, one can use smaller, single crystal NCM particles.[12–14]

Although rarely analyzed, there is broad agreement that the volume occupied by voids in SSB cathodes should be minimized. We further want to recommend that the voids at the CAM/SE-interface should also be minimized in size to ensure a homogeneous distribution, if they cannot be avoided entirely due to manufacturing issues. One way to achieve this could be by isostatic hot pressing that has shown to improve the CAM/SE-contact, previously.[29] We encourage a deeper look into partial contact loss, its size and shape characteristics and evolution, both experimentally and theoretically, because it can affect the cell performance quite significantly.

Optimizing the cathode microstructure in SSBs can be a way to disable tortuosity effects, but requires channels in the low μm-range to ensure sufficient surface area, because, unlike liquid electrolytes, the SE does not infiltrate (micro-)porosities.

Altogether, we want to encourage a more sophisticated cathode design in SSBs that accounts for the materials prerequisites as well as for the targeted application. To provide further guidelines to experimenters, coupled (chemo-)mechanical and electrochemical simulations of the cathode composite are required on the microstructure level, as these can enlighten the mechanical behavior, the formation and evolution of voids and inter-particle cracks during cycling and therefore assess various degradation effects.

Acknowledgments

The authors thank the Volkswagen AG for the financial support of this work. The results, opinions and conclusions expressed in this publication are not necessarily those of Volkswagen Aktiengesellschaft.

Jürgen Janek thanks the German Federal Ministry of Education and Research (BMBF) for funding within the Cluster of Competence ”FESTBATT” (03XP0177A). The authors acknowledge helpful discussion with Philip Minnmann (JLU) and the consortium of the ”ProFeLi” project (03XP0184C) funded by the German Federal Ministry of Education and Research (BMBF).

ORCID

Anja Bielefeld https://orcid.org/0000-0003-2193-8375
Dominik A. Weber https://orcid.org/0000-0003-4357-9713
Raffael Rueß https://orcid.org/0000-0002-9274-4714
Jürgen Janek https://orcid.org/0000-0002-9221-4756

References

1. J. Janek and W. G. Zeier, *Nat. Energy*, **1**, 16141 (2016).
2. K. B. Hatzell et al., *ACS Energy Lett*, **5**, 922 (2020).
3. P. Adeli, J. D. Bazak, K. H. Park, I. Kochetkov, A. Huq, G. R. Goward, and L. F. Nazar, *Angew. Chem. - Int. Ed.*, **58**, 8681 (2019).
4. Y. Kato, S. Hori, T. Saito, K. Suzuki, M. Hirayama, A. Mitsui, M. Yonemura, H. Iba, and R. Kanno, *Nat. Energy*, **1**, 16030 (2016).
5. S. Randau et al., *Nat. Energy*, **5**, 259 (2020).
6. H. Lee, P. Oh, J. Kim, H. Cha, S. Chae, S. Lee, and J. Cho, *Adv. Mater*, **31**, 1900376 (2019).
7. A. Banerjee, X. Wang, C. Fang, E. A. Wu, and Y. S. Meng, *Chem. Rev.*, **120**, 6878 (2020).
8. R. Koerver, I. Aygün, T. Leichtweiß, C. Dietrich, W. Zhang, J. O. Binder, P. Hartmann, W. G. Zeier, and J. Janek, *Chem. Mater.*, **29**, 5574 (2017).
9. R. Koerver, W. Zhang, L. de Biasi, S. Schweidler, A. O. Kondrakov, S. Kolling, T. Brezesinski, P. Hartmann, W. G. Zeier, and J. Janek, *Energy Environ. Sci.*, **11**, 2142 (2018).

10. R. Ruess, S. Schweidler, H. Hemmelmann, G. Conforto, A. Bielefeld, D. A. Weber, J. Sann, M. T. Elm, and J. Janek, *J. Electrochem. Soc.*, **167**, 100532 (2020).
11. E. Trevisanello, R. Ruess, G. Conforto, F. H. Richter, and J. Janek, *Adv. Energy Mater*, **11**, 2003400 (2021).
12. R. Fantin, E. Trevisanello, R. Ruess, A. Pokle, G. Conforto, F. H. Richter, K. Volz, and J. Janek, *Chem. Mater.*, **33**, 2624 (2021).
13. C. Doerrer, I. Capone, S. Narayanan, J. Liu, C. R. M. Grovenor, M. Pasta, and P. S. Grant, *ACS Appl. Mater. Interfaces*, **13**, 37809 (2021).
14. C. Wang et al., *Energy Storage Mater*, **30**, 98 (2020).
15. X. Li et al., *ACS Energy Lett*, **4**, 2480 (2019).
16. Y. Xiao, L. J. Miara, Y. Wang, and G. Ceder, *Joule*, **3**, 1252 (2019).
17. F. Walther, R. Koerver, T. Fuchs, S. Ohno, J. Sann, M. Rohnke, W. G. Zeier, and J. Janek, *Chem. Mater.*, **31**, 3745 (2019).
18. F. Walther, S. Randau, Y. Schneider, J. Sann, M. Rohnke, F. H. Richter, W. G. Zeier, and J. Janek, *Chem. Mater.*, **32**, 6123 (2020).
19. S. P. Culver, R. Koerver, W. G. Zeier, and J. Janek, *Adv. Energy Mater*, **9**, 1900626 (2019).
20. X. D. Zhang, F. S. Yue, J. Y. Liang, J. L. Shi, H. Li, and Y. G. Guo, *Small Struct*, **1**, 2000042 (2020).
21. D. Kitsche, Y. Tang, Y. Ma, D. Goonetilleke, J. Sann, F. Walther, M. Bianchini, J. Janek, and T. Brezesinski, *ACS Appl. Energy Mater*, **4**, 7338–7345 (2021).
22. F. Walther, F. Strauss, X. Wu, B. Mogwitz, J. Hertle, J. Sann, M. Rohnke, T. Brezesinski, and J. Janek, *Chem. Mater.*, **33**, 2110 (2021).
23. F. Strauss, T. Bartsch, L. de Biasi, A. Y. Kim, J. Janek, P. Hartmann, and T. Brezesinski, *ACS Energy Lett*, **3**, 992 (2018).
24. A. Bielefeld, D. A. Weber, and J. Janek, *J. Phys. Chem. C*, **123**, 1626 (2019).
25. A. Bielefeld, D. A. Weber, and J. Janek, *ACS Appl. Mater. Interfaces*, **12**, 12821 (2020).
26. T. Shi, Q. Tu, Y. Tian, Y. Xiao, L. J. Miara, O. Kononova, and G. Ceder, *Adv. Energy Mater*, **10**, 1902881 (2020).
27. P. Minnmann, L. Quillman, S. Burkhardt, F. H. Richter, and J. Janek, *J. Electrochem. Soc.*, **168**, 040537 (2021).
28. M. B. Dixit, A. Parejiya, N. Muralidharan, R. Essehli, R. Amin, and I. Belharouak, *Energy Storage Mater*, **40**, 239 (2021).
29. Y. G. Lee et al., *Nat. Energy*, **5**, 299 (2020).
30. L. Froboese, J. F. van der Sichel, T. Loellhoeffel, L. Helmers, and A. Kwade, *J. Electrochem. Soc.*, **166**, A318 (2019).
31. K. H. Chen et al., *J. Power Sources*, **471**, 228475 (2020).
32. M. Bolsinger, M. Weller, S. Ruck, P. Kaya, H. Riegel, and V. Knoblauch, *Electrochim. Acta*, **330**, 135163 (2020).
33. C. J. Bae, C. K. Erdonmez, J. W. Halloran, and Y. M. Chiang, *Adv. Mater.*, **25**, 1254 (2013).
34. Y. M. Chiang, C. J. Bae, J. W. Halloran, Q. Fu, A. P. Tomsia, and C. K. Erdonmez, *Controlled porosity in electrodes Patent US10164242B2* (2018).
35. V. Wood, M. Otto, and J. Ebner, *Method for the production of electrodes and electrodes made using such a method Patent WO 2014/170024 A1* (2014).
36. J. Billaud, F. Bouville, T. Magrini, C. Villevieille, and A. R. Studart, *Nat. Energy*, **1**, 16097 (2016).
37. M. Finsterbusch, T. Danner, C. L. Tsai, S. Uhlenbruck, A. Latz, and O. Guillon, *ACS Appl. Mater. Interfaces*, **10**, 22329 (2018).
38. A. Neumann, S. Randau, K. Becker-Steinberger, T. Danner, S. Hein, Z. Ning, J. Marrow, F. H. Richter, J. Janek, and A. Latz, *ACS Appl. Mater. Interfaces*, **12**, 9277 (2020).
39. N. de Klerk and M. Wagemaker, *ACS Appl. Energy Mater*, **1**, 5609 (2018).
40. R. Amin and Y. M. Chiang, *J. Electrochem. Soc.*, **163**, A1512 (2016).
41. A. M. Colclasure and R. J. Kee, *Electrochim. Acta*, **55**, 8960 (2010).
42. M. Schönleber, C. Uhlmann, P. Braun, A. Weber, and E. Ivers-Tiffée, *Electrochim. Acta*, **243**, 250 (2017).
43. M. Weiss et al., *Adv. Energy Mater*, **11**, 2101126 (2021).
44. J. Park, K. T. Kim, D. Y. Oh, D. Jin, D. Kim, Y. S. Jung, and Y. M. Lee, *Adv. Energy Mater*, **10**, 2001563 (2020).
45. Math2Market GmbH, Kaiserslautern, Germany 2019 GeoDict - The digital material laboratory, Version 2019 SP 2.
46. Comsol AB 2019 Comsol Multiphysics 5.4.
47. G. Conforto, R. Ruess, D. Schröder, E. Trevisanello, R. Fantin, F. H. Richter, and J. Janek, *J. Electrochem. Soc.*, **168**, 070546 (2021).
48. K. Märker, P. J. Reeves, C. Xu, K. J. Griffith, and C. P. Grey, *Chem. Mater.*, **31**, 2545 (2019).
49. N. Lin, X. Xie, R. Schenkendorf, and U. Krewer, *J. Electrochem. Soc.*, **165**, A1169 (2018).
50. P. Braun, C. Uhlmann, M. Weiss, A. Weber, and E. Ivers-Tiffée, *J. Power Sources*, **393**, 119 (2018).
51. T. Danner, M. Singh, S. Hein, J. Kaiser, H. Hahn, and A. Latz, *J. Power Sources*, **334**, 191 (2016).
52. P. Arora, M. Doyle, S. A. Gozdz, E. R. White, and J. Newman, *J. Power Sources*, **88**, 219 (2000).
53. A. Falconi, *Electrochemical Li-Ion Battery Modeling for Electric Vehicles Thesis*, Communauté Université Grenoble Alpes (2017).
54. A. Van der Ven, J. Bhattacharya, and A. A. Belak, *Acc. Chem. Res.*, **46**, 1216 (2013).
55. J. Li, L. E. Downie, L. Ma, W. Qiu, and J. R. Dahn, *J. Electrochem. Soc.*, **162**, A1401 (2015).
56. D. Hlushkou, A. E. Reising, N. Kaiser, S. Spannenberger, S. Schlabach, Y. Kato, B. Roling, and U. Tallarek, *J. Power Sources*, **396**, 363 (2018).
57. T. Ates, M. Keller, J. Kulisch, T. Adermann, and S. Passerini, *Energy Storage Mater*, **17**, 204 (2019).
58. D. H. Kim, D. Y. Oh, K. H. Park, Y. E. Choi, Y. J. Nam, H. A. Lee, S. M. Lee, and Y. S. Jung, *Nano Lett.*, **17**, 3013 (2017).
59. H. Giesche, *Part. Part. Syst. Char*, **23**, 9 (2006).
60. W. Pfleging, *Int. J. Extrem. Manuf*, **3**, 012002 (2021).
61. E. Mottay, X. Liu, H. Zhang, E. Mazur, R. Sanatinia, and W. Pfleging, *MRS Bull.*, **41**, 984 (2016).
62. Y. Y. He, C. Q. Zhu, K. H. Hu, K. Zhou, Y. Qing, X. L. Yan, Y. Liu, E. Q. Yang, C. M. Yang, and N. C. Chen, *Ionics*, **25**, 5277 (2019).
63. Z. Yang, J. Lu, D. Bian, W. Zhang, X. Yang, J. Xia, G. Chen, H. Gu, and G. Ma, *J. Power Sources*, **272**, 144 (2014).
64. J. Y. Kim, J. Park, M. J. Lee, S. H. Kang, D. O. Shin, J. Oh, J. Kim, K. M. Kim, Y. G. Lee, and Y. M. Lee, *ACS Energy Lett*, **5**, 2995–3004 (2020).
65. J. Y. Kim, S. Jung, S. H. Kang, J. Park, M. J. Lee, D. Jin, D. O. Shin, Y. G. Lee, and Y. M. Lee, *Adv. Energy Mater*, **12**, 2103108 (2021).
66. J. Y. Kim et al., *Energy Storage Mater*, **41**, 289 (2021).
67. A. Jain et al., *APL Mater.*, **1**, 011002 (2013).

4. Conclusions and Outlook

This thesis examined various aspects of cathodes for ASSBs from the perspective of models and simulations, exposing the trade-offs in the electrode design and several challenges that remain to be solved for ASSBs. The simulation models range from basic conduction network identification, via flux-based stationary simulations to an electrochemical cell charge simulation, all in the context of the cathode microstructure.

Despite their diversity in the model approach, the complexity and the implementation, all publications in this thesis conclude one aspect in unison: *The microstructure counts.* From the void size, distribution and volume fraction to the electrode composition in general, the microstructure that had already been identified as an important influence in conventional LIBs is decisive for the performance in ASSBs.
Concerning the ability to wet and infiltrate pores, the SEs are at a clear disadvantage compared to liquid electrolytes. Therefore, in ASSBs, voids persist after the electrode production and negatively affect the conduction paths and their efficiency. In cells that feature a high CAM fraction for elevated cell capacity, the presence of voids is equivalent to a reduction of the available space for the solid ion conductor. Apart, the voids cover AM surfaces which would otherwise be available for lithium ion (de-)intercalation. A similar effect of active interface and ion pathway blocking can be observed upon the addition of binders in the electrode.
The trade-off between high energy and high power electrode layouts that is known from conventional LIBs is also present in ASSBs: On the one hand high CAM fractions imply an increased cathode loading and facilitate electron transport, potentially making carbon additives redundant in NCM-containing composites. On the other hand, the CAM particles are obstacles for the ions and elevated CAM fractions make their paths more tortuous.
Notwithstanding its flaws in comprehensively describing the cathode microstructure, the tortuosity has shown to be a practical property to broadly assess the conduction efficiency. However, the commonly used Bruggeman relation and even its modifications are not suitable for ASSBs cathodes and should be used cautiously, if at all.
Because the first two publications are comparably simple in their assumptions, the conclusions that can be drawn are broadly applicable and provide guidelines for the electrode layout. The third publication is rather specific in its outcome and demonstrates the criticality of the interface of simulations and experiments. The simulation relies heavily on the experimental input, namely the state-of-charge (SOC)-dependence of $\tilde{D}_{\mathrm{Li}}$ and j_0 and the particle size distribution of the CAM.

There are several ideas for future work that evolve from this thesis.

(i) *Develop elaborate manufacturing techniques for ASSB cathodes.*
It cannot be emphasized enough: The microstructure counts. And because the manufacturing technique has a direct impact on the electrode microstructure, this is an important aspect: Voids and binders both crucially affect the electrode performance, so their content in the composite has to be reduced. There are first bright spots in this field with the warm isostatic pressing[105] and the dry-film processing with 0.1 wt% polytetrafluoroethylene (PTFE),[106] both for NCM955-LPSCl composites or the removal of polypropylene carbonate (PPC)-based binder by heat treatment from NCM111-Li_2S-P_2S_5 composites.[107] Still, there is a lot to do in this field and the reduction of voids and binders are not the only aspect that can be addressed by processing techniques.
A homogeneous distribution of all electrode components is essential for the percolation as well as for a uniform current distribution in the composite which is also reflected in the effective conductivities.[20] Even if voids persist in the electrode, they are less likely to evoke significant overpotentials, if they are well distributed and, accordingly, small in size.[27]
Apart from these basic issues, the (micro-)structuring of ASSB cathodes is a way to go. From the estimation of the applicable current densities in the second publication it is evident that the tortuosity limits the electrode performance, particularly for thick electrodes and low- to medium-conductive SEs. To overcome tortuosity issues I suggest to structure the cathode in express lanes for electrons and lithium ions, while maintaining a sufficient active surface area. One idea is to produce a thick and dense SE layer that is then perforated by a laser. The resulting channels would have to be infiltrated by CAM. As shown in the third publication, these channels should not be wider than 5 μm. Another way is to grow single-crystal CAM structures on the current collector and to infiltrate the SE afterwards which leads over to the next aspect.

(ii) *Use single-crystal CAMs.*
For conventional LIBs, the use of secondary NCM particles with typical particle sizes between 3 and 15 μm[69,108] is the best practice. However, this cannot be said about ASSBs: The conventional particle sizes are too large for the ASSB composites. The percolation analysis indicates that small CAM particles are favorable for the electronic percolation, especially when intending to dispense with conductive carbons. In the charge simulation, the comparison of CAM particle size distributions exposes the beneficial kinetics in small CAM particles, because these entail shorter diffusion paths. Reduced particle sizes also promote a homogeneous particle distribution in the electrode and finally, single-crystals comply better with the mechanical conditions in ASSB cathodes: When the c-lattice of the NCM contracts upon advanced delithiation, the single crystals are less likely to crack than secondary particles and occurring mechanical stresses will be more evenly distributed in the electrode.

Single-crystal NCMs have already shown[109–111] to perform well in ASSBs and I am convinced that this development will proceed.

(iii) *Clear blind spots in modeling.*
As pointed out in section 2.2.2, the extent to which ASSBs are studied in simulations is moderate and that, for sure, is not the result of too few questions. Further studies of the CAM/SE/void-interface that account for the morphology of the SE could advance the insight to this interface. Coupling an electrochemical charge/discharge model as the one in the third publication to a mechanical model is of interest to understand the local stresses that arise due to the volume changes of the CAM upon cycling.
Overall, mechanical models are rare, but they are needed to proceed towards the integration of ASSBs in electric vehicles. Therein the construction of the surrounding component parts requires a sophisticated understanding of the cell (and cell pack) behavior.
Also, degradation, both electrochemical and (chemo-)mechanical, will be a major upcoming topic, once ASSBs become more mature and advance toward practical application.
The latter aspects are difficult to couple to microstructure-resolved models at a manageable computational cost and, as described at length before, infinitely increasing the model complexity cannot be the answer. An extended effective representation of the electrode microstructure, similar to the crux of the Newman model, might be feasible. A way to go could be to study the evolution of the porosity, tortuosity and specific surface area upon cycling in order to implement these in a modified Newman model. But these studies also require an experimental basis that is rock-solid, which leads to the final aspect:

(iv) *Measure and use reliable input parameter sets for simulations.*
One example for a vital input parameter is the diffusion coefficient of lithium in the CAM, whose SOC-dependence is significant, but still widely neglected in simulations. I know how tempting it is to rely on parameter sets that can be extracted from literature, because they are easy to obtain. My work is not completely free of these parameters either, but is it essential to look into their origin and reflect upon the ramifications that these sets imply.
I am convinced that reliable input parameters are essential for the simulation outcome and I encourage to either measure them directly or get into contact with people who are capable to measure them for the desired material combination.
Apart from the specific parameter set that one gets from these cooperations, the interaction with specialists for experiments and measuring techniques is likely to widen the horizon of everyone involved. Communication is the key.
Altogether, I recommend to abide by the agenda on how to build useful models that was originally proposed by Berro [30] and modified in this thesis.

I want to close the thesis with a joke about modeling:

> A group of farmers desperately trying to increase their cows' milk production calls a theorist to help them find a solution. After a few months of hard work, the theorist calls back: "I found the optimal solution. Consider a spherical cow in a vacuum ..."[30]

Bibliography

(1) Masson-Delmotte, V.; Zhai, P.; Pirani, A.; Connors, S.; Péan, C.; Berger, S.; Caud, N.; Chen, Y.; Goldfarb, L.; Gomis, M.; Huang, M.; Leitzell, K.; Lonnoy, E.; Matthews, J. B. R.; Maycock, T. K.; Waterfield, T.; Yelekçi, O.; Yu, R. In *Climate Change 2021: The Physical Science Basis. Contribution of Working Group I to the Sixth Assessment Report of the Intergovernmental Panel on Climate Change*, Zhou, B., Ed.; Cambridge University Press. In Press: 2021; Chapter Summary for Policymakers.

(2) Bieker, G. A Global Comparison of the Life-Cycle Greenhouse Gas Emissions of Combustion Engine and Electric Passenger Cars, `https://theicct.org/publications/global-LCA-passenger-cars-jul2021`, White Paper at The International Council on Clean Transportation, 2021.

(3) United Nations/ Framework Convention on Climate Change Adoption of the Paris Agreement, `https://unfccc.int/sites/default/files/english_paris_agreement.pdf`, 2015.

(4) Pasta, M.; Armstrong, D.; Brown, Z. L.; Bu, J.; Castell, M. R.; Chen, P.; Cocks, A.; Corr, S. A.; Cussen, E. J.; Darnbrough, E.; Deshpande, V.; Doerrer, C.; Dyer, M. S.; El-Shinawi, H.; Fleck, N.; Grant, P.; Gregory, G. L.; Grovenor, C.; Hardwick, L. J.; Irvine, J. T. S.; Lee, H. J.; Li, G.; Liberti, E.; McClelland, I.; Monroe, C.; Nellist, P. D.; Shearing, P. R.; Shoko, E.; Song, W.; Jolly, D. S.; Thomas, C. I.; Turrell, S. J.; Vestli, M.; Williams, C. K.; Zhou, Y.; Bruce, P. G. 2020 Roadmap on Solid-State Batteries. *J. Phys. Energy* **2020**, *2*, 032008, DOI: `10.1088/2515-7655/ab95f4`.

(5) Sen, S.; Trevisanello, E.; Niemöller, E.; Shi, B.-X.; Simon, F. J.; Richter, F. H. The Role of Polymers in Lithium Solid-State Batteries with Inorganic Solid Electrolytes. *J. Mater. Chem. A* **2021**, DOI: `10.1039/D1TA02796D`.

(6) Adeli, P.; Bazak, J. D.; Park, K. H.; Kochetkov, I.; Huq, A.; Goward, G. R.; Nazar, L. F. Boosting Solid-State Diffusivity and Conductivity in Lithium Superionic Argyrodites by Halide Substitution. *Angew. Chem. - Int. Ed.* **2019**, *58*, 8681–8686, DOI: `10.1002/anie.201814222`.

(7) Kato, Y.; Hori, S.; Saito, T.; Suzuki, K.; Hirayama, M.; Mitsui, A.; Yonemura, M.; Iba, H.; Kanno, R. High-power All-Solid-State Batteries using Sulfide Superionic Conductors. *Nat. Energy* **2016**, *1*, 16030, DOI: `10.1038/nenergy.2016.30`.

(8) Asenbauer, J.; Eisenmann, T.; Kuenzel, M.; Kazzazi, A.; Chen, Z.; Bresser, D. The Success Story of Graphite as a Lithium-Ion Anode Material - Fundamentals, Remaining Challenges, and Recent Developments Including Silicon (Oxide) Composites. *Sustain. Energy Fuels* **2020**, *4*, 5387–5416, DOI: 10.1039/D0SE00175A.

(9) Janek, J.; Zeier, W. G. A Solid Future for Battery Development. *Nat. Energy* **2016**, *1*, 16141, DOI: 10.1038/nenergy.2016.141.

(10) Wang, C.; Li, X.; Zhao, Y.; Banis, M. N.; Liang, J.; Li, X.; Sun, Y.; Adair, K. R.; Sun, Q.; Liu, Y.; Zhao, F.; Deng, S.; Lin, X.; Li, R.; Hu, Y.; Sham, T.-K.; Huang, H.; Zhang, L.; Yang, R.; Lu, S.; Sun, X. Manipulating Interfacial Nanostructure to Achieve High-Performance All-Solid-State Lithium-Ion Batteries. *Small Methods* **2019**, *3*, 1900261, DOI: 10.1002/smtd.201900261.

(11) Hatzell, K. B.; Chen, X. C.; Cobb, C. L.; Dasgupta, N. P.; Dixit, M. B.; Marbella, L. E.; McDowell, M. T.; Mukherjee, P. P.; Verma, A.; Viswanathan, V.; Westover, A. S.; Zeier, W. G. Challenges in Lithium Metal Anodes for Solid-State Batteries. *ACS Energy Lett.* **2020**, *5*, 922–934, DOI: 10.1021/acsenergylett.9b02668.

(12) Krauskopf, T.; Richter, F. H.; Zeier, W. G.; Janek, J. Physicochemical Concepts of the Lithium Metal Anode in Solid-State Batteries. *Chem. Rev.* **2020**, *120*, 7745–7794, DOI: 10.1021/acs.chemrev.0c00431.

(13) Kato, Y.; Shiotani, S.; Morita, K.; Suzuki, K.; Hirayama, M.; Kanno, R. All-Solid-State Batteries with Thick Electrode Configurations. *J. Phys. Chem. Lett.* **2018**, *9*, 607–613, DOI: 10.1021/acs.jpclett.7b02880.

(14) Singh, M.; Kaiser, J.; Hahn, H. Thick Electrodes for High Energy Lithium Ion Batteries. *J. Electrochem. Soc.* **2015**, *162*, A1196–A1201, DOI: 10.1149/2.0401507jes.

(15) Landesfeind, J.; Gasteiger, H. A. Temperature and Concentration Dependence of the Ionic Transport Properties of Lithium-Ion Battery Electrolytes. *J. Electrochem. Soc.* **2019**, *166*, A3079–A3097, DOI: 10.1149/2.0571912jes.

(16) Gallagher, K. G.; Trask, S. E.; Bauer, C.; Woehrle, T.; Lux, S. F.; Tschech, M.; Lamp, P.; Polzin, B. J.; Ha, S.; Long, B.; Wu, Q.; Lu, W.; Dees, D. W.; Jansen, A. N. Optimizing Areal Capacities through Understanding the Limitations of Lithium-Ion Electrodes. *J. Electrochem. Soc.* **2016**, *163*, A138–A149, DOI: 10.1149/2.0321602jes.

(17) Walther, F.; Koerver, R.; Fuchs, T.; Ohno, S.; Sann, J.; Rohnke, M.; Zeier, W. G.; Janek, J. Visualization of the Interfacial Decomposition of Composite Cathodes in Argyrodite-Based All-Solid-State Batteries Using Time-of-Flight Secondary-Ion Mass Spectrometry. *Chem. Mater.* **2019**, *31*, 3745–3755, DOI: 10.1021/acs.chemmater.9b00770.

(18) Walther, F.; Randau, S.; Schneider, Y.; Sann, J.; Rohnke, M.; Richter, F. H.; Zeier, W. G.; Janek, J. Influence of Carbon Additives on the Decomposition Pathways in Cathodes of Lithium Thiophosphate-Based All-Solid-State Batteries. *Chem. Mater.* **2020**, *32*, 6123–6136, DOI: 10.1021/acs.chemmater.0c01825.

(19) Koerver, R.; Aygün, I.; Leichtweiß, T.; Dietrich, C.; Zhang, W.; Binder, J. O.; Hartmann, P.; Zeier, W. G.; Janek, J. Capacity Fade in Solid-State Batteries: Interphase Formation and Chemomechanical Processes in Nickel-Rich Layered Oxide Cathodes and Lithium Thiophosphate Solid Electrolytes. *Chem. Mater.* **2017**, *29*, 5574–5582, DOI: 10.1021/acs.chemmater.7b00931.

(20) Minnmann, P.; Quillman, L.; Burkhardt, S.; Richter, F. H.; Janek, J. Editors' Choice–Quantifying the Impact of Charge Transport Bottlenecks in Composite Cathodes of All-Solid-State Batteries. *J. Electrochem. Soc.* **2021**, *168*, 040537, DOI: 10.1149/1945-7111/abf8d7.

(21) Bielefeld, A.; Weber, D. A.; Janek, J. Microstructural Modeling of Composite Cathodes for All-Solid-State Batteries. *J. Phys. Chem. C* **2019**, *123*, 1626–1634, DOI: 10.1021/acs.jpcc.8b11043.

(22) Hlushkou, D.; Reising, A. E.; Kaiser, N.; Spannenberger, S.; Schlabach, S.; Kato, Y.; Roling, B.; Tallarek, U. The Influence of Void Space on Ion Transport in a Composite Cathode for All-Solid-State Batteries. *J. Power Sources* **2018**, *396*, 363–370, DOI: 10.1016/j.jpowsour.2018.06.041.

(23) Ruess, R.; Schweidler, S.; Hemmelmann, H.; Conforto, G.; Bielefeld, A.; Weber, D. A.; Sann, J.; Elm, M. T.; Janek, J. Influence of NCM Particle Cracking on Kinetics of Lithium-Ion Batteries with Liquid or Solid Electrolyte. *J. Electrochem. Soc.* **2020**, *167*, 100532.

(24) Bielefeld, A.; Weber, D. A.; Janek, J. Modeling Effective Ionic Conductivity and Binder Influence in Composite Cathodes for All-Solid-State Batteries. *ACS Appl. Mater. Interfaces* **2020**, *12*, 12821–12833, DOI: 10.1021/acsami.9b22788.

(25) Shi, T.; Tu, Q.; Tian, Y.; Xiao, Y.; Miara, L. J.; Kononova, O.; Ceder, G. High Active Material Loading in All-Solid-State Battery Electrode via Particle Size Optimization. *Adv. Energy Mater.* **2020**, *10*, 1902881, DOI: 10.1002/aenm.201902881.

(26) Randau, S.; Walther, F.; Neumann, A.; Schneider, Y.; Negi, R. S.; Mogwitz, B.; Sann, J.; Becker-Steinberger, K.; Danner, T.; Hein, S.; Latz, A.; Richter, F. H.; Janek, J. On the Additive Microstructure in Composite Cathodes and Alumina-Coated Carbon Microwires for Improved All-Solid-State Batteries. *Chem. Mater.* **2021**, *33*, 1380–1393, DOI: 10.1021/acs.chemmater.0c04454.

(27) Bielefeld, A.; Weber, D. A.; Ruess, R.; Glavas, V.; Janek, J. Influence of Lithium Ion Kinetics, Particle Morphology and Voids on the Electrochemical Performance of Composite Cathodes for All-Solid-State Batteries. *J. Electrochem. Soc.* **2022**, *169*, 020539, DOI: 10.1149/1945-7111/ac50df.

(28) Conforto, G.; Ruess, R.; Schröder, D.; Trevisanello, E.; Fantin, R.; Richter, F. H.; Janek, J. Editors' Choice–Quantification of the Impact of Chemo-Mechanical Degradation on the Performance and Cycling Stability of NCM-Based Cathodes in Solid-State Li-Ion Batteries. *J. Electrochem. Soc.* **2021**, *168*, 070546, DOI: 10.1149/1945-7111/ac13d2.

(29) Trevisanello, E.; Ruess, R.; Conforto, G.; Richter, F. H.; Janek, J. Polycrystalline and Single Crystalline NCM Cathode Materials–Quantifying Particle Cracking, Active Surface Area, and Lithium Diffusion. *Adv. Energy Mater.* **2021**, *11*, 2003400, DOI: 10.1002/aenm.202003400.

(30) Berro, J. "Essentially, all Models are Wrong, but Some are Useful"–A Cross-Disciplinary Agenda for Building useful Models in Cell Biology and Biophysics. *Biophys. Rev.* **2018**, *10*, 1637–1647, DOI: 10.1007/s12551-018-0478-4.

(31) Albertus, P.; Anandan, V.; Ban, C.; Balsara, N.; Belharouak, I.; Buettner-Garrett, J.; Chen, Z.; Daniel, C.; Doeff, M.; Dudney, N. J.; Dunn, B.; Harris, S. J.; Herle, S.; Herbert, E.; Kalnaus, S.; Libera, J. A.; Lu, D.; Martin, S.; McCloskey, B. D.; McDowell, M. T.; Meng, Y. S.; Nanda, J.; Sakamoto, J.; Self, E. C.; Tepavcevic, S.; Wachsman, E.; Wang, C.; Westover, A. S.; Xiao, J.; Yersak, T. Challenges for and Pathways toward Li-Metal-Based All-Solid-State Batteries. *ACS Energy Lett.* **2021**, *6*, 1399–1404, DOI: 10.1021/acsenergylett.1c00445.

(32) Box, G. E. P. In *Robustness in Statistics*, Launer, R. L., Wilkinson, G. N., Eds.; Academic Press: 1979, pp 201–236, DOI: 10.1016/B978-0-12-438150-6.50018-2.

(33) Von Neumann, J. In, Bródy F Vámos, T., Ed.; World Scientific Series In 20th Century Mathematics; World Scientific: 1995; Chapter Method in the Physical Sciences, pp 627–635.

(34) Truran, P. In *Practical Applications of the Philosophy of Science: Thinking about Research*; Springer International Publishing: Heidelberg, 2013, pp 61–67, DOI: 10.1007/978-3-319-00452-5_10.

(35) Comsol The Finite Element Method (FEM), https://www.comsol.com/multiphysics/finite-element-method, 2016.

(36) Winsberg, E., *Science in the Age of Computer Simulation*; University of Chicago Press: Chicago, United States, 2010.

(37) Möbius, W.; Laan, L. Physical and Mathematical Modeling in Experimental Papers. *Cell* **2015**, *163*, 1577–1583, DOI: 10.1016/j.cell.2015.12.006.

(38) Finsterbusch, M.; Danner, T.; Tsai, C.-L.; Uhlenbruck, S.; Latz, A.; Guillon, O. High Capacity Garnet-Based All-Solid-State Lithium Batteries: Fabrication and 3D-Microstructure Resolved Modeling. *ACS Appl. Mater. Interfaces* **2018**, *10*, 22329–22339, DOI: 10.1021/acsami.8b06705.

(39) Zhang, W.; Leichtweiß, T.; Culver, S. P.; Koerver, R.; Das, D.; Weber, D. A.; Zeier, W. G.; Janek, J. The Detrimental Effects of Carbon Additives in $Li_{10}GeP_2S_{12}$-Based Solid-State Batteries. *ACS Appl. Mater. Interfaces* **2017**, *9*, 35888–35896, DOI: 10.1021/acsami.7b11530.

(40) Riesch, H. Simple or Simplistic? Scientists' Views on Occam's Razor. *THEORIA. An International Journal for Theory, History and Foundations of Science* **2010**, *25*, 75–90.

(41) Dyson, F. A Meeting with Enrico Fermi. *Nature* **2004**, *427*, 297–297, DOI: 10.1038/427297a.

(42) Amin, R.; Chiang, Y.-M. Characterization of Electronic and Ionic Transport in $Li_{1-x}Ni_{0.33}Mn_{0.33}Co_{0.33}O_2$ (NMC333) and $Li_{1-x}Ni_{0.50}Mn_{0.20}Co_{0.30}O_2$ (NMC523) as a Function of Li Content. *J. Electrochem. Soc.* **2016**, *163*, A1512–A1517, DOI: 10.1149/2.0131608jes.

(43) Hoshen, J.; Kopelman, R. Percolation and Cluster Distribution. I. Cluster Multiple Labeling Technique and Critical Concentration Algorithm. *Phys. Rev. B* **1976**, *14*, 3438–3445, DOI: 10.1103/PhysRevB.14.3438.

(44) MATLAB, *R2016a (9.0.1)*; The MathWorks Inc.: Natick, Massachusetts, 2016.

(45) Trembacki, B. L.; Mistry, A. N.; Noble, D. R.; Ferraro, M. E.; Mukherjee, P. P.; Roberts, S. A. Editors' Choice—Mesoscale Analysis of Conductive Binder Domain Morphology in Lithium-Ion Battery Electrodes. *J. Electrochem. Soc.* **2018**, *165*, E725–E736, DOI: 10.1149/2.0981813jes.

(46) Laue, V.; Röder, F.; Krewer, U. Practical Identifiability of Electrochemical P2D Models for Lithium-Ion Batteries. *J. Appl. Electrochem.* **2021**, *51*, 1253–1265, DOI: 10.1007/s10800-021-01579-5.

(47) Falconi, A. Electrochemical Li-Ion Battery Modeling for Electric Vehicles, Thesis, Communauté Université Grenoble Alpes, 2017.

(48) Ecker, M.; Tran, T. K. D.; Dechent, P.; Käbitz, S.; Warnecke, A.; Sauer, D. U. Parameterization of a Physico-Chemical Model of a Lithium-Ion Battery. *J. Electrochem. Soc.* **2015**, *162*, A1836–A1848, DOI: 10.1149/2.0551509jes.

(49) Torchio, M.; Magni, L.; Gopaluni, R. B.; Braatz, R. D.; Raimondo, D. M. LIONSIMBA: A Matlab Framework Based on a Finite Volume Model Suitable for Li-Ion Battery Design, Simulation, and Control. *J. Electrochem. Soc.* **2016**, *163*, A1192–A1205, DOI: 10.1149/2.0291607jes.

(50) COMSOL AB Comsol Multiphysics 5.4, Stockholm, Sweden, 2019.

(51) Newman, J. FORTRAN Programs for the Simulation of Electrochemical Systems, `http://www.cchem.berkeley.edu/jsngrp/fortran.html`, 1998.

(52) Fröhlich, P., *FEM-Anwendungspraxis: Einstieg in die Finite Elemente Analyse Zweisprachige Ausgabe Deutsch/Englisch*, 1st ed.; Studium Technik, pp. 74; Vieweg+Teubner Verlag: 2005.

(53) Strauss, F.; Bartsch, T.; de Biasi, L.; Kim, A.-Y.; Janek, J.; Hartmann, P.; Brezesinski, T. Impact of Cathode Material Particle Size on the Capacity of Bulk-Type All-Solid-State Batteries. *ACS Energy Lett.* **2018**, *3*, 992–996, DOI: `10.1021/acsenergylett.8b00275`.

(54) Bentovim, L.; Harden, T. T.; DePace, A. H. Transcriptional Precision and Accuracy in Development: From Measurements to Models and Mechanisms. *Development* **2017**, *144*, 3855–3866, DOI: `10.1242/dev.146563`.

(55) Winsberg, E. In *The Stanford Encyclopedia of Philosophy*, Zalta, E. N., Ed.; Metaphysics Research Lab, Stanford University: 2019.

(56) Frigg, R.; Reiss, J. The Philosophy of Simulation: Hot New Issues or Same Old Stew? *Synthese* **2009**, *169*, 593–613, DOI: `10.1007/s11229-008-9438-z`.

(57) Morgan, M. S. Experiments versus Models: New Phenomena, Inference and Surprise. *J. Econ. Methodol.* **2005**, *12*, 317–329, DOI: `10.1080/13501780500086313`.

(58) Doyle, C. M. Design and Simulation of Lithium Rechargeable Batteries, Ph.D. Thesis, Lawrence Berkeley Laboratory. University of California, 1995.

(59) Fuller, T. F.; Doyle, M.; Newman, J. Simulation and Optimization of the Dual Lithium Ion Insertion Cell. *J. Electrochem. Soc.* **1994**, *141*, DOI: `10.1149/1.2054684`.

(60) Ramadesigan, V.; Northrop, P. W. C.; De, S.; Santhanagopalan, S.; Braatz, R. D.; Subramanian, V. R. Modeling and Simulation of Lithium-Ion Batteries from a Systems Engineering Perspective. *J. Electrochem. Soc.* **2012**, *159*, R31–R45, DOI: `10.1149/2.018203jes`.

(61) Erhard, S. Mehrdimensionale Elektrochemisch-Thermische Modellierung von Lithium-Ionen-Batterien, Dissertation, München: Technische Universität München, 2017.

(62) Bruggeman, D. A. G. Berechnung verschiedener physikalischer Konstanten von heterogenen Substanzen. I. Dielektrizitätskonstanten und Leitfähigkeiten der Mischkörper aus isotropen Substanzen. *Ann. Phys. (Berlin)* **1935**, *416*, 636–664, DOI: `10.1002/andp.19354160705`.

(63) Lagadec, M. F.; Zahn, R.; Müller, S.; Wood, V. Topological and Network Analysis of Lithium Ion Battery Components: The Importance of Pore Space Connectivity for Cell Operation. *Energy Environ. Sci.* **2018**, *11*, 3194–3200, DOI: `10.1039/C8EE00875B`.

(64) Nguyen, T.-T.; Demortière, A.; Fleutot, B.; Delobel, B.; Delacourt, C.; Cooper, S. J. The Electrode Tortuosity Factor: Why the Conventional Tortuosity Factor is not Well Suited for Quantifying Transport in Porous Li-ion Battery Electrodes and What to Use Instead. *NPJ Comput. Mater.* **2020**, *6*, 123, DOI: 10.1038/s41524-020-00386-4.

(65) Tjaden, B.; Brett, D. J. L.; Shearing, P. R. Tortuosity in Electrochemical Devices: A Review of Calculation Approaches. *Int. Met. Rev.* **2018**, *63*, 47–67, DOI: 10.1080/09506608.2016.1249995.

(66) Mayilvahanan, K. S.; Hui, Z.; Hu, K.; Kuang, J.; McCarthy, A. H.; Bernard, J.; Wang, L.; Takeuchi, K. J.; Marschilok, A. C.; Takeuchi, E. S.; West, A. C. Quantifying Uncertainty in Tortuosity Estimates for Porous Electrodes. *J. Electrochem. Soc.* **2021**, *168*, 070537, DOI: 10.1149/1945-7111/ac1316.

(67) Landesfeind, J.; Hattendorff, J.; Ehrl, A.; Wall, W. A.; Gasteiger, H. A. Tortuosity Determination of Battery Electrodes and Separators by Impedance Spectroscopy. *J. Electrochem. Soc.* **2016**, *163*, A1373–A1387, DOI: 10.1149/2.1141607jes.

(68) Zhu, G.-L.; Zhao, C.-Z.; Huang, J.-Q.; He, C.; Zhang, J.; Chen, S.; Xu, L.; Yuan, H.; Zhang, Q. Fast Charging Lithium Batteries: Recent Progress and Future Prospects. *Small* **2019**, *15*, 1805389, DOI: 10.1002/smll.201805389.

(69) Li, J.; Li, H.; Stone, W.; Weber, R.; Hy, S.; Dahn, J. R. Synthesis of Single Crystal $LiNi_{0.5}Mn_{0.3}Co_{0.2}O_2$ for Lithium Ion Batteries. *J. Electrochem. Soc.* **2017**, *164*, A3529–A3537, DOI: 10.1149/2.0401714jes.

(70) Xu, Z.; Jiang, Z.; Kuai, C.; Xu, R.; Qin, C.; Zhang, Y.; Rahman, M. M.; Wei, C.; Nordlund, D.; Sun, C.-J.; Xiao, X.; Du, X.-W.; Zhao, K.; Yan, P.; Liu, Y.; Lin, F. Charge Distribution Guided by Grain Crystallographic Orientations in Polycrystalline Battery Materials. *Nat. Commun.* **2020**, *11*, 83, DOI: 10.1038/s41467-019-13884-x.

(71) Sigma Aldrich Safety Data Sheet according to Regulation (EC) No. 1907/2006: Poly(vinylidene fluoride), Version 6.3, accessed 2019-12-02, Taufkirchen, 2018.

(72) Sigma Aldrich Safety Data Sheet according to Regulation (EC) No. 1907/2006: Poly(acrylonitrile-co-butadiene), Version 6.2, accessed 2019-12-02, Taufkirchen, 2018.

(73) Dhakate, S. R.; Mathur, R. B.; Dhami, T. L. Development of Vapor Grown Carbon Fibers (VGCF) Reinforced Carbon/Carbon Composites. *J. Mater. Sci.* **2006**, *41*, 4123–4131, DOI: 10.1007/s10853-006-6320-6.

(74) Schmidt, D.; Kamlah, M.; Knoblauch, V. Highly densified NCM-Cathodes for High Energy Li-Ion Batteries: Microstructural Evolution during Densification and its Influence on the Performance of the Electrodes. *J. Energy Storage* **2018**, *17*, 213–223, DOI: 10.1016/j.est.2018.03.002.

(75) Bolsinger, M.; Weller, M.; Ruck, S.; Kaya, P.; Riegel, H.; Knoblauch, V. Selective Surface Treatment by Means of IR-Laser – A new Approach to Enhance the Rate Capability of Cathodes for Li-ion Batteries. *Electrochim. Acta* **2020**, *330*, 135163, DOI: 10.1016/j.electacta.2019.135163.

(76) Bauer, W.; Nötzel, D.; Wenzel, V.; Nirschl, H. Influence of Dry Mixing and Distribution of Conductive Additives in Cathodes for Lithium Ion Batteries. *J. Power Sources* **2015**, *288*, 359–367, DOI: 10.1016/j.jpowsour.2015.04.081.

(77) Zielke, L.; Hutzenlaub, T.; Wheeler, D. R.; Chao, C.-W.; Manke, I.; Hilger, A.; Paust, N.; Zengerle, R.; Thiele, S. Three-Phase Multiscale Modeling of a $LiCoO_2$ Cathode: Combining the Advantages of FIB-SEM Imaging and X-Ray Tomography. *Adv. Energy Mater.* **2015**, *5*, 1401612, DOI: 10.1002/aenm.201401612.

(78) Daemi, S. R.; Tan, C.; Volkenandt, T.; Cooper, S. J.; Palacios-Padros, A.; Cookson, J.; Brett, D. J. L.; Shearing, P. R. Visualizing the Carbon Binder Phase of Battery Electrodes in Three Dimensions. *ACS Appl. Energy Mater.* **2018**, *1*, 3702–3710, DOI: 10.1021/acsaem.8b00501.

(79) Sakuda, A.; Hayashi, A.; Tatsumisago, M. Sulfide Solid Electrolyte with Favorable Mechanical Property for All-Solid-State Lithium Battery. *Sci. Rep.* **2013**, *3*, 2261, DOI: 10.1038/srep02261.

(80) Deng, Z.; Wang, Z.; Chu, I.-H.; Luo, J.; Ong, S. Elastic Properties of Alkali Superionic Conductor Electrolytes from First Principles Calculations. *J. Electrochem. Soc.* **2016**, *163*, A67–A74, DOI: 10.1149/2.0061602jes.

(81) Kim, D. H.; Oh, D. Y.; Park, K. H.; Choi, Y. E.; Nam, Y. J.; Lee, H. A.; Lee, S.-M.; Jung, Y. S. Infiltration of Solution-Processable Solid Electrolytes into Conventional Li-Ion-Battery Electrodes for All-Solid-State Li-Ion Batteries. *Nano Lett.* **2017**, *17*, 3013–3020, DOI: 10.1021/acs.nanolett.7b00330.

(82) Braun, P.; Uhlmann, C.; Weiss, M.; Weber, A.; Ivers-Tiffée, E. Assessment of All-Solid-State Lithium-Ion Batteries. *J. Power Sources* **2018**, *393*, 119–127, DOI: 10.1016/j.jpowsour.2018.04.111.

(83) Laue, V.; Wolff, N.; Röder, F.; Krewer, U. Modeling the Influence of Mixing Strategies on Microstructural Properties of All-Solid-State Electrodes. *Energy Technol.* **2019**, *8*, 1801049, DOI: 10.1002/ente.201801049.

(84) Sangrós Giménez, C.; Helmers, L.; Schilde, C.; Diener, A.; Kwade, A. Modeling the Electrical Conductive Paths within All-Solid-State Battery Electrodes. *Chem. Eng. Technol.* **2020**, *43*, 819–829, DOI: 10.1002/ceat.201900501.

(85) Park, J.; Kim, K. T.; Oh, D. Y.; Jin, D.; Kim, D.; Jung, Y. S.; Lee, Y. M. Digital Twin-Driven All-Solid-State Battery: Unraveling the Physical and Electrochemical Behaviors. *Adv. Energy Mater.* **2020**, *10*, 2001563, DOI: 10.1002/aenm.202001563.

(86) Neumann, A.; Hamann, T. R.; Danner, T.; Hein, S.; Becker-Steinberger, K.; Wachsman, E.; Latz, A. Effect of the 3D Structure and Grain Boundaries on Lithium Transport in Garnet Solid Electrolytes. *ACS Appl. Energy Mater.* **2021**, *4*, 4786–4804, DOI: 10.1021/acsaem.1c00362.

(87) Neumann, A.; Randau, S.; Becker-Steinberger, K.; Danner, T.; Hein, S.; Ning, Z.; Marrow, J.; Richter, F. H.; Janek, J.; Latz, A. Analysis of Interfacial Effects in All-Solid-State Batteries with Thiophosphate Solid Electrolytes. *ACS Appl. Mater. Interfaces* **2020**, *12*, 9277–9291, DOI: 10.1021/acsami.9b21404.

(88) Becker-Steinberger, K.; Schardt, S.; Horstmann, B.; Latz, A. Statics and Dynamics of Space-Charge-Layers in Polarized Inorganic Solid Electrolytes. *arXiv e-prints* **2021**, https://ui.adsabs.harvard.edu/abs/2021arXiv210110294B.

(89) Swift, M. W.; Swift, J. W.; Qi, Y. Modeling the Electrical Double Layer at Solid-State Electrochemical Interfaces. *Nat. Comput. Sci.* **2021**, *1*, 212–220, DOI: 10.1038/s43588-021-00041-y.

(90) Bistri, D.; Afshar, A.; Leo, C. Modeling the Chemo-Mechanical Behavior of All-Solid-State Batteries: A Review. *Meccanica* **2021**, *56*, 1523–1554, DOI: 10.1007/s11012-020-01209-y.

(91) Dixit, M. B.; Parejiya, A.; Muralidharan, N.; Essehli, R.; Amin, R.; Belharouak, I. Understanding Implications of Cathode Architecture on Energy Density of Solid-State Batteries. *Energy Storage Mater.* **2021**, *40*, 239–249, DOI: 10.1016/j.ensm.2021.05.001.

(92) Yamakawa, S.; Ohta, S.; Kobayashi, T. Effect of Positive Electrode Microstructure in All-Solid-State Lithium-Ion Battery on High-Rate Discharge Capability. *Solid State Ion.* **2020**, *344*, 115079, DOI: 10.1016/j.ssi.2019.115079.

(93) Koerver, R.; Zhang, W.; de Biasi, L.; Schweidler, S.; Kondrakov, A. O.; Kolling, S.; Brezesinski, T.; Hartmann, P.; Zeier, W. G.; Janek, J. Chemo-Mechanical Expansion of Lithium Electrode Materials - On the Route to Mechanically Optimized All-Solid-State Batteries. *Energy Environ. Sci.* **2018**, *11*, 2142–2158, DOI: 10.1039/C8EE00907D.

(94) Nam, Y. J.; Oh, D. Y.; Jung, S. H.; Jung, Y. S. Toward Practical All-Solid-State Lithium-Ion Batteries with High Energy Density and Safety: Comparative Study for Electrodes Fabricated by Dry- and Slurry-Mixing Processes. *J. Power Sources* **2018**, *375*, 93–101, DOI: 10.1016/j.jpowsour.2017.11.031.

(95) Noh, S.; Nichols, W. T.; Park, C.; Shin, D. Enhanced Energy Density and Electrochemical Performance of All-Solid-State Lithium Batteries through Microstructural Distribution of Solid Electrolyte. *Ceram. Int.* **2017**, *43*, 15952–15958, DOI: 10.1016/j.ceramint.2017.08.176.

(96) Zhang, W.; Weber, D. A.; Weigand, H.; Arlt, T.; Manke, I.; Schröder, D.; Koerver, R.; Leichtweiss, T.; Hartmann, P.; Zeier, W. G.; Janek, J. Interfacial Processes and Influence of Composite Cathode Microstructure Controlling the Performance of All-Solid-State Lithium Batteries. *ACS Appl. Mater. Interfaces* **2017**, *9*, 17835–17845, DOI: 10.1021/acsami.7b01137.

(97) Siroma, Z.; Sato, T.; Takeuchi, T.; Nagai, R.; Ota, A.; Ioroi, T. AC Impedance Analysis of Ionic and Electronic Conductivities in Electrode Mixture Layers for an All-Solid-State Lithium-Ion Battery. *J. Power Sources* **2016**, *316*, 215–223, DOI: 10.1016/j.jpowsour.2016.03.059.

(98) Math2Market GmbH, K. G. GeoDict — The Digital Material Laboratory, Version 2018 SP 5, 2018.

(99) Oh, D. Y.; Nam, Y. J.; Park, K. H.; Jung, S. H.; Kim, K. T.; Ha, A. R.; Jung, Y. S. Slurry-Fabricable Li+-Conductive Polymeric Binders for Practical All-Solid-State Lithium-Ion Batteries Enabled by Solvate Ionic Liquids. *Adv. Energy Mater.* **2019**, *9*, 1802927, DOI: 10.1002/aenm.201802927.

(100) Ito, S.; Fujiki, S.; Yamada, T.; Aihara, Y.; Park, Y.; Kim, T. Y.; Baek, S.-W.; Lee, J.-M.; Doo, S.; Machida, N. A Rocking Chair Type All-Solid-State Lithium Ion Battery Adopting Li_2O-ZrO_2 Coated $LiNi_{0.8}Co_{0.15}Al_{0.05}O_2$ and a Sulfide Based Electrolyte. *J. Power Sources* **2014**, *248*, 943–950, DOI: 10.1016/j.jpowsour.2013.10.005.

(101) Inada, T.; Takada, K.; Kajiyama, A.; Kouguchi, M.; Sasaki, H.; Kondo, S.; Watanabe, M.; Murayama, M.; Kanno, R. Fabrications and Properties of Composite Solid-State Electrolytes. *Solid State Ion.* **2003**, *158*, 275–280, DOI: 10.1016/S0167-2738(02)00889-5.

(102) Yu, C.; Ganapathy, S.; van Eck, E. R. H.; van Eijck, L.; Basak, S.; Liu, Y.; Zhang, L.; Zandbergen, H. W.; Wagemaker, M. Revealing the Relation between the Structure, Li-ion Conductivity and Solid-State Battery Performance of the Argyrodite Li_6PS_5Br Solid Electrolyte. *J. Mater. Chem. A* **2017**, *5*, 21178–21188, DOI: 10.1039/C7TA05031C.

(103) Lee, J. M.; Park, Y. S.; Moon, J.-W.; Hwang, H. Ionic and Electronic Conductivities of Lithium Argyrodite Li_6PS_5Cl Electrolytes Prepared via Wet Milling and Post-Annealing. *Front. Chem.* **2021**, *9*, 1023, DOI: 10.3389/fchem.2021.778057.

(104) Math2Market GmbH, K. G. GeoDict — The Digital Material Laboratory, Version 2019 SP 2, 2019.

(105) Lee, Y.-G.; Fujiki, S.; Jung, C.; Suzuki, N.; Yashiro, N.; Omoda, R.; Ko, D.-S.; Shiratsuchi, T.; Sugimoto, T.; Ryu, S.; Ku, J. H.; Watanabe, T.; Park, Y.; Aihara, Y.; Im, D.; Han, I. T. High-Energy Long-Cycling All-Solid-State Lithium Metal Batteries Enabled by Silver–Carbon Composite Anodes. *Nat. Energy* **2020**, *5*, 299–308, DOI: 10.1038/s41560-020-0575-z.

(106) Hippauf, F.; Schumm, B.; Doerfler, S.; Althues, H.; Fujiki, S.; Shiratsushi, T.; Tsujimura, T.; Aihara, Y.; Kaskel, S. Overcoming Binder Limitations of Sheet-Type Solid-State Cathodes using a Solvent-Free Dry-Film Approach. *Energy Storage Mater.* **2019**, *21*, 390–398, DOI: 10.1016/j.ensm.2019.05.033.

(107) Yamamoto, M.; Terauchi, Y.; Sakuda, A.; Takahashi, M. Binder-Free Sheet-Type All-Solid-State Batteries with Enhanced Rate Capabilities and High Energy Densities. *Sci. Rep.* **2018**, *8*, 1212, DOI: 10.1038/s41598-018-19398-8.

(108) Tsai, P.-C.; Wen, B.; Wolfman, M.; Choe, M.-J.; Pan, M. S.; Su, L.; Thornton, K.; Cabana, J.; Chiang, Y.-M. Single-Particle Measurements of Electrochemical Kinetics in NMC and NCA Cathodes for Li-Ion Batteries. *Energy Environ. Sci.* **2018**, *11*, 860–871, DOI: 10.1039/C8EE00001H.

(109) Wang, C.; Fu, K.; Kammampata, S. P.; McOwen, D. W.; Samson, A. J.; Zhang, L.; Hitz, G. T.; Nolan, A. M.; Wachsman, E. D.; Mo, Y.; Thangadurai, V.; Hu, L. Garnet-Type Solid-State Electrolytes: Materials, Interfaces, and Batteries. *Chem. Rev.* **2020**, *120*, 4257–4300, DOI: 10.1021/acs.chemrev.9b00427.

(110) Doerrer, C.; Capone, I.; Narayanan, S.; Liu, J.; Grovenor, C. R. M.; Pasta, M.; Grant, P. S. High Energy Density Single-Crystal NMC/Li_6PS_5Cl Cathodes for All-Solid-State Lithium-Metal Batteries. *ACS Appl. Mater. Interfaces* **2021**, DOI: 10.1021/acsami.1c07952.

(111) Fantin, R.; Trevisanello, E.; Ruess, R.; Pokle, A.; Conforto, G.; Richter, F. H.; Volz, K.; Janek, J. Synthesis and Postprocessing of Single-Crystalline $LiNi_{0.8}Co_{0.15}Al_{0.05}O_2$ for Solid-State Lithium-Ion Batteries with High Capacity and Long Cycling Stability. *Chem. Mater.* **2021**, *33*, 2624–2634, DOI: 10.1021/acs.chemmater.1c00471.

Appendix

This chapter contains the supporting information of the second and third publication as well as an overview of articles, oral and poster presentations and patents.
The supporting information supplement the articles by providing more insight to modeling methods, such as the generation of binder for the second publication or the reconstruction or the import/export of particle-type microstructures from GeoDict to Comsol in the third publication. Also simulation parameters and additional result plots are provided.

A. Supporting Information of Publication 2

Supporting information for: Modeling Effective Ionic Conductivity and Binder Influence in Composite Cathodes for All-Solid-State Batteries

Anja Bielefeld,[*,†,‡] Dominik A. Weber,[‡] and Jürgen Janek[*,†,¶]

†*Physikalisch-Chemisches Institut, Justus-Liebig-Universität, 35392 Giessen, Germany*

‡*Volkswagen AG, Group Innovation, 38436 Wolfsburg, Germany*

¶*Center of Materials Research (LaMa), Justus-Liebig-Universität, 35392 Giessen, Germany*

E-mail: anja.bielefeld@volkswagen.de; juergen.janek@phys.chemie.uni-giessen.de

Supporting Information Available

Binder generation procedure

The GeoDict[S1]-procedure of the binder generation is illustrated in Figure S1, targeting the shape of a concave meniscus in locations where surfaces come close together. This binder distribution is also referred to as a "binder bridge"[S2]. The underlying process consists of three steps which are repeated until the desired binder content is obtained: To reach the desired binder content precisely, the procedure is optimized, such that the outer voxels are dilated and removed. The composition of a microstructure model is exemplarily shown in Figure S2. The first step is called "Dilation" (from section 1) to 2) in Figure S1). Herein, the AM particles are coated (dilated) by a thin binder film. Geometrically, this is equivalent to dilating the AM particle by a given amount of voxels and the resulting coating may overlap in areas where AM particles are close together. In the second step, the binder coating and AM particles can be regarded as one structural agglomerate as a whole ((section 3) in Figure S1). This structure can then, in the third step, be diminished by a given number of voxels. Hence, most of the coating is removed, except for small remains between the AM particles that build the binder bridge ((section 4) in Figure S1). These steps are repeated until the desired binder content is reached. The choice of coating thickness and the amount of voxels removed determines the concrete shape of the binder meniscus. In our work, the

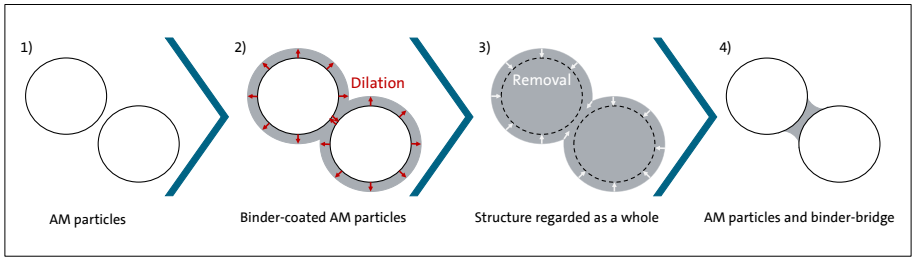

Figure S1: Schematic illustration of the generation of binder (in grey) between solid AM particles

dilation and removal step were done at the same growth/shrinkage rate, which leads to a minimal contact angle between the solid structure and the binder and corresponds to a binder with high wettability.

Figure S2: Schematic illustration of the composition of microstructure models in GeoDict [S1]

Flux-based simulation of effective conductivity

Table S1: Modeling parameters for the calculation of the ionic conductivity

parameter	symbol	value	comment/reference
void space	ϕ	15 %	similar to Hlushkou et al. [S3]
ionic conductivity SE (LPSCl)	$\sigma^{\text{ion}}_{\text{LPSCl}}$	2.7 mS cm^{-1}	Kato et al. [S4]
ionic conductivity AM (NCM532)	$\sigma^{\text{ion}}_{\text{NCM532}}$	10^{-4} mS cm^{-1}	according to Amin and Chiang [S5]
contact resistance AM/SE	$\rho_{\text{AM/SE}}$	40 Ω cm^2	estimated by Braun et al. [S6] from EIS and SEM data of Kato et al. [S4]
potential difference	ΔU	1 V	
resolution		0.2 μm voxel^{-1}	
simulation dimensions	$(l_1 \times l_2 \times l_3)$	(80 x 80 x 140) μm	

Estimation of current densities

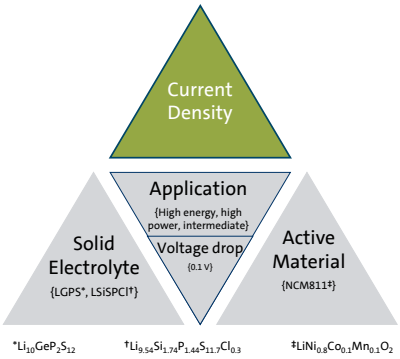

Figure S3: Elements needed for the estimation of current density through a composite cathode: Ionic conduction (linear), material choice, application-driven electrode layout and an assumed voltage drop.

Comparison with the literature

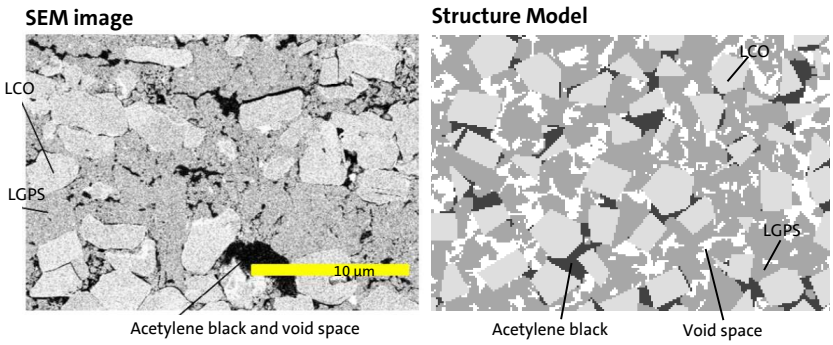

Figure S4: Cross-sectional SEM image (left) adapted with permission from Kato et al.[S7]. Copyright (2018) American Chemical Society. Reconstructed microstructure model (right), based on the modeling parameters in Table S2 featuring 15 % void space.

Table S2: Modeling parameters for the reconstruction of a composite cathode studied by Kato et al.[S7]

description	symbol	value
microstructure dimensions	$(l_1 \times l_2 \times l_3)$	(80 x 80 x 100) μm^3
resolution		0.2 μm voxel^{-1}
void space	ϕ	15 %
shape of LCO particles		planar polyhedra, 5 edges
thickness of LCO particles	l_{AM}	$\mu = 3\ \mu\mathrm{m}, \sigma = 0.5\ \mu\mathrm{m}, l_{\mathrm{AM}} \in [2.3, 3.7]\ \mu\mathrm{m}$
ray length of LCO particles	r_{AM}	$\mu = 2.5\ \mu\mathrm{m}, \sigma = 0.5\ \mu\mathrm{m}, r_{\mathrm{AM}} \in [1.8, 3.2]\ \mu\mathrm{m}$
shape of LGPS particles		convex polyhedra, 7 edges
enclosing diameter of LGPS particles	d_{SE}	$\mu = 4\ \mu\mathrm{m}, \sigma = 1\ \mu\mathrm{m}, d_{\mathrm{SE}} \in [2.8, 5.2]\ \mu\mathrm{m}$
solid volume fraction of AM	ν_{AM}	38.1 %
solid volume fraction of SE	ν_{SE}	57.1 %
solid volume fraction acetylene black	ν_{AB}	4.8 %

Effective conduction

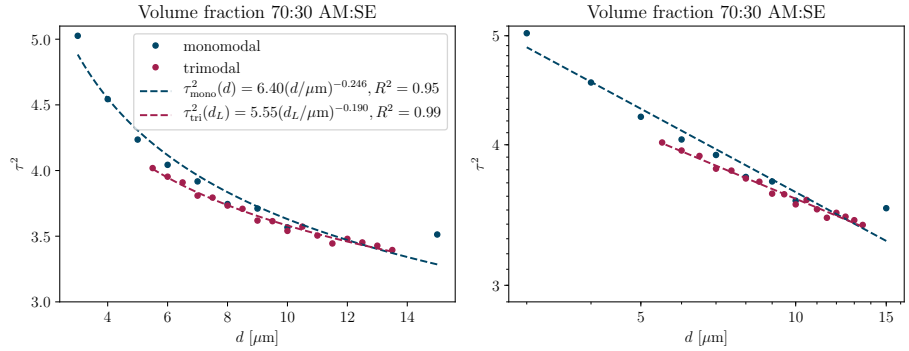

Figure S5: AM particle size dependence of the ionic tortuosity factor of composite microstructures; monomodal AM distribution with $d \in [3, 15]$ μm; trimodal AM distribution with $d_L \in [5.5, 13.5]$ μm, $d_M = 5.5$ μm and $d_S = 3$ μm; electrode void space held constant at $\phi = 15$ %.

References

(S1) Math2Market GmbH, K. G. GeoDict — The Digital Material Laboratory, Version 2019 SP 2. 2019.

(S2) Trembacki, B. L.; Mistry, A. N.; Noble, D. R.; Ferraro, M. E.; Mukherjee, P. P.; Roberts, S. A. Editors' Choice—Mesoscale Analysis of Conductive Binder Domain Morphology in Lithium-Ion Battery Electrodes. *Journal of The Electrochemical Society* **2018**, *165*, E725–E736.

(S3) Hlushkou, D.; Reising, A. E.; Kaiser, N.; Spannenberger, S.; Schlabach, S.; Kato, Y.; Roling, B.; Tallarek, U. The Influence of Void Space on Ion Transport in a Composite Cathode for All-Solid-State Batteries. *Journal of Power Sources* **2018**, *396*, 363–370.

(S4) Kato, Y.; Hori, S.; Saito, T.; Suzuki, K.; Hirayama, M.; Mitsui, A.; Yonemura, M.; Iba, H.; Kanno, R. High-Power All-Solid-State Batteries using Sulfide Superionic Conductors. *Nature Energy* **2016**, *1*, 16030.

(S5) Amin, R.; Chiang, Y.-M. Characterization of Electronic and Ionic Transport in $Li_{1-x}Ni_{0.33}Mn_{0.33}Co_{0.33}O_2$ (NMC333) and $Li_{1-x}Ni_{0.50}Mn_{0.20}Co_{0.30}O_2$ (NMC523) as a Function of Li Content. *Journal of The Electrochemical Society* **2016**, *163*, A1512–A1517.

(S6) Braun, P.; Uhlmann, C.; Weiss, M.; Weber, A.; Ivers-Tiffée, E. Assessment of All-Solid-State Lithium-Ion Batteries. *Journal of Power Sources* **2018**, *393*, 119–127.

(S7) Kato, Y.; Shiotani, S.; Morita, K.; Suzuki, K.; Hirayama, M.; Kanno, R. All-Solid-State Batteries with Thick Electrode Configurations. *The Journal of Physical Chemistry Letters* **2018**, *9*, 607–613.

B. Supporting Information of Publication 3

Supporting Information:

Influence of Lithium Ion Kinetics, Particle Morphology and Voids on the Electrochemical Performance of Composite Cathodes for All-Solid-State Batteries

Anja Bielefeld[1,2], Dominik A. Weber[3], Raffael Rueß[1,2], Vedran Glavas[3] and Jürgen Janek[1,2]

[1] Physikalisch-Chemisches Institut, Justus-Liebig-Universität, 35392 Giessen, Germany
[2] Center of Materials Research (LaMa), Justus-Liebig-Universität, 35392 Giessen, Germany
[3] Volkswagen AG, 38440 Wolfsburg, Germany

E-mail: anja.bielefeld@phys.chemie.uni-giessen.de, juergen.janek@phys.chemie.uni-giessen.de

SI: Electrochemical Performance of Composite Cathodes for ASSBs S-1

Model

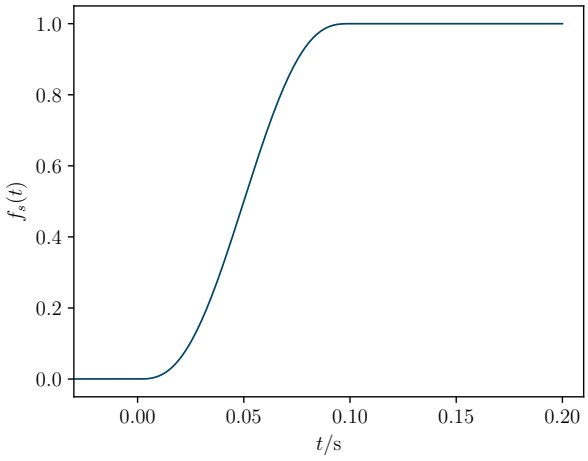

Figure S1. Smooth step function for the applied external current density.

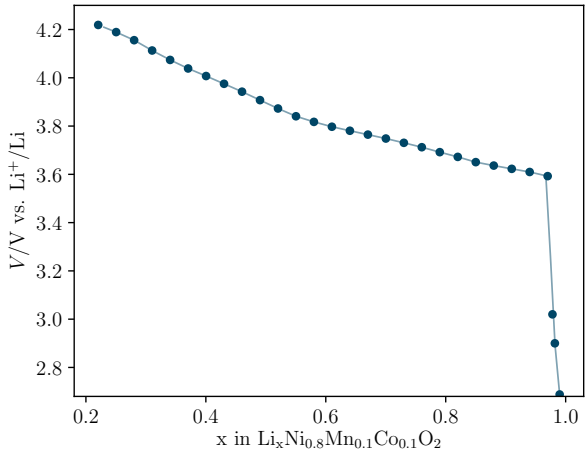

Figure S2. Open circuit voltage of NCM811.

Table S1. Overview of the variables, parameters and constants for the electrochemical simulation mentioned in figure S3.

Variable/ Parameter/ Constant	Description	Unit
c_{Li}	lithium ion concentration in CAM	molm^{-3}
$\vec{J}_{\mathrm{Li}}$	molar lithium flux in CAM	$\mathrm{molm}^{-2}\mathrm{s}^{-1}$
R_{I}	molar volume reaction rate for (de-)intercalation in CAM	$\mathrm{molm}^{-3}\mathrm{s}^{-1}$
R'_{I}	molar surface reaction rate for (de-)intercalation in CAM	$\mathrm{molm}^{-2}\mathrm{s}^{-1}$
$\vec{j}_{\mathrm{eon}}^{\mathrm{CAM}}$	electronic current density in CAM	Am^{-2}
$\vec{j}^{\mathrm{SE}}$	ionic current density in SE	Am^{-2}
$\vec{j}_{\mathrm{eon}}^{\mathrm{CC}}$	electronic current density in CC	Am^{-2}
$\vec{j}_{\mathrm{BV}}$	current density at CAM/SE-interface	Am^{-2}
$\vec{j}_{\mathrm{BV}}^{a}$	current density at Li/SE-interface	Am^{-2}
η	overpotential at CAM/SE-interface	V
η^{a}	overpotential at Li/SE-interface	V
φ	(Galvani) electric potential	V
T	temperature	K
t	time	s
$\vec{n}$	normal vector	-
$\sigma_{\mathrm{eon}}^{\mathrm{CAM}}$	partial electronic conductivity in CAM	Sm^{-1}
$\sigma_{\mathrm{Li}}^{\mathrm{SE}}$	ionic conductivity in SE	Sm^{-1}
$\sigma_{\mathrm{eon}}^{\mathrm{CC}}$	electronic conductivity in CC	Sm^{-1}
V_0^{NCM811}	open circuit voltage of NCM811 vs. Li^{+}/Li, see figure S2	V
V_0^{Li}	open circuit voltage of lithium	V
$\tilde{D}_{\mathrm{Li}}$	chemical lithium diffusion coefficient in CAM, see figure 7a)	$\mathrm{m}^2\mathrm{s}^{-1}$
j_0	exchange current density at CAM/SE-interface, see figure 7a)	Am^{-2}
j_0^{a}	exchange current density at Li/SE-interface	Am^{-2}
α	symmetry factor for reaction at CAM/SE-interface	-
α^{a}	symmetry factor for reaction at Li/SE-interface	-
j_{ext}	external, applied current density	Am^{-2}
$f_s(t)$	smooth step function, see figure S1	-
F	Faraday constant	Cmol^{-1}
R	universal gas constant	$\mathrm{Jmol}^{-1}\mathrm{K}^{-1}$

Table S2. Parameter values for the electrochemical simulation; the right column indicates with model geometry uses the parameter with a • for the 1-particle model, $*$ referring to the particle-type microstructure geometries and $\odot$ to the cone-type structures.

	Parameter	Value	Description	Comment/ Reference	Models
Anode	j_0^a	3 $\mathrm{Acm^{-2}}$	anode exchange current density, Li/Li_6PS_5Cl-interface	Rueß *et al.* [1]	•, $*$, $\odot$
	α^a	0.5	symmetry factor Li/Li_6PS_5Cl-interface		•, $*$, $\odot$
	V_0^{Li}	0 V	open circuit voltage of lithium		•, $*$, $\odot$
SE	l_{SE}	10 μm	SE-separator thickness		$*$, $\odot$
	$\sigma_{\mathrm{Li}}^{\mathrm{SE}}$	0.7 $\mathrm{mScm^{-1}}$	lithium ion conductivity of Li_6PS_5Cl	Rueß *et al.* [1]	•, $*$, $\odot$
Cathode	l_c	40 μm	cathode thickness		$*$, $\odot$
	j_0	see figure 7a)	cathode exchange current density, $NCM811/Li_6PS_5Cl$-interface	calculated from R_{CT} Rueß *et al.* [1] (equation 12)	•, $*$, $\odot$
	α	0.5	symmetry factor $NCM811/Li_6PS_5Cl$-interface		•, $*$, $\odot$
	V_0^{NCM811}	see figure S2	open circuit voltage of NCM811 vs. Li^+/Li	Rueß *et al.* [1]	•, $*$, $\odot$
	$\tilde{D}_{\mathrm{Li}}$	see figure 7a)	lithium diffusion coefficient in NCM811	Rueß *et al.* [1]	•, $*$, $\odot$
	$c_{\mathrm{spec}}^{\mathrm{NCM811}}$	200 $\mathrm{mAhg^{-1}}$	specific capacity of NCM811	Rueß *et al.* [1]	•, $*$, $\odot$
	ρ^{NCM811}	4.77 $\mathrm{gcm^{-3}}$	gravimetric density of NCM811		•, $*$, $\odot$
	$\sigma_{\mathrm{eon}}^{\mathrm{CAM}}$	100 $\mathrm{Sm^{-1}}$	partial electronic conductivity of NCM811	see assumptions of mathematical model	•, $*$, $\odot$
	$c_{\mathrm{Li,ref}}^{\mathrm{NCM811}}$	49 $\mathrm{moll^{-1}}$	reference concentration of NCM811		•, $*$, $\odot$
CC	$\sigma_{\mathrm{eon}}^{\mathrm{CC}}$	300 $\mathrm{Sm^{-1}}$	electronic conductivity of current collector		•, $*$, $\odot$
Other	T	273.15 K	temperature		•, $*$, $\odot$
	$V_{\max}$	4.2 V	upper cutoff potential vs. Li^+/Li		•, $*$, $\odot$
	$V_{\min}$	3.5 V	lower cutoff potential vs. Li^+/Li		•, $*$, $\odot$
	dt	$0.01/C$ for $V \leq 4.0$ V; $0.001/C$ for $V > 4.0$ V	time stepping (depending on C-rate)		•, $*$, $\odot$

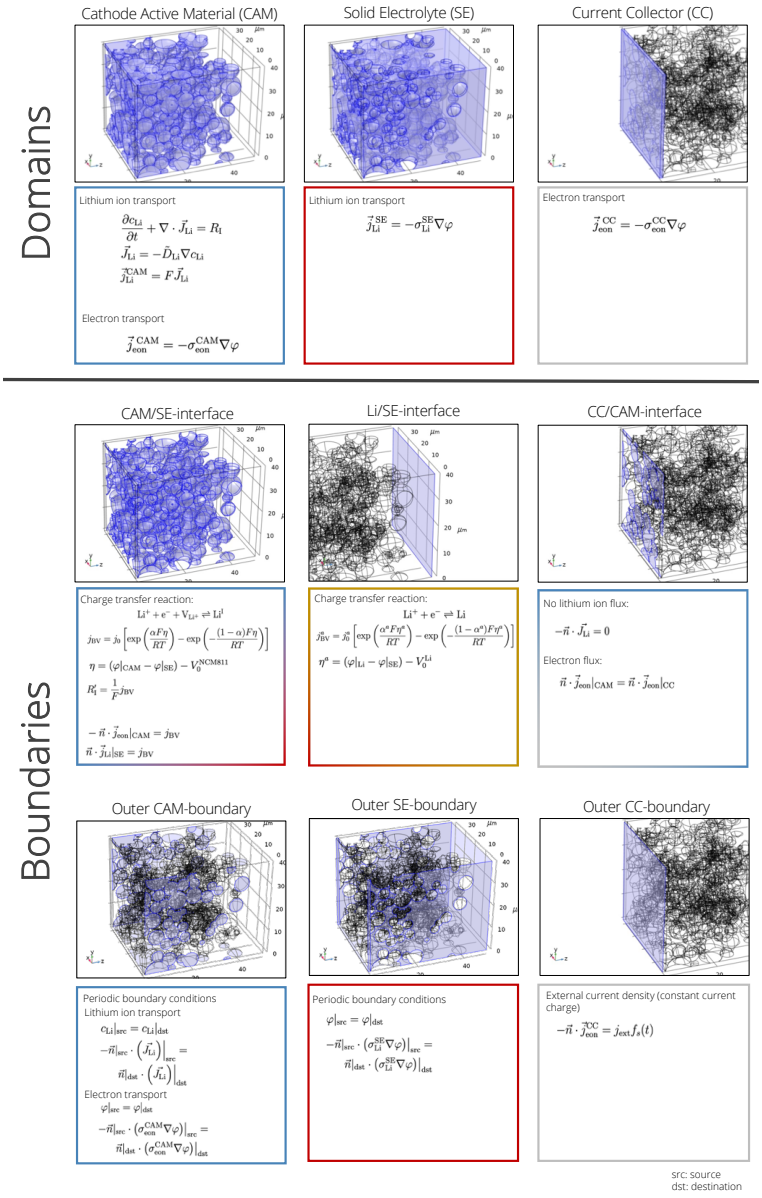

Figure S3. Overview of the mathematical model, its equations and, highlighted in blue, their associated domains and boundaries, respectively. The illustrations are based on the particle-type geometry S-PSD a).

Microstructure Generation

Reconstruction of CAM Particle-Type Microstructures The CAM is constructed to consist of spherical secondary particles, neglecting the impact of crystallite orientation of the primary particles. This impact of crystallographic orientation in polycrystalline NCM can be anticipated from the study of Xu *et al.*[2] As the electrochemical data from Rueß *et al.*[1] does not indicate issues with electronic percolation albeit the absence of carbon black in the composite, the CAM particles have to be well-connected. The weight composition of 70/30 NCM811/Li_6PS_5Cl and 14% of residual void space is equivalent to an overall volume fraction of 42% CAM. According to a percolation study on similar composites, electronic percolation will not be achieved for randomly distributed spherical particles at this volume fraction,[3] so upon microstructure generation in GeoDict electronic percolation is assured by a placeholder "trick", while maintaining the spherical CAM particle shape: Placeholder particles are randomly distributed in the empty volume to block space from CAM placement (figure 1, step 1)). Good interconnection of CAM particles is achieved by overlapping convex polyhedra that fill 40% of the volume (Please refer to table S3 for the detailed parameter selection.). The CAM particles are then randomly distributed in the unoccupied 60%, not in the placeholder-filled volume, with the target to minimize the overlap among the CAM particles and with the placeholder to 3 % (figure 1, step 2)). With this method, we manage to generate microstructured of interconnected and therefore percolating CAM-particles that are intact in shape.

In order to perform the electrochemical simulation in COMSOL Multiphysics,[4] both programs are coupled by their Matlab interfaces: GeoLab for GeoDict and Matlab LiveLink for Comsol. A .gad-file (GeoDict analytic data) is imported to Matlab and all sphere diameters and positions are collected in a variable, which is then used to generate exactly the same spheres in a .mph-file. for Comsol

The particle arrangement is periodic when generated in GeoDict, but each particle is represented once in the .gad-file, no matter if it overlaps with the volume's boundaries. Therefore, the particle arrangement is duplicated in a $(3 \times 3 \times 2)$-array after import to Comsol (figure 1, step 4 and 5)). This way, periodicity in the x- and y-directions can be assured when the simulation volume is cut out of the overall volume by placing a box of SE around it. This box intersects with CAM-particles at the negative z-boundary ensuring contact to the current collector of 1 μm thickness which is attached to this side. The current collector has the effect that is distributes the incoming current uniformly to the connected CAM-particles. At the positive z-boundary, the box does not intersect with the CAM-particles, because its length is chosen to be the cathode thickness plus the separator thickness. The final microstructure ready for simulation is shown in figure 1, step 6). A first charge simulation is used to identify isolated particles which are then moved manually to assure connection of all CAM particles in a percolating network.

Table S3. Geometrical microstructure reconstruction parameters

	Parameter	Symbol	Value	Comment/ Reference
Placeholder	Volume fraction	ν_P	40%	best practice
	Shape		Convex polyhedra	
	Size (enclosing ellipsoid diameters)		$(20 \times 15 \times 10)$ μm	
CAM	Volume fraction	ν_{CAM}	42%	Rueß *et al.*[1]
	Shape		Spheres (secondary particles)	
	Size distribution		PSDs (S, M, L)	Conforto *et al.*[5] (modified, see results section)
	Model volume	$(l_1 \times l_2 \times l_3)$	$(40 \times 40 \times 40)$ μm^3	

1-Particle-Void Microstructures The 1-particle geometry itself is constructed by a spherical CAM particle with particle diameter d_{CAM} that is surrounded by a block of SE (figure 2), not resolving the actual SE-microstructure for technical reasons: The finite element method (FEM) in COMSOL Multiphysics requires a computation mesh on the geometry whose element size would drastically increase when modeling the SE as e.g. convex polyhedra as performed by Bielefeld *et al.*,[3,6] but in a voxel-based model. However, hemispheres are introduced on the CAM surface to represent residual voids that result from electrode manufacturing. The dimension of the surrounding box exceeds the CAM particle by $d_{\mathrm{CAM}}/4$ in every x- and y-direction. In negative z-direction, the particle is connected to the current collector-layer and to ensure sufficient connection, the particle is cut at $d_{\mathrm{CAM}}/10$.
For the void-containing microstructures, voids are generated at the CAM particle surface with a given void diameter until a desired surface coverage is reached. The void position is random and as a part of the particle is cut off for the current collector connection, the achieved surface coverage for the whole particle may differ slightly from the final surface coverage. The void-generation script is implemented in the COMSOL Application Builder.

Cone-Type Microstructures The cone model consists of a unit cell featuring a truncated cone in the center and four cone-fourths at the edges (figure 3), which can be continued periodically in x- and y-direction and is therefore calculated with periodic boundary conditions. The truncated cone is described by the cone diameters at each end, a at the current collector and b at the separator, the cone (or electrode) length l and the overlap dn. The overlap means that some of the simulated geometries have partly overlapping CAM cones at the current collector as displayed in figure S4.
In order for the CAM density to be higher near the current collector, the diameter a has to be larger than b. The unit cell is set up as follows:
The center cone is the basis for a $(1 \times 2 \times 2)$-array of cones, wherein the displacement is

$$\left(0, \frac{2a}{\sqrt{2}}dn, \frac{2a}{\sqrt{2}}dn\right) \tag{1}$$

The whole array is then duplicated and moved by

$$\left(0, \frac{\sqrt{2}a}{2}dn, \frac{\sqrt{2}a}{2}dn\right). \tag{2}$$

Afterwards, the unit cell is cut out as a block with the dimensions

$$\left(l, \sqrt{2}a\ dn, \sqrt{2}a\ dn\right). \tag{3}$$

The loading of the electrode is defined by the diameter ratio of the truncated cone, because the volume ratio of the CAM in the electrode can be calculated as follows:

$$\nu_{\mathrm{CAM}} = \frac{V_{\mathrm{CAM}}}{V} = \frac{2 \cdot V_{\mathrm{cone}}}{V}, \tag{4}$$

with V refering to the total simulated volume and V_{CAM} to the CAM-filled volume in the simulation, which is equal to the volume of two truncated cones in an unit cell. The truncated cone volume is

$$V_{\mathrm{cone}} = \frac{1}{3}\pi \left[\left(\frac{a}{2}\right)^2 + \left(\frac{a}{2}\right)\left(\frac{b}{2}\right) + \left(\frac{b}{2}\right)^2\right] l \tag{5}$$

and the total unit cell volume is

$$V = l \cdot \left(\sqrt{2}a\right)^2 = 2la^2, \tag{6}$$

leading to

$$\nu_{\mathrm{CAM}} = \frac{\pi}{12}\left(1 + \frac{b}{a} + \frac{b^2}{a^2}\right) \tag{7}$$

with $x = b/a$,

$$\nu_{\mathrm{CAM}} = \frac{\pi}{12}\left(1 + x + x^2\right) \tag{8}$$

$$\rightarrow x = \frac{b}{a} = -\frac{1}{2} \pm \sqrt{\frac{1}{4} - 1 + \frac{12\nu_{\mathrm{CAM}}}{\pi}}. \tag{9}$$

For a volume fraction of 55% CAM, this implies

$$\frac{b}{a}\left(\nu_{\mathrm{CAM}} = 0.55\right) = 0.6623, \tag{10}$$

so the simulated cone diameter couples simulated in section 3.4 and analyzed in figure 11 are

$$(a, b) \in \{(2, 1.3), (5, 3.3), (10, 6.6), (20, 13.3)\}\ \mu\mathrm{m}. \tag{11}$$

All simulations and microstructure generations are performed on a HP Z8 G4 Workstation (130767 MB RAM, 2 x Intel Xeon Gold 6134 CPU).

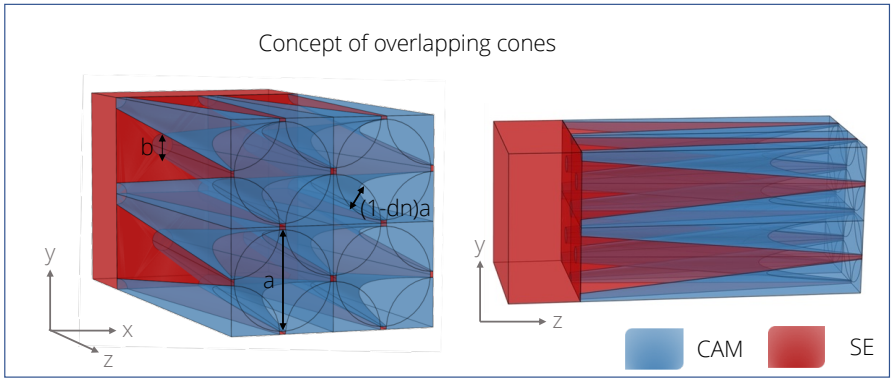

Figure S4. Schematic of the concept of overlapping cones in a structured cathode.

Meshing

We use the COMSOL[4] mesh generator to create tetrahedral meshes that adapt to the underlying geometry. Interfacial regions or narrow pores are meshed finer than bulk volumes. For this purpose, COMSOL uses a Delaunay-based mesh generator.[7] The geometry shape order is linear.
Examples of the meshes and meshing parameters are given in figure S5.
To enable the use of periodic boundary conditions for the particle-type microstructure, the boundary meshes must be identical which requires some manual meshing steps:

- Edge 1 and 2 mesh: Generate a mesh along two neighboring edges in the z-direction
- Edge 3 and 4 mesh: Copy the edge meshes from Edges 1 and 2 to 3 and 4, respectively. Edge 3 opposes Edge 1; Edge 4 opposes Edge 2.
- Face 1 and 2 free triangular mesh: Generate a mesh along two neighboring faces in the xz- and the yz-plane.
- Face 3 and 3 free triangular mesh: Copy the triangular meshes from Faces 1 and 2 to 3 and 4, respectively. Face 3 opposes Face 1; Face 4 opposes Face 2.
- Volume tetrahedral mesh: Mesh the volume with a tetrahedral mesh using the mesh generator.

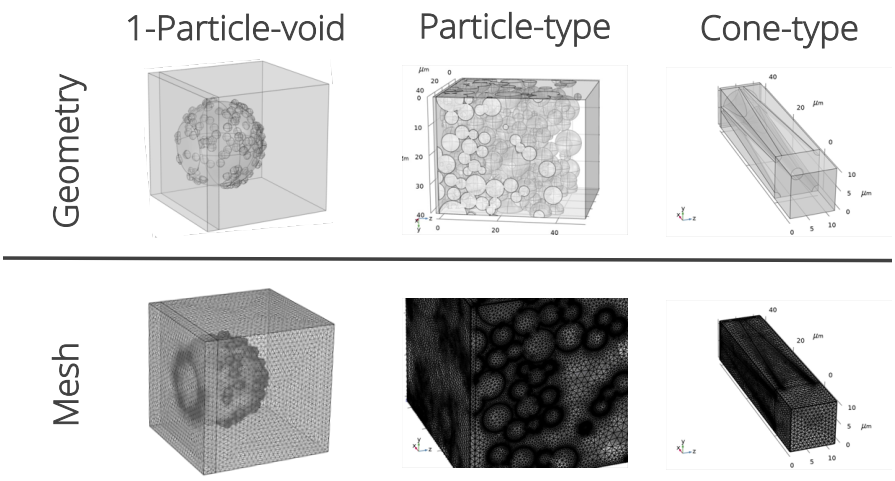

Description			
Maximum element size (µm)	0.378	1.79	1.02
Minimum element size (µm)	0.0162	0.0765	0.0102
Number of tetrahedra	1744880 (for 0.7 µm voids) 515482 (for 2.0 µm voids) 409177 (for 7.0 µm voids)	8625685	523859

Figure S5. Tetrahedral meshes for selected geometries and their characteristics.

Results

Input Parameters

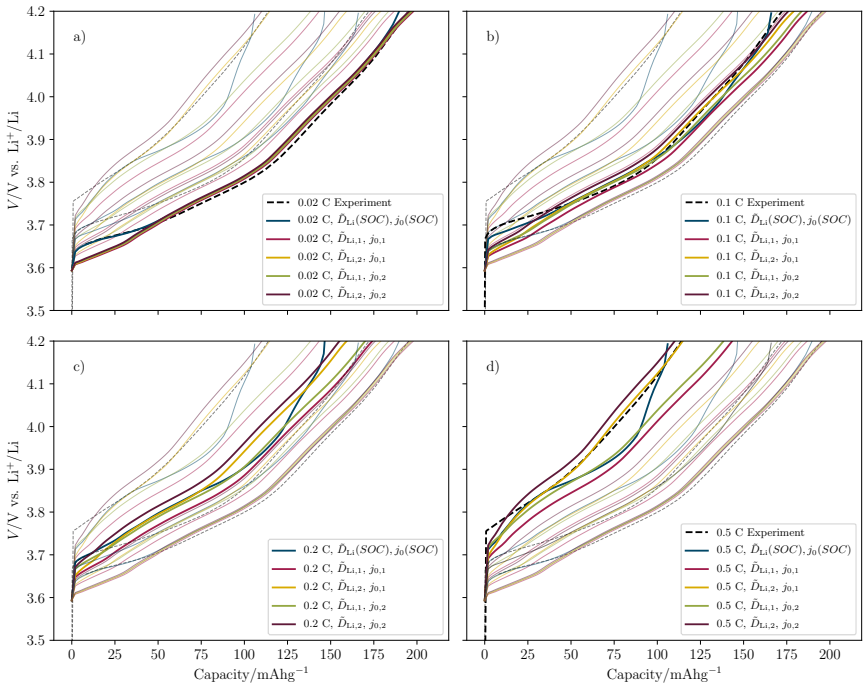

Figure S6. Simulated charge voltage profiles of the particle-type microstructure model with different input parameter sets compared to experimental data, each plot dedicated to a C-rate.

SI: Electrochemical Performance of Composite Cathodes for ASSBs S-12

Voidstudy

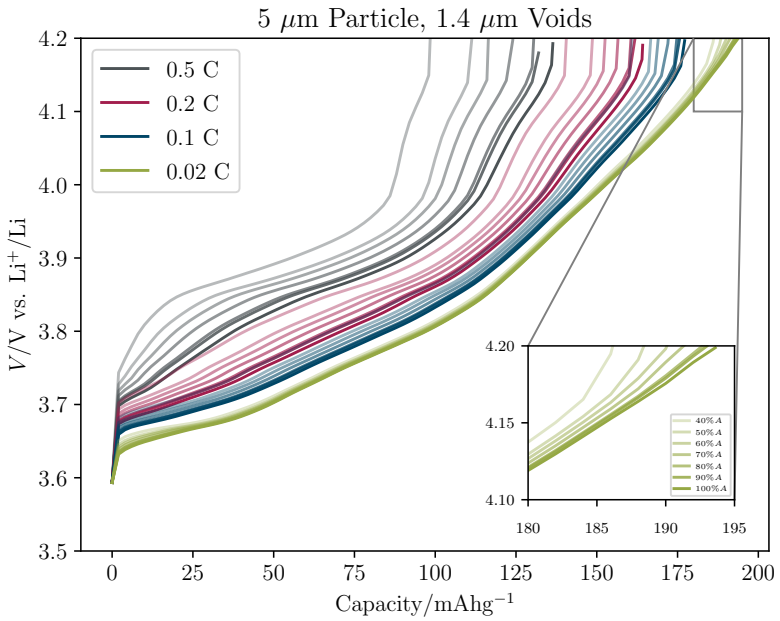

Figure S7. Charge voltage profile for different C-rates in the 1-particle model with voids at the particle surface. 5 μm particle and 1.4 μm voids at varying void surface coverage.

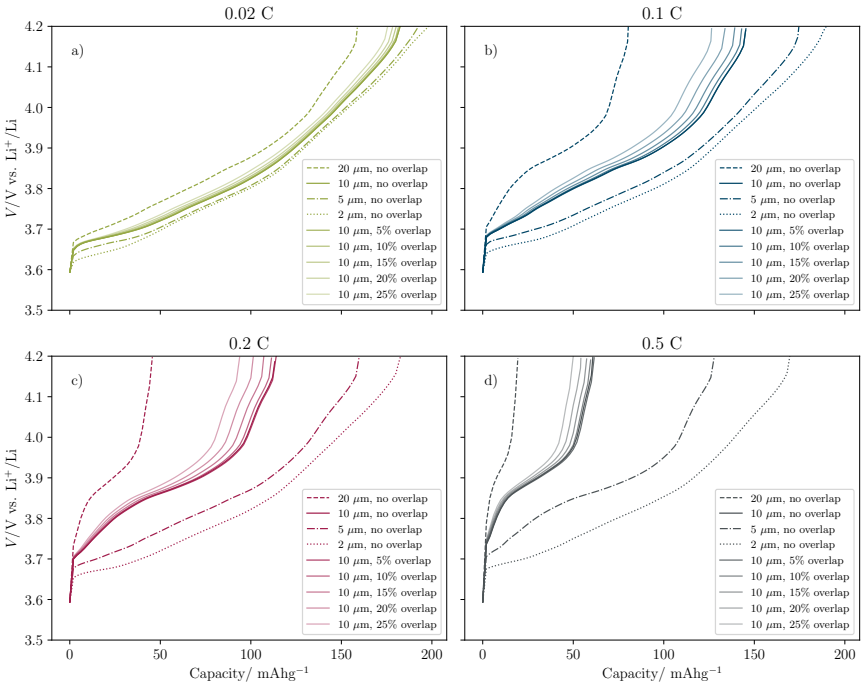

Figure S8. Charge voltage profile of a) 0.02 C, b) 0.1 C, c) 0.2 C and d) 0.5 C charge for different cone microstructures at 55 vol% CAM differing in current collector facing cone diameter $a \in \{2, 5, 10, 20\}$ μm and overlap.

Bibliography

[1] Ruess R, Schweidler S, Hemmelmann H, Conforto G, Bielefeld A, Weber D A, Sann J, Elm M T and Janek J 2020 *J. Electrochem. Soc.* **167** 100532
[2] Xu Z, Jiang Z, Kuai C, Xu R, Qin C, Zhang Y, Rahman M M, Wei C, Nordlund D, Sun C-J, Xiao X, Du X-W, Zhao K, Yan P, Liu Y and Lin F 2020 *Nat. Commun.* **11** 83
[3] Bielefeld A, Weber D A and Janek J 2019 *J. Phys. Chem. C* **123** 1626–1634
[4] Comsol AB 2019 Comsol Multiphysics 5.4
[5] Conforto G, Ruess R, Schröder D, Trevisanello E, Fantin R, Richter F H and Janek J 2021 *J. Electrochem. Soc.* **168** 070546
[6] Bielefeld A, Weber D A and Janek J 2020 *ACS Appl. Mater. Interfaces* **12** 12821–12833
[7] Bretz B 2016 Improved capabilities for meshing with tetrahedral elements `https://www.comsol.com/blogs/improved-capabilities-for-meshing-with-tetrahedral-elements/` Comsol Blog

C. List of Peer-Reviewed Publications and Articles to be Submitted

- **Bielefeld, A.**; Weber, D. A.; Janek, J. Microstructural Modeling of Composite Cathodes for All-Solid-State Batteries. *J. Phys. Chem. C* **2019**, 123, 1626-1634.

- **Bielefeld, A.**; Weber, D. A.; Janek, J. Modeling Effective Ionic Conductivity and Binder Influence in Composite Cathodes for All-Solid-State Batteries. *ACS Appl. Int. Mater.* **2020**, 12, 12821-12833.

- Ruess, R.; Schweidler, S.; Hemmelmann, H.; Conforto, G.; **Bielefeld, A.**; Weber, D. A.; Sann, J.; Elm, M. T.; Janek, J. Lithium Transport Kinetics in $LiNi_{0.8}Co_{0.1}Mn_{0.1}O_2$ Cathode Active Materials and the Contrasting Consequences for the Performance of Lithium-Ion Batteries with Liquid or Solid Electrolytes. *J. Electrochem. Soc.* **2020**, 167, 100532.

- **Bielefeld, A.**; Weber, D. A.; Rueß, R.; Glavas, V.; Janek, J. Influence of Lithium Ion Kinetics, Particle Morphology and Voids on the Electrochemical Performance of Composite Cathodes for All-Solid-State Batteries *J. Electrochem. Soc.* **2022**, 169, 020539.

- Minnmann, P.; Strauss, F.; Trevisanello, E.; Dreyer, S. L.; Ruess, R.; **Bielefeld, A.**; Burkhardt, S.; Adelhelm, P.; Brezesinski, T.;Richter, F. H.; Janek, J. Designing Cathode Active Materials for Solid-State Batteries. *to be defined* **2022**, in preparation.

D. List of Oral and Poster Presentations

- **Bielefeld, A.**; Weber, D. A.; Janek, J. Microstructural Modeling of Composite Cathodes for All-Solid-State Batteries. Poster at the *3rd Bunsen Colloquium on Solid-State Batteries*, Frankfurt/Main, 14.-16.11.**2018**

- **Bielefeld, A.**; Weber, D. A.; Janek, J. Microstructural Modeling of Composite Cathodes for All-Solid-State Batteries. Oral Presentation at *MRS Spring Meeting*, Phoenix, 22.-26.04.**2019**

- **Bielefeld, A.**; Weber, D. A.; Janek, J. Modeling of Composite Cathodes as a Design Tool for All-Solid-State Batteries. Oral Presentation at *3rd Dresden Battery Days*, Dresden, 23.-25.09.**2019**

- **Bielefeld, A.**; Weber, D. A.; Janek, J. Microstructural Electrode Design Based on Modeling of Composite Cathodes for All-Solid-State Batteries. Oral Presentation at *237th ECS Meeting*, Montreal, 10.-15.05.**2020** (canceled due to COVID19)

E. List of Patents

- **Bielefeld, A.**; Weber, D. A. , Manufacturing Method for an Electrode Precursor and Electrode Precursor and Manufacturing Method for an Electrode Paste. *Patent pending* **2019**, DE102019203057A1, CN111180658A.

Acknowledgments

Die vergangenen Jahre waren für mich durchaus eine Herausforderung, verbunden mit vielen kleineren und größeren Erfolgen, mit unglaublich vielen Einblicken, Erkenntnissen, Möglichkeiten zu wachsen und insbesondere mit einzigartigen, wundervollen Menschen, die mich unterstützt und gefördert haben und denen ich hier danken möchte.

Ein besonderer Dank geht an Prof. Dr. Jürgen Janek, der mir jederzeit unterstützend und mit einem positiven Blick auf die Dinge zur Seite stand, offen für neue und alte Ideen war und ausdauernd an einer Brücke zwischen experimentellen und modellbasierten Arbeiten baut. Danke für die ideale Waage aus Freiraum und Antreiben, die ich sehr schätze und danke für den Zuspruch, das Vertrauen und die persönliche, wissenschaftliche und berufliche Förderung.
Ich freue mich, dass Prof. Dr. Doreen Mollenhauer das Koreferat dieser Arbeit übernommen hat und danke ihr, sowie Prof. Dr. Ellen Ivers-Tiffée und Prof. Dr. Peter Klar als Mitgliedern der Prüfungskommission.

Ich danke der Volkswagen Aktiengesellschaft für die finanzielle Förderung, die Möglichkeiten des interdisziplinären Austauschs und die Einblicke in die Automobilbranche, die ich in meiner Zeit bei Volkswagen gewonnen habe.
Meinem dortigen Betreuer möchte ich für so vieles danken, von der fachlichen Betreuung über die chemischen und persönlichen Ratschläge, die langen (privaten) Gespräche, das tägliche Schreibtischnachbartum bis zu den Kommata, die er unermüdlich in meine ersten Arbeiten gezeichnet hat. So wurde die Kommasetzung im Englischen nicht zu meinem Endgegner! Er trägt einen großen Anteil daran, wie sich meine Arbeit entwickelt hat und entwickeln konnte und darüber hinaus ist auch im Bezug auf Notfallteevorräte immer Verlass auf ihn.
Auch meiner direkten Vorgesetzten möchte ich danken, dafür, dass sie so beharrlich für mich gekämpft hat, für ihr Verständnis, ihr Feedback, ihre Hilfe und dafür, dass sie mich fachlich, wie auch persönlich sehr gefördert und dabei eine offene und transparente Teamgestaltung vorgelebt hat.
Was bin ich froh über den Austausch mit den Simulationskollegen, darüber, dass sie für mich und mit mir Softwarelizenzen jonglierten und dabei Flach- und Physikerwitze rissen. Danke, Los Comsolieros!
Ich danke dem Volkswagen Team für die Zusammenarbeit, den Zusammenhalt und die täglichen "Social Meetings", als uns Covid19 ins Homeoffice schickte.

Ohne seine beharrliche Art, den Dingen auf den Grund zu gehen und zuverlässige Daten zu messen, wäre der abschließende Teil dieser Arbeit nicht halb so interessant und relevant geworden. Mein Dank geht an Dr. Raffael Ruess für die Unterstützung von experimenteller Seite.
Dank Philip Minnmann und seiner Geduld für Modellierer im Labor, konnte ich eigene Feststoffbatterien bauen und einiges aus einem anderen Blickwinkel sehen. Danke für das Näherbringen der experimentellen Sichtweise und das Anschubsen zum Hindernislauf durch den Matsch.
Justine Ruhl, Biance Helm, Simon Randau, und Philip Minnmann, ich werde nicht vergessen, wie viel Spaß ich mit euch im Matsch hatte und wie schlimm der Muskelkater in den folgenden Tagen war.
Ich danke der Arbeitsgruppe von Prof. Dr. Janek für die freundliche Aufnahme und die Einladungen zum Boulderngehen – Ich bin sehr gern unter euch.
Auch den Konsortien der öffentlich geförderten Projekte FELIZIA, NASEBER und ProFeLi möchte ich für die spannenden Einblicke und Diskussionen danken.

Und schließlich danke ich meinen Eltern für die immerwährende Unterstützung, die Motivation und ihren ungebrochenen Glauben an mich.
Ich danke Julius, dass er in der ersten Hälfte der Promotion an meiner Seite war.
Nicht zuletzt möchte ich Martin dafür danken, dass er meine Definition von Geborgenheit ist, in hellen und dunklen Momenten bei mir ist und das Leben mit mir teilt.